UQAR
Université du Québec
à Rimouski

GÉNÉRATION D'ONDES INTERNES PAR COLLISIONS FRONTALES

MÉMOIRE PRÉSENTÉ

dans le cadre du programme de maîtrise en océanographie

en vue de l'obtention du grade de Maître sciences (M.Sc.)

PAR

©BRUNO ST-DENIS

Mai **202**1

Composition du jury :

Louis-Philippe Nadeau, président du jury, Institut des sciences de la mer de Rimouski

Daniel Bourgault, directeur de recherche, Institut des sciences de la mer de Rimouski

Cédric Chavanne, codirecteur de recherche, Institut des sciences de la mer de Rimouski

Jose Da Silva, examinateur externe, Université de Porto

Dépôt initial le 3 décembre 2020 Dépôt final le 14 mai 2021

What's an ocean but a multitude of drops - Adam Ewing, Cloud Atlas, écrit par David Mitchell

REMERCIEMENTS

La recherche scientifique, tout comme l'écriture d'un mémoire, n'est pas une épreuve que nous entreprenons seul. En effet, plusieurs individus y contribueront en apportant une idée, une vision ou simplement un p'tit verre de Scotch ; en somme, une goutte d'espoir dans un océan de remise en question. Le premier "collaborateur" de ce mémoire fut Jean-Luc Shaw, un collègue exceptionnel avec qui j'ai effectué ma première "vraie" mission océanographique et qui m'as appris qu'il existe toujours une solution à un problème. Par la suite, Abigaelle Dussol fut d'une précieuse aide en analysant et critiquant constructivement mes présentations orales et travaux. Un merci spécial doit être remis à Jérome J. Guay pour son oreille attentive, ses nombreux conseils et le partage de plusieurs liqueurs écossaises. Merci beaucoup à Sophie Bédard de m'avoir constamment épaulé pendant la deuxième année de maîtrise et de m'avoir dépanné lors de la mission hivernale de 2019. Je dois aussi saluer l'aide importante apportée par Jérôme Lemelin dans la récolte de données lors de la mission Sillex 2018 ainsi qu'à James Caveen, le phare de tous physiciens du POLR, sans qui nous serions perdu sur Mingan.

Je tiens aussi à remercier Louis Gostiaux, qui en plus de m'avoir fait découvrir la ville de Lyon, m'a accueilli au LMFA (Laboratoire de mécanique des fluides et d'acoustique) afin deprésenter mes résultats de recherche et ainsi profiter des connaissances et expertises de son groupe de recherche.

Sur une note plus personnel, je dois remercier ma famille : Mathieu, Céline, Richard et Manon pour leurs inconditionnels encouragements.

Peter et Cédric, vous avez joué un rôle important dans mon apprentissage afin de former le scientifique que je suis. Peter, merci de m'avoir amené en mer, à de nombreuse reprises, dans ton programme de monitorage et fait découvrir le Saguenay à partir du fjord. Cédric, merci d'avoir co-dirigé cette recherche, malgré nos échanges moins fréquents qu'avec Daniel,

tu as apporté une vision différente au projet et pris le temps de corriger et améliorer tous mes travaux et présentations.

Je ne pourrai conclure cette section sans remercier la pièce maitresse de ce projet, Daniel Bourgault :

Cher Daniel, merci énormément pour ton éternel patience et positivisme. Ta présence dans toutes les facettes de cette recherche ainsi que ton inconditionnel support ont joué un rôle important dans l'aboutissement de ce projet. Tu as su m'écouter, me comprendre et philosopher avec moi sur mes 1001 remises en questions vis-à-vis la pertinence et la portée scientifique de cet oeuvre. Tu as toujours cru en moi et m'as offert la possibilité de faire rayonner le fruits de mes travaux dans de nombreux congrès régionaux et internationaux, ainsi que d'organiser la mission exploratoire à l'hiver 2019. Merci pour tout, en espérant te revoir sur la glace, le terrain de badminton et autour d'une bière.

RÉSUMÉ

L'intrusion résultant d'une collision frontale entre deux masses d'eau fortement stratifiées a récemment été décrite comme une potentielle source de génération d'ondes internes solitaires. Cependant, peu d'observations de terrain ont été rapportées. De ce fait, les relations entre les propriétés des ondes générées (longueur d'onde, amplitude, énergie) et les conditions de forçage (épaisseur des couches de surface, cisaillement et nombres de Richardson et de Froude) sont à ce jour, mal comprises. Pour pallier cet inconvénient, plusieurs simulations numériques idéalisées ont été effectuées à l'aide d'un modèle 2-D non-linéaire et non-hydrostatique. L'objectif de ces modélisations est de déterminer des relations empiriques entre les propriétés des ondes internes générées et les conditions initiales en explorant l'espace des paramètres régissant ce mécanisme. Dans cet article, nous présentons les résultats des simulations et des observations de terrain collectées lors des étés 2017 et 2018 dans le fjord du Saguenay.

Mots clés : [Onde interne, Intrusion, Front, Collision, Saguenay, Fluide stratifié, Modélisation numérique]

ABSTRACT

The intrusion resulting from a frontal collision of two stratified water masses has recently been described as a potential source of generation of internal solitary wavetrains (ISW). However, only a handful of field observations have been reported such that the relationships between the properties of the generated ISW (wavelength, amplitude, energy), and the background and forcing conditions (surface layer thickness, shearing, Richardson and Froude numbers) are misunderstood. To assess this issue, idealized numerical simulations are carried out using a 2D nonlinear and nonhydrostatic model. The objective is to determine empirical relationships between ISW properties and the control condition by exploring the wide parameter space involved in this mechanism. Here we report the results of these numerical simulations and from few observations collected during the 2017 and 2018 summer expeditions in the Saguenay Fjord (Quebec, Canada).

Keywords : [Internal wave, Intrusion, Front, Simulation, Collision, Saguenay Fjord, Stratified fluid, Numerical model]

TABLE DES MATIÈRES

LISTE DES TABLEAUX

LISTE DES FIGURES

LISTE DES ABRÉVIATIONS

ADCP Acoustic Doppler Current Profiler

APE Available Potential Energy

CTD Conductivity - Temperature - Depth sensors

DFO Department of Fisheries and Oceans

IW Internal Wave

ISW Internal Solitary Wave.

K-H Kelvin-Helmholtz Instabilities

LISTE DES SYMBOLES

ρ Masse volumique [kg m^{-3}].

N Fréquence de flottabilité [s^{-1}]

S Cisaillement vertical [s^{-1}]

R_i Nombre de Richardson [Adimensionel]

F Nombre de Froude [Adimensionel]

u_i Vitesse de l'écoulement [m s^{-1}]

c Vitesse de phase [m s^{-1}]

Δx Résolution spatiale horizontale [m]

Δz Résolution spatiale verticale [m]

Δt Pas de temps

w Vitesse vertical de l'écoulement [m s^{-1}]

L Largeur horizontale du front [m]

d_i Demi épaisseur de la pycnocline [m]

h_i Épaisseur de la couche de surface [m]

$g*$ Gravité réduite [m s^{-2}]

E_k Énergie cinétique [J m^{-1}]

U Vitesse horizontal initiale

A Amplitude de l'onde [m]

c_p Vitesse de phase de l'onde [m s^{-1}]

λ Longueur d'onde [m]

μ Position de la pycnocline ou amplitude de marée [m]

v_f Vitesse du front [m s^{-1}]

INTRODUCTION GÉNÉRALE

De la fin du néolithique jusqu'à l'ère moderne, en passant par la Renaissance, la navigation et l'océan ont toujours été une source de commerce, de conquête, d'inspiration et de découvertes. Les premières petites embarcations servaient essentiellement à traverser les fleuves, rejoindre d'autres îles d'un même archipel et à pêcher.

Dans l'Antiquité, l'exploration des mers prend de l'ampleur avec l'apparition de navires plus imposants comme la pentécontère, le trirème (Papalas, 1997) et le quinquérème, permettant le transport des troupes, la guerre navale de grande envergure ainsi que la traversée de la Méditérannée. Les thèmes de l'océan et de la navigation sont bien présents au sein des civilisations antiques, notamment avec les prières à Posédion, Neptune ou Njord lorsque l'on souhaitait une mer calme et des vents favorables. On dénote une multitude de créatures maritimes dans les contes mythologiques telles que les sirènes de L'Odyssée d'Homère et l'hydre de Lerne, 2^{e} des 12 travaux d'Hercule. Deux des septs merveilles de l'Antiquité étaient reliées à la mer, le colosse de Rhodes en Grèce et la tour d'Alexandrie sur l'île de Pharos, d'où la provenance du mot «phare», encore couramment utilisé au 21^{e} siècle.

À la fin du Moyen-Âge sont apparus les navires capables d'affronter la haute-mer, telle que la caravelle et la nef (Schwarz, 2008). Ils sont largement utilisés pour trouver des routes commerciales navigables vers l'Orient. L'arrivée de ces grandes embarcations et la découverte de l'Amérique en 1492 marquent le début des grandes explorations maritimes. S'en suit la découverte de plusieurs archipels dans l'Atlantique et dans le Pacifique, la rencontre avec les premières nations, la découverte de nouvelles espèces marines et la première circumnavigation par Fernando de Magellan.

L'industrialisation des grandes puissances mondiales comme la Grande-Bretagne et la France a permis de donner un volet plus scientifique aux grandes explorations. En 1872, Charles Wyville Thompson, zoologiste et naturaliste anglais, convainquait la couronne bri-

tannique de lui prêter la direction du H.M.S. Challenger pour y effectuer une expédition scientifique. Équipé de plusieurs laboratoires et équipements d'analyse, le navire pris la mer en décembre 1872 pour y revenir 4 ans plus tard. Ayant parcourue plus de 125 000 km, recensée près de 4000 nouvelles espèces marines et effectuée des centaines de relevés de température et de bathymétrie, l'expédition du Challenger met en place les bases de l'océanographie.

Au tournant du 20^{e} siècle, désirant étudier les pôles, la Norvège concevait une goelette à coque arrondie capable de se laisser dériver sur la banquise, le Fram (Nansen, 1900). À partir de 1893, plusieurs expéditions dirigées successivement par Nansen, Sverdrup et Amundsen amenèrent ce navire aussi bien dans l'Arctique que dans l'Antarctique, y ramenant de précieuses découvertes scientifiques et géographiques tel que la preuve que les glaces de l'Arctique ne sont pas assises sur un continent rocheux, mais une mer profonde.

De nos jours, que ce soit pour extraire ses ressources, transporter des biens, attaquer des nations ou alimenter notre imaginaire, la mer exerce toujours un attrait important sur notre mode de vie et notre culture. Que ce soit dans l'univers de Jules Verne, au travers d'un documentaire de la BBC ou dans un film de Spielberg, l'océan fascine encore l'homme par la beauté de ses eaux, l'incommensurable diversité de ses espèces, ses inexplorées profondeurs et la complexité de sa physique.

Dans un contexte où la fonte des glaciers, l'acidification des océans, la pollution par le plastique et l'augmentation de la température exercent une pression grandissante sur le milieu marin, il devient crucial de comprendre les divers processus physico-chimiques impliqués dans la circulation générale, l'interaction océan-glace-atmosphère et la dynamique côtière. Plus spécifiquement, de nombreux phénomènes océaniques observés depuis plusieurs décennies tels que les tourbillons, les fronts et les ondes internes sont à ce jour, mal compris. Ces dernières, ainsi que leurs propriétés et méthodes de formation seront le coeur de ce mémoire.

Ondes internes

Comparable aux vagues de surface, les ondes internes sont des vagues se propageant à l'intérieur d'un fluide, majoritairement le long de la pycnocline dans un environnement fortement stratifié (Jackson et al., 2012). N'étant pas exclusivement réservé à l'océan, on observe aussi ce phénomène dans l'atmosphère par exemple, lorsque des vents catabatiques interagissent, la nuit, avec une inversion de température (Christie et al., 1978). Les Morning Glories, bandes de nuages en forme de rouleau (Fig.1), observés dans le golfe de Carpentarie en Australie, sont une des plus visibles manifestations d'ondes internes dans l'atmosphère (Christie et al., 1981; Reeder et al., 1995).

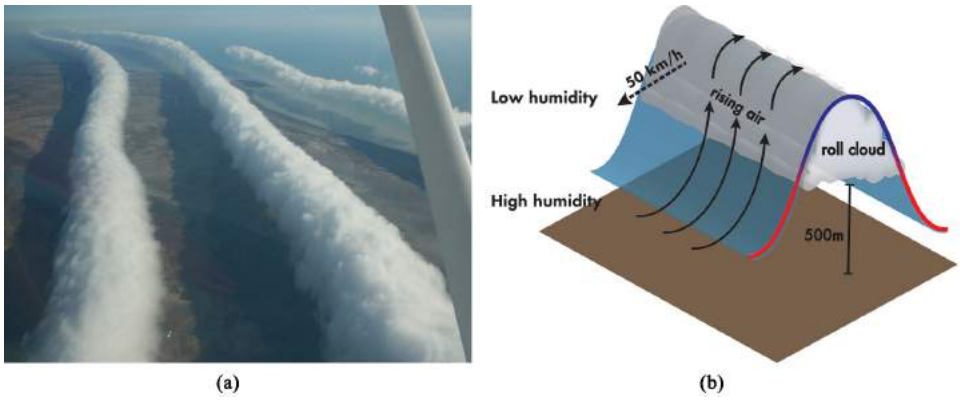

Figure 1: a) Photo aérienne des Morning Glories près de Burketwon (Australie), prise par Mike Petroff. b) Illustration de la formation de Morning Glories tirée de (Ouazzani et al., 2014)

Dans un contexte océanique, des vagues sous-marines ayant différentes caractéristiques physiques sont observées dans plusieurs régions du monde tel les fjords (Stigebrandt, 1976), l'embouchure de certains fleuves (Nash and Moum, 2005) et les estuaires (Wang and Pawlowicz, 2017; Wang et al., 2019; Marmorino and Smith, 2007). En haute mer, notamment sur le plateau des Mascareignes au large des îles de la Réunion (Da Silva et al., 2011) et en mer de Chine méridionale (Lien et al., 2014; Alford et al., 2015), une multitude d'ondes internes d'une amplitude, c'est-à-dire la hauteur séparant le creux de la crête, de plus de 50 m ont été

observées. Plusieurs études ont aussi démontrées la présence d'ondes internes dans des lacs, notamment dans l'état de New York (Hunkins and Fliegel, 1973; Dorostkar et al., 2017), en Colombie-Britannique (Farmer, 1978) et en Écosse (Thorpe et al., 1972).

Indépendamment de leur lieu de formation, la propagation et le déferlement de ces vagues sous-marines jouent un rôle important pour une multitude de processus océaniques. Le mélange et le transport causés par les forts courants verticaux associés au passage et déferlement d'ondes internes peuvent générer un flux vertical de nutriment (Wang et al., 2007). Dans la même optique, les sédiments peuvent être érodés, remis en suspension et transportés vers la rive lors de leur déferlement (Bourgault et al., 2014). Les vagues sous-marines qui sont caractérisées par un noyau emprisonné («trapped cores» en anglais), c'est-à-dire un volume d'eau de densité intermédiare emprisonné dans une recirculation entre deux crêtes d'une vague, sont un moyen efficace de transporter une masse d'eau (Lamb, 2003; Richards et al., 2013). Les ondes internes ont la propriété de se propager sur des centaines de kilomètres si elles ne rencontrent pas d'obstacles topographiques ou ne déferlent pas.

Mecanisme de génération

On retrouve dans la littérature scientifique différents mécanismes expliquant la formation de vagues sous-marines dans l'océan. Le plus connu, est la génération orographique («Lee Waves»). Mis de l'avant par Maxworthy (1979), d'après l'expérience de Lee and Beardsley (1974), ce mécanisme est décrit par l'interaction de la marée avec un obstacle topographique. La génération d'ondes se produit en fonction de l'état critique de l'écoulement qui est décrit par le nombre de Froude. Il s'agit d'un nombre adimensionel F, exprimé par $F = u_f/c$ où u_f est la vitesse de l'écoulement du fluide et c la vitesse de phase du premier mode de l'onde interne. Ce mécanisme génère des ondes internes dans un milieu stratifié lorsque l'écoulement passe de supercritique ($F > 1$) à sous critique ($F < 1$) causé par une variation des courants de marée autour d'un obstacle topographique tel un seuil (Jackson et al.,

2012). Lors de la marée descendante, les courants de marée dirigés vers l'aval empêchent l'eau en aval de l'obstacle de le franchir, car l'écoulement est supercritique, il y a donc une accumulation d'énergie (fig 2a). Lorsque les courants de marée s'inversent, l'écoulement devient sous critique et l'eau emprisonnée en aval franchit le seuil et l'énergie est libérée sous forme de perturbation de la pycnocline se transformant en ondes internes solitaires se propageant vers l'amont (fig 2b et c).

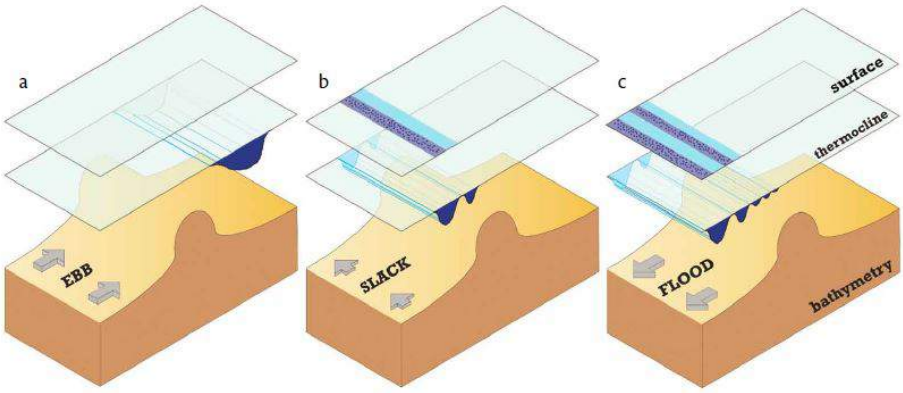

Figure 2: a) Schéma de la formation d'ondes internes par génération orographique, tirée de Jackson et al. (2012).

Dans certains lacs ayant une grande superficie, on observe des ondes internes générées lorsque l'intensité du vent diminue après avoir soufflé pendant plusieurs jours dans la direction de l'axe longitudinal du lac. Le stress d'un vent fort et continu génère un transport d'eau vers l'une des extrémités du lac entrainant la remontée de la thermocline à l'autre extrémité. Dès que le vent diminue, la thermocline va tendre rapidement à retrouver sa position initiale, ce qui génère des oscillations sous forme d'ondes internes (Thorpe et al., 1972; Boegman et al., 2005). Ce phénomène est aussi nommé seiche hydraulique.

Un navire de croisière ou de transport de marchandise navigant dans un milieu stratifié peut aussi générer des ondes internes lorsque le tirant d'eau est plus grand que la profondeur

de la pycnocline (Grue et al., 2016). Si la vitesse du navire est inférieure à celle des ondes générées, il est possible que celles-ci rattrapent le navire entrainant ainsi une subite perte de vitesse, c'est ce qu'on appelle le phénomène des eaux mortes (Ekman, 1904; Miloh et al., 1993).

Il existe une panoplie d'autres mécanimes expliquant la formation de vagues sous-marines, certains parmi ceux-ci ont été découverts dans les 15 dernières années, par exemple la génération d'ondes internes par collision frontale. Postulé par Maxworthy (1980), cette méthode de formation se produit lorsque deux masses d'eau stratifiées ayant des densités différentes collisionnent (Fig 3a). La différence de densité entre les eaux forcent la plus dense à plonger sous la plus légère, générant une intrusion, une cisaille à l'interface des couches et des oscillations de la pycnocline (Fig 3b). Au fur et à mesure que l'intrusion progresse, ces oscillations s'éloignent du front sous forme d'ondes internes et des instabilités de Kelvin-Helmholtz se forment si l'interface ρ_1, ρ_2 devient suffisamment instable (Fig 3c).

Depuis Maxworthy (1980), plusieurs autres études se sont intéressées à ce mécanisme en laboratoire à l'aide d'expérience faites en bassin contrôlé par un sas (Hoyler and Huppert, 1980; Cheong et al., 2006) et/ou à l'aide de modèles numériques (Flynn et al., 2008) en étudiant l'impact d'une intrusion dans un fluide en 2 ou 3 couches. Toutefois quelques observations de ce phénomène ont été rapportées, notamment par Nash and Moum (2005) où une langue d'eau de moindre densité semblait émettre des ondes internes en entrant en collision avec une masse d'eau plus dense provenant de l'océan Pacifique. Cependant, le mécanisme impliqué dans ce processus de formation n'était pas totalement compris à ce moment.

Problématique et objectifs

En 2016, Bourgault et al. (2016) démontrent, à l'aide d'observations de terrain recueillies dans le fjord du Saguenay (Canada), l'existence de la formation d'ondes internes par collision frontale. En utilisant quelques simulations numériques idéalisées à partir de

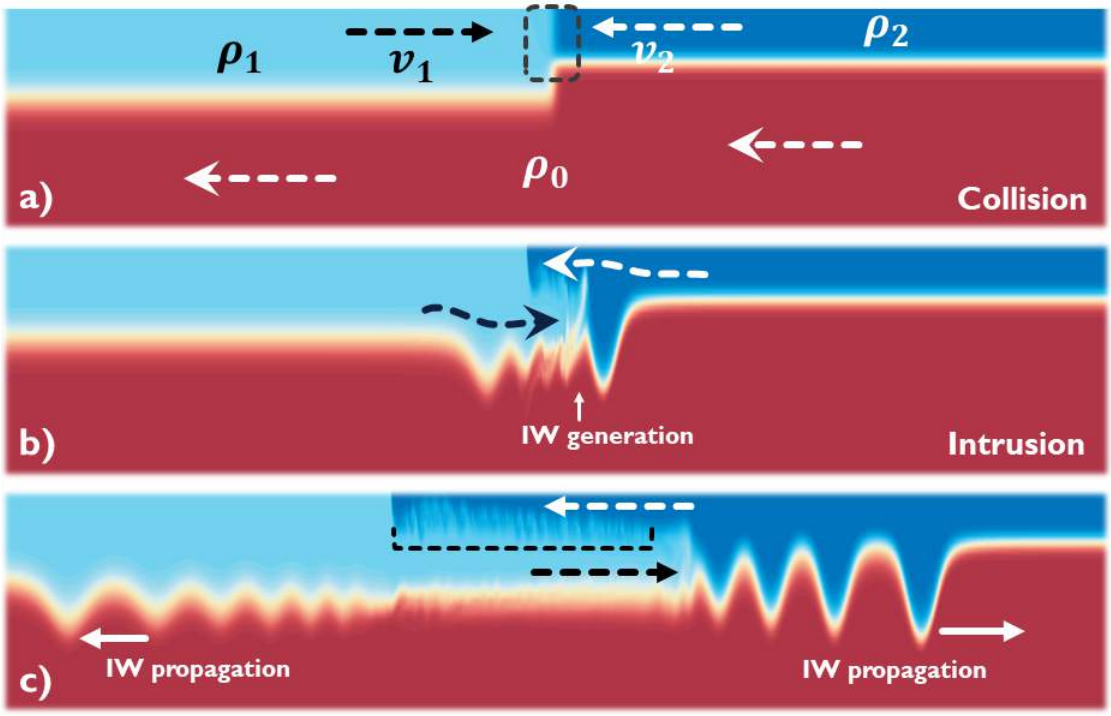

Figure 3: Schéma montrant le processus de formation d'ondes internes par collision frontale où $\rho_0 > \rho_1 > \rho_2$ et v_1 et v_2 convergent, a) Les deux masses d'eau de surface collisionnent, b) La masse d'eau la plus dense s'introduit sous la plus légère générant des oscillations à la pycnocline, c) ces pertubations se propagent sous forme d'ondes internes solitaires

leurs données, ils expliquent et lient les différents phénomènes physiques impliqués dans ce mécanisme ; front, intrusion, instabilités et ondes internes. Cependant, seulement deux cas de ce type de génération ont été échantillonnés et certains questionnements persistent toujours concernant le vaste espace des paramètres régissant ce processus, la provenance des différentes masses d'eau de surface et l'impact des conditions environnementales sur les propriétés des ondes générées.

Afin de répondre à ces interrogations, une série de missions de terrain dans le cadre du projet nommé Sillex (acronyme anglais de Sill Experiment) a eu lieu à l'été 2017 et 2018 dans le fjord du Saguenay, près de l'endroit où l'équipe avait échantillonné lors de leur première découverte. Afin de compléter les observations recueillies lors de ces campagnes océanographiques, plusieurs simulations numériques idéalisées ont été effectuées afin

d'étudier l'espace des paramètres impliqués dans ce mécanisme ; densité des masses d'eau, vitesse du courant, épaisseur des couches de surface et de la pycnocline, etc.

Fjord du Saguenay

Le fjord du Saguenay est situé dans la province de Québec, dans l'est du Canada. Orienté principalement dans l'axe est-ouest, il s'étend sur une longueur de 120 km et une largeur moyenne de 2 km, avec certaines zones d'étranglement. Comme la plupart des fjords, sa densité est contrôlée principalement par la salinité, oscillant entre 26 et 31 PSU dépendemment des saisons et de la profondeur (Belzile et al., 2016). Son principal affluent d'eau douce est la rivière Saguenay se déversant dans la partie nord en amont de Sainte-Rose-du-Nord. Contrairement à plusieurs fjords, il débouche sur l'estuaire du Saint-Laurent en bordure de la ville de Tadoussac et non sur l'océan. Trois seuils topographiques possédant une profondeur de 18, 60 et 120 mètres, situés respectivement à 2 km en aval de Tadoussac et 18 et 32 km en amont (Fig. 4), divisent le fjord en 3 bassins. Ces montagnes sous-marines, principalement celle près de Tadoussac, influencent le renouvellement des eaux en obstruant la circulation des masses d'eaux profondes avec l'estuaire du Saint-Laurent (Belzile et al., 2016; Galbraith et al., 2018). La forme en entonnoir de l'estuaire est propice à la génération de marée ayant en moyenne 4 mètres de marnage près de Tadoussac, parfois 6 mètres en vives-eaux (Siebert et al., 1979). De ce fait, les eaux denses ayant une profondeur plus grande que le sommet du seuil peuvent être transportées par la marée dans les bassins du fjord. De plus, l'interaction de la marée et des seuils génère des ondes internes maintes fois observées lors des différentes missions dans le Saguenay (Janes, 2008).

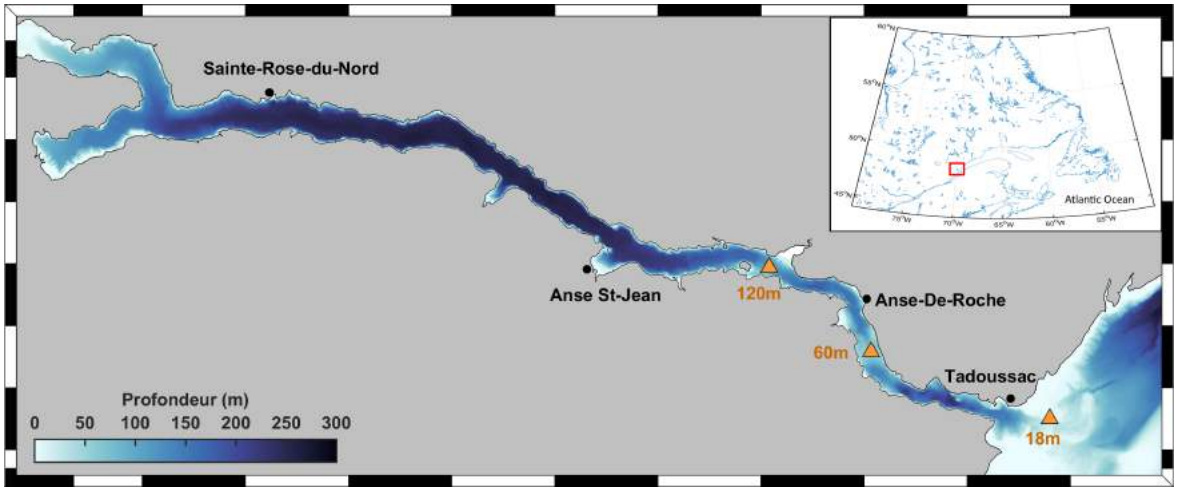

Figure 4: Carte bathymétrique du fjord du Saguenay montrant les seuils et leurs profondeurs (triangle jaune).

ARTICLE 1

GÉNÉRATION D'ONDES INTERNES PAR COLLISION FRONTALE

Résumé

L'intrusion résultant d'une collision frontale entre deux masses d'eau fortement stratifiées a récemment été décrite comme une potentielle source de génération d'ondes internes solitaires. Cependant, peu d'observations de terrain ont été rapportées. De ce fait, les relations entre les propriétés des ondes générées (longueur d'onde, amplitude, énergie) et les conditions de forçage (épaisseur des couches de surface, cisaillement et nombres de Richardson et de Froude) sont à ce jour, mal comprises. Pour pallier cet inconvénient, plusieurs simulations numériques idéalisées ont été effectuées à l'aide d'un modèle 2-D non-linéaire et non-hydrostatique. L'objectif de ces modélisations est de déterminer des relations empiriques entre les propriétés des ondes internes générées et les conditions initiales en explorant l'espace des paramètres régissant ce mécanisme. Dans cet article, nous présentons les résultats des simulations et des observations de terrain collectées lors des étés 2017 et 2018 dans le fjord du Saguenay.

Abstract

The intrusion resulting from a frontal collision of two stratified water masses has recently been described as a potential source of generation of internal solitary wavetrains (ISW). However, only a handful of field observations have been reported such that the relationships between the properties of the generated ISW (wavelength, amplitude, energy), and the background and forcing conditions (surface layer thickness, shearing, Richardson and Froude numbers) remain unclear. To assess this issue, idealized numerical simulations are carried out using a 2D nonlinear and nonhydrostatic model. The objective is to determine empirical relationships between ISW properties and the environmental conditions by exploring the wide parameter space involved in this mechanism. Here we report the results of these numerical simulations and few observations collected during the 2017 and 2018 summers in the Saguenay Fjord (Quebec, Canada).

1.1 Introduction

Similar to surface gravity waves, internal waves (IWs) are perturbations supported by a medium through which they propagate as oscillatory motions (Gerkema and Zimmerman, 2008). Instead of propagating at the air-water interface as do surface waves, IWs travel inside the stratified water masses, mostly at the sharpest density step, and in some cases, at all depths in continuously-stratified oceans. Compared to surfaces waves, they have longer wavelength and period, and also a lower travelling speed (Garrett and Munk, 1979). Their vertical motions can alter the sea surface roughness allowing them to become visible from the surface as stripe patterns (Apel, 2002).

A particular class of internal waves are the solitary waves (ISW). They consist of isolated large amplitude waves of quasi-permanent form propagating under nonlinear hydrodynamics (Apel, 2002). Despite being termed *solitary*, they are often observed in packets of waves, however single depressions have also been reported. They can travel for many hours and over hundreds of kilometers if they don't encounter topographic barriers or breaking conditions. As they break, they modify the water mass properties by generating vertical mixing, nutrients redistribution (Wang et al., 2007) and sediment resuspension when near the bottom (Bourgault et al., 2014; Boegman and Stastna, 2019).

Internal waves can be generated by wind stress on lakes (Farmer, 1978; Pannard et al., 2011), the interaction of tide and topography (Lee and Beardsley, 1974; Alford et al., 2015), ship wake (Watson et al., 1992; Grue et al., 2016) or by the gravitational collapse of mixed fluids (Maxworthy, 1980), the later being the main focus of this article.

Initially studied as internal gravity current, in partial or full-depth lock-exchange experiments (Sutherland et al., 2004a,b; Cheong et al., 2006), the gravitational collapse of mixed fluids was only recently observed in the ocean. Nash and Moum (2005) observed this mechanism at the mouth of the Columbia River when a freshwater plume flowing as a gravity current into the coastal ocean released internal waves. Wang et al. (2019) found similar obser-

vations with the discharge of fresher water by the Fraser River. In a fjord context, Bourgault et al. (2016) published clear observations, supported by numerical simulations, that internal waves may arise from a frontally forced gravity current intruding into a two-layer stratification. However, the relationships between the properties of the generated internal waves (wavelength, amplitude, energy) and the background and forcing conditions (surface layer thickness, shearing, Richardson and Froude numbers) remain unclear.

In an attempt to solve this issue, two oceanographic campaigns were organized to collect new evidence of internal solitary waves generated by frontally forced intrusions in the Saguenay Fjord. Along its narrow, long and steep morphology, the Saguenay Fjord possesses three sills at depths of 20, 60 and 120 m located respectively at 2 km downstream, 18 and 32 km upstream of Tadoussac (Fig. 5). These particular topographic features divide the fjord in three basins. They are also known to cause mixing which modifies the water properties at various depths (Bourgault et al., 2012; Belzile et al., 2016; Galbraith et al., 2018) and generate internal solitary waves (Janes, 2008; Bourgault et al., 2011) (Fig.5).

Here we present observations of internal solitary waves generated by frontally forced intrusions in the Saguenay Fjord and results from idealized numerical simulations.

1.2 Methodology

1.2.1 Field observations

A field experiment was carried out from the 4th to the 9th of July 2017 and from the 2nd to the 9th of July 2018 near Anse-de-Roche and the 2nd sill of the fjord (Fig. 6).

As in Bourgault et al. (2016), the strategy consisted in using the Colvert, a 9 m long DFO research boat with an approximate draught of 1 m, to sample through internal wave surface patterns visible from the shore during calm conditions. The boat towed a Biosonics Biofins body equiped with a 123 kHz Biosonic echosounder and a Teledyne Sentinel V 500

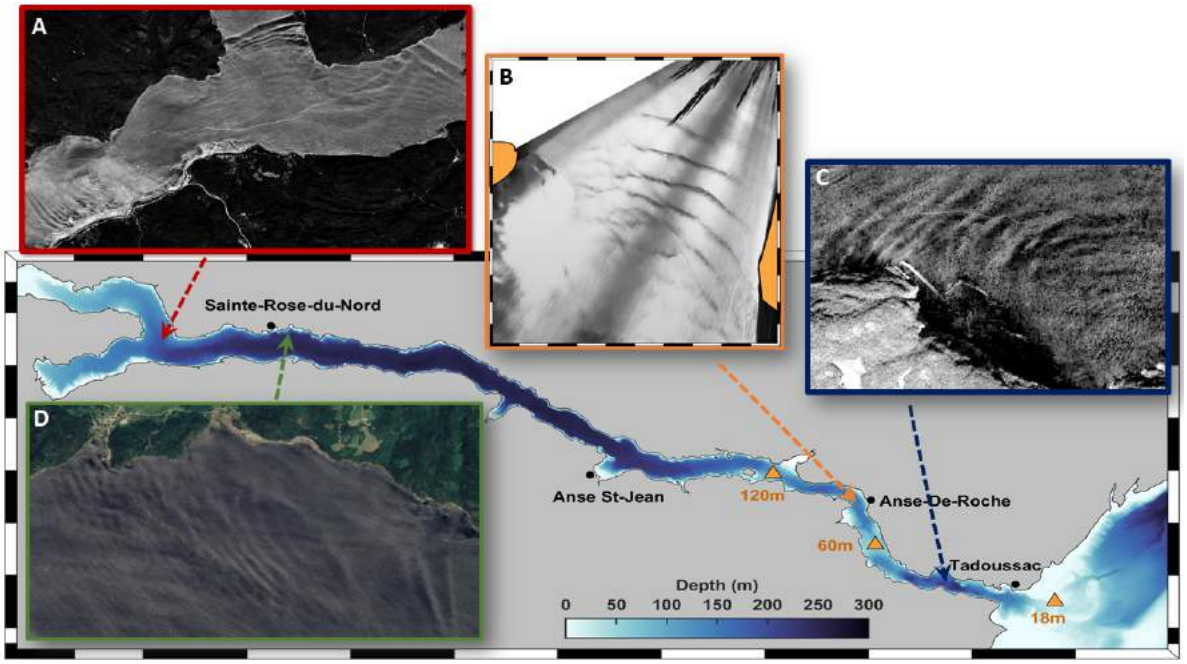

Figure 5: Bathymetric map of the Saguenay fjord with the sills (yellow triangles) and theirs respective depths. A) Satellite image taken on September 9 2012 showing internal waves, obtained via Google Earth Pro. B) Georectified image taken on the 6th of July 2017 showing internal solitary waves propagating upstream near Anse-de-roche. C) Satellite image taken on August 30 2018 showing the upstream propagation of internal waves, obtained via Google Earth Pro. D) Satellite image of internal waves near Sainte-Rose-du-Nord, captured on September 12 2017 and obtained via Google Earth Pro

kHz acoustic Doppler current profiler (ADCP) mounted on it. A Sea-Bird SBE 19+ CTD probe and a Garmin GPSmap 76Cx were used to, respectively, profile the water masses and log the ship track. Unfortunately, the CTD profiler was lost at sea during the 2018 campaign.

For the 2017 oceanographic campaign, the velocity data were acquired at a frequency of 2 Hz and at a vertical resolution of 0.5 m. During processing, the data were averaged to a temporal resolution of 10 s and 1 m vertically. The current profiler was not equipped with bottom-track nor real-time features in this campaign. However, during the expedition in July 2018, the current profiler was equipped with real-time and bottom track features. The data were acquired in 4 s ensemble averages and 0.5 m vertical bins, then processed to a 16 s and 1 m resolution. The sea surface temperature was measured from the ADCP temperature

sensor. For both campaigns, the horizontal velocity field was rotated to extract the along and across track components, allowing us to obtain a better visualisation of the fronts, intrusions and IWs sampled, considering that our methodology consisted of crossing as perpendiculary as possible theses features.

The Conductivity-Temperature-Depth profiler was deployed at an approximate falling speed of 1 m s^{-1} with a sampling frequency of 4 Hz. The data processing was done using Seabird instruments software.

An observer positioned on land, over a promontory, helped the onboard crew to navigate across the patterns by communicating the location of front and IW surface signatures.

A Canon EOS 6D camera with a 18 Mpixels resolution positioned at Cam1 on fig. 6, which is at 48.2240 °N, 69.8752 °W and 88 m above the water surface, took oblique pictures of the bay of Anse-de-Roche at an interval of 60 s. Only on the 9^{th} of July 2017, the camera was deployed at 48.1973 °N, 69.8608 °W at an elevation of 73 m (Cam2 on fig. 6). The camera was set to turn itself on during daylight, allowing the capture of more than 11 000 frames. Thoses images were later calibrated to remove lens distortion (Heikkila and Silven, 1997), stabilized to correct the small motions of the camera between each shot (Farid and Woodward, 2007) and georectified using the g_rect Maltab package (Pawlowicz, 2003; Bourgault, 2008; Bourgault et al., 2020). The georectification technique consists in determining the geographic coordinates of each pixel of a given image by providing the best guesses to a variety of camera parameters such as the field of view, geographical position, etc. The georectified images were used to calculate distances and extract internal wave properties such as wavelength and ground velocity using M_map toolbox (Pawlowicz, 2020). Also multiple timelapses were made to visualize the formation and behavior of fronts and internal waves by observing the sea surface pattern they produced.

In an attempt to use the ice floes as surface tracers, an exploratory winter campaign was carried out between March 10 and March 15 2019 near Anse-de-Roche in the Saguenay Fjord.

Two DJI Mavic 2 drones equipped with a 20 Mpixels Hasselblad camera and a 18 Mpixel Canon EOS 6D camera were deployed daily to capture sea surface patterns with the hope of capturing internal solitary waves propagation with the periodic divergence and convergence of ice floes along its motion. The same approach was used to detect front formation and displacement with the convergence of ice floes over certain lines. The images captured were processed with the same methodology as those obtained in July.

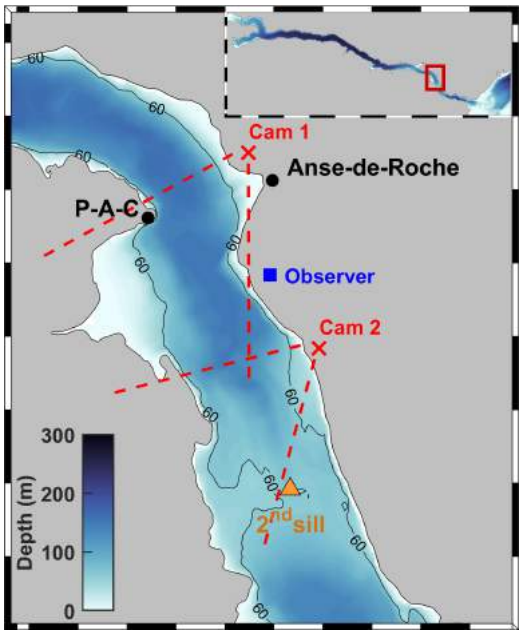

Figure 6: Bathymetric map of Anse-de-Roche bay, near the 2nd sill. Black contour line is the 60 m isobath.

1.2.2 Numerical simulations

To explore the vast parameter space involved in the frontally forced intrusion mechanism, over 50 different idealized simulations were carried out using a similar initial setup as in Bourgault et al. (2016). Introduced by Bourgault and Kelley (2004), a 2-D laterally averaged nonhydrostatic ocean model solving the non-rotating 2-D Euler equations with second-order finite differences was used to simulate the frontally forced intrusion mechanism.

1.2.2.1 Simulation frame

Every simulation were conducted in the $x-z$ plane with a flat bottom topography, open boundaries conditions with a basin of a constant depth of 150 m. The model grid is a 2636 $\times$ 66 points variable-mesh Arakawa-C type (Arakawa, 1966; Bourgault and Kelley, 2004) where the spatial resolution decreases away from the central [-1 km, 1 km] domain. The horizontal grid size, Δx, is 1 m from -1000 m to 1000 m, then decreases to reach Δx = 1000 m at 20 km on each side of the front. The vertical resolution from the surface to -30 m is Δz = 1 m and exponentially decreases to Δz = 5 m at 73 m below the surface. The horizontal and vertical domains are respectively bounded by the [-200 km, 200 km] and [-150 m, 0] intervals. The initial timestep used to solve the equations, Δt_0, is 0.1 s. After a few iterations, Δt is calculated at each timestep to meet a third of the Courant-Friedrichs-Lewy condition (Bourgault et al., 2014),

$$\Delta t = \frac{1}{3}\min\left\{\frac{\Delta x}{\mid u_{\max} \mid}, \frac{\Delta z}{\mid w_{\max} \mid}\right\} \tag{1.1}$$

where $\mid u_{\max} \mid$, $\mid w_{\max} \mid$ are the absolute maximum value of the currents inside the high resolution part of the grid at the previous timestep.

In order to limit the size of the data, the model gives output for all variables at a period of $\sim$ 5 s, excepted for the energy flux where the output timestep is Δt.

1.2.2.2 Initial conditions

The initial density field is separated in three water masses with different densities, with two surface waters (ρ_1, ρ_2) separated by a front of a certain width (L) centered at x = 0 m overlying the bottom denser water (ρ_0) (fig. 7). The surface waters ρ_1, ρ_2 are separated from the bottom water ρ_0 by a pycnocline of half-thickness d_1, d_2 centered at a depth of h_1, h_2. The vertical density profiles follow an hyperbolic tangent shape where ρ_i, ρ_0, d_i, h_i modulate its steepness. The same function is used to create the front, except L modulates the horizontal

gradient instead of d_i, h_i, ρ_0. This setup represents an idealization of the observations made by Bourgault et al. (2016).

The initial horizontal velocity field is similarly shaped to the density field. There are two surface velocities u_1, u_2, respectively associated with the surface waters ρ_1, ρ_2 and transition from those two velocities follows the front with an hyperbolic tangent function with u_i, L, x as variables. However, the velocity field of the deeper water (ρ_0) comprises two components u_{01}, u_{02}. The first one is the velocity field below the surface water ρ_1, which is on the left side of the front. The second component, below ρ_2, u_{02}, is initially calculated to balance the transport on each side of the front using the following equation :

$$\int_{-H}^{0} u_l \, dz = \int_{-H}^{0} u_r \, dz \tag{1.2}$$

where u_l, u_r are respectively the initial velocity field on the left and the right side of the front.

The initial vertical velocity field is given by integrating vertically the continuity equation along the $z-$axis, this is to assure that the initial flow is non divergent.

$$w(x, z, t = 0) = -\int_{-H}^{z} \frac{\partial u}{\partial x} \, dz \tag{1.3}$$

The Richardson ($\mathrm{Ri_i}$) and composite Froude ($\mathrm{Fr_i}$) numbers were computed on both sides of the front where $\mathrm{Ri_i}$ is computed as :

$$Ri_i = \frac{N_i^2}{S_i^2} \tag{1.4}$$

and the buoyancy frequency on each side of the front is given by $N_i^2 = -\frac{g}{\rho_0}\frac{(\rho_i - \rho_0)}{2d_i}$ and the vertical shear by $S_i^2 = \left(\frac{(u_i - u_{0i})}{2d_i}\right)^2$. The composite Froude number is calculated as :

$$Fr_i = \sqrt{\frac{u_i^2}{g_i' h_i} + \frac{u_{0i}^2}{g_i'(H - h_i)}} \tag{1.5}$$

with $g_i^{'} = 2d_iN_i^2$.

These adimensional numbers were calculated before launching the simulations to make sure that the initial flow is stable, $\mathrm{Ri_i} > 0.25$ and subcritical, $\mathrm{Fr_i} < 1$.

The depth-integrated perturbation energy flux, $F_i^{'}$, is calculated in two different ways at 1000 m away on each side of the front and for each iteration. Both methods decompose the horizontal velocity as $u = U + u'$ where U and u' are respectively the mean current and the perturbation component.The background vertical velocity is $W = 0$ such that $w = w'$. The horizontal background velocity profiles are defined as the mean current at $t = 0$ s and $x = \pm 1000$ m. Although being similar, the two methods computed the perturbation kinetic energy differently.

The first one, used for example by Martin et al. (2006), computes the perturbation kinetic energy with $E_k = \frac{\rho}{2}(u'^2 + w'^2)$ where u' is given by subtracting the background current to the total current, $u' = u - U$. By using this method, the perturbation kinetic energy density is always positive.

The second method, presented in Lamb (2010), computes the change in perturbation kinetic energy by subtracting the background kinetic energy from the total kinetic energy as $\Delta E_k = K_{tot} - K_b$ where :

$$K_{tot} = \rho\left(\frac{U^2}{2} + Uu' + \frac{u'^2 + w'^2}{2}\right),$$
$$K_b = \rho\frac{U^2}{2}$$

leading to :

$$\Delta E_k = \rho\left(Uu' + \frac{u'^2 + w'^2}{2}\right),$$

As opposed to the previous method, this one may produce negative values if $U < \frac{-u'}{2}$, indi-

cating that the passing of the internal waves reduces the total kinetic energy in comparison of the initial state.

It's worth noticing that both methods give the same energy value if the background velocity field is motionless. The results presented in this article are produced with both methods but the interpretation and discussion will focus on the first one.

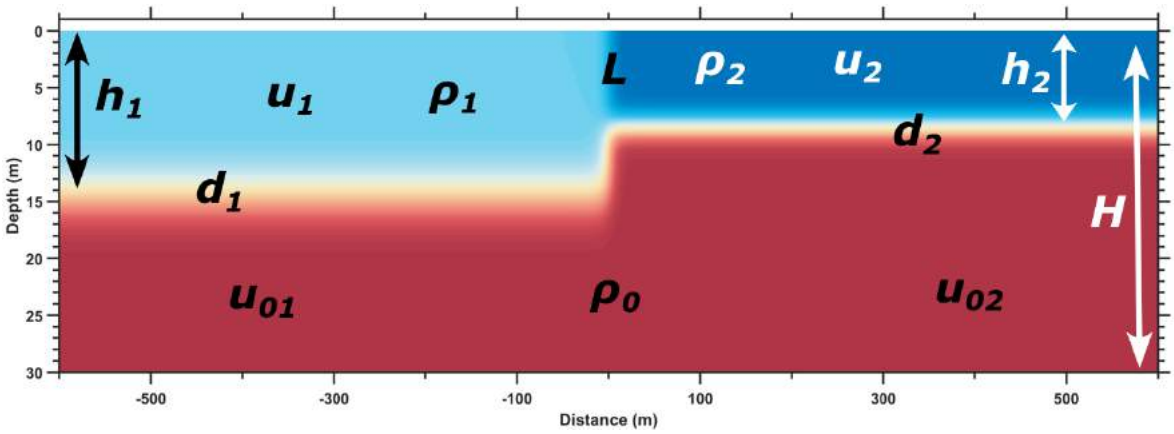

Figure 7: Required initial variables by the 2-D model, where ρ_i refers to density, u_i to velocity, h_i to surface layer thickness, d_i to half the pycnocline thickness, L the front horizontal scale and H the maximum depth

1.2.2.3 Data Analysis

In order to match the internal waves properties with the perturbation energy they contain, the amplitude A, the wavelength λ and the mean phase velocity c_p were calculated at ±1000 m. The amplitude is measured by finding the maximum vertical displacement of the interface between ρ_i and ρ_0 relative to the unperturbed state.

The mean phase velocity c_p was calculated by dividing the distance between two selected positions x_1, x_2 and the time taken by the internal wave trough to travel between them, that is,

$$c_p = (x_1 - x_2)/(t_1 - t_2)$$

with $x_1, x_2 = -1000, -960$ for IWs that propagate leftward, and $x_1, x_2 = 1000, 960$ m for a rightward propagation.

The wavelength was computed by integrating the position of the pycnocline η between two selected points that comprise the entire wave x_1, x_2 (Michallet and Ivey, 1999) :

$$\lambda = \frac{1}{A} \int_{x_1}^{x_2} \eta(x)\, dx.$$

Given that more than a dozen internal waves can be generated in some simulations, and on occasion, outside the high resolution part of the grid, we restrain our study to the first 3 internal waves generated on each side of the front, provided that the vertical displacements of the waves is greater or equal to 1 m, which equals Δz in the high resolution part of the grid. These thresholds are used to effectively compare runs between them.

We computed the intrusion mean velocity by finding the time taken by the head of the intrusion to reach ±200 m. As opposed to the intrusion velocity, the speed of the front is obtained by locating the density gradient at the surface for each time step and then calculating the slope of that position against time. Note that this method can be misled by large surface density gradients caused by other phenomena than fronts such as those caused by trapped cores. Visual inspections were made to manually detect these and correct these cases. The front and intrusion velocities are negative if the physical feature propagates leftward.

To obtain the perturbation energy contained in a single internal wave, the perturbation energy flux time series F_i is passed through an envelope filter to remove the trend induced by the varying background condition set by the intrusion. Then $F_i^{\cdot}$ is integrated along time as :

$$E_p = \int_{t_1}^{t_2} F_i^{\cdot}\, dt$$

where t_1, t_2 are times that completely capture the IW.

1.3 Results

1.3.1 Observations

After nearly a week of oceanographic campaign in July 2017 and July 2018, only a handful of internal waves generated by the frontally forced intrusion mechanism were observed. Furthermore, most of the observations only provide partial evidences, as we have not been able to capture a complete sequence of a front, an intrusion and IWs as clearly as did Bourgault et al. (2016). We have come to realize that although these features may be widespread, they are difficult to find and to measure completely and to identify unambiguously within the extraordinary complexity of natural tidal flows in a silled fjord. Also many technical difficulties occurred with the ship and the scientific equipment that reduced the number of days at sea and caused a sporadic lack of velocity data. Nevertheless, fronts, intrusions and internal waves were individually observed a few times. Overall, relevant quantitative information were extracted from the georectified and acoustic images as well as velocity field, allowing us to better understand the mechanism that generate IWs from frontally forced intrusions.

On the 7th of July 2017, $\sim$ 1 h before the time of low water at Tadoussac, multiple transects, located 2 km upward of the 2nd sill, were carried out through a front from 11:58 to 13:05 Z. Figure 8a, taken between 12:00 to 12:04Z, is the most eloquent image of the physic processes occurring during that period, where we can clearly see the front and the intrusion on the echogram. The depression of the pycnocline, $\Delta h \sim 5$ m, between -150 m and 0 m, and its wavy shape under the front (-100 to 100 m) is similar to the intrusion observed by Bourgault et al. (2016) in their idealized simulations. Therefore, we interpret that the water mass downstream of the front is intruding underneath the upstream side one, which is consistent with the downcast density profiles (fig 8b) since the denser surface water is located on the downstream side. However, this interpretation remains qualitative due to the lack of

velocity data.

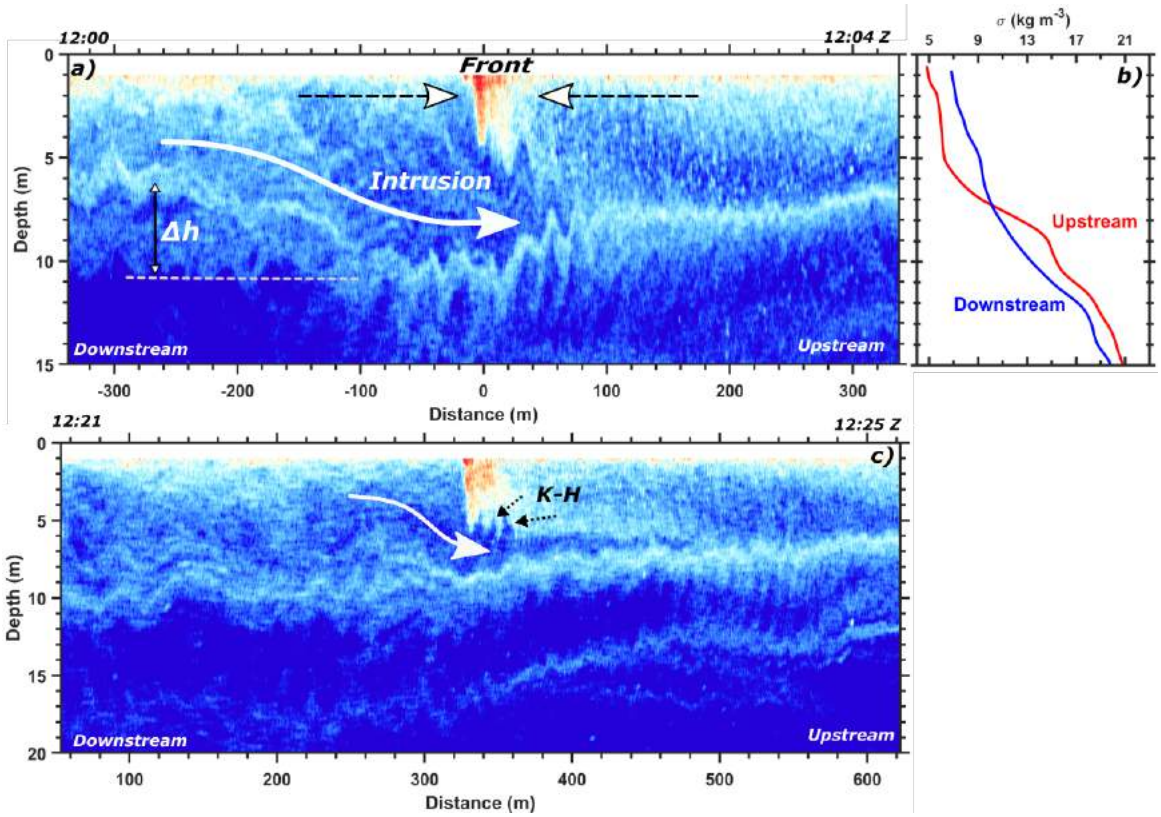

Figure 8: a). Acoustic image of a front, red echo, and the beginning of an intrusion sampled in July 7th 2017. Dashed arrows are an interpretation of the surface velocity. b). Density profile on each side of the front, collected at 12:33Z for the upstream cast and 12:44Z for the downstream cast. c) Acoustic image of the same intrusion taken between 12:21 and 12:25Z.

Acoustic images collected during the following transect show the same front-intrusion pattern, some with evidence of Kelvin-Helmholtz instabilities (fig8c), but no internal solitary waves were observed. By comparing the fronts positions between the two transects, the front velocity is approximated to 0.25 m s^{-1}. As sampling went on, the front and intrusion faded away to become unclear on the echogram around 13:05Z.

On July 9th 2017, from 12:39 to 12:42 UTC, we sampled through a clear front (fig 9b.) near the 2nd sill of the fjord. The sampling occurred ~ 1 h before the low water time at Tadoussac during a spring ebb tide of $\Delta\eta$ = 3.1 m. The boat crossed the front in a southwest

- northeast direction at ~ 45° angle relative to the front direction around 12:40Z, indicated by the change of sea surface temperature, ΔT = 1.7 °C, (fig 9 b). The acoustic image of the track (fig 9a) shows the front signature, the red echo from 12:40:10 and 12:40:30, and a V-shaped pattern between it and the pycnocline suggesting that an intrusion was forming. However, the velocity field in this sequence doesn't show the presence of an intrusion.

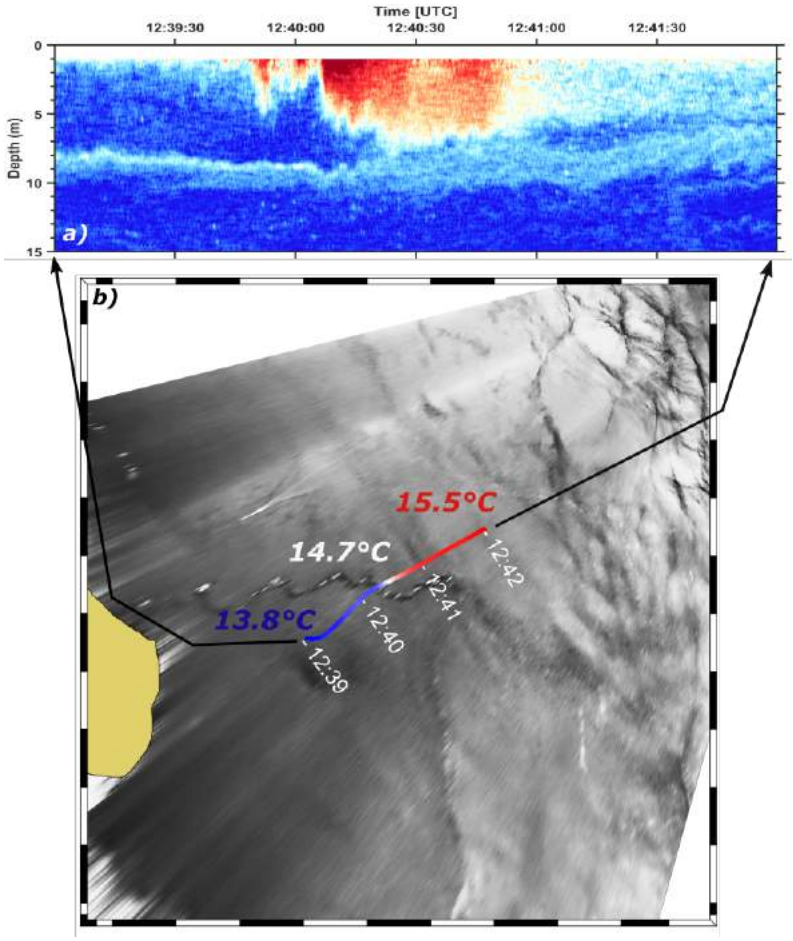

Figure 9: b). Sea surface patterns at 12:39:02 UTC on July 9th 2017 with the ship track and the sea surface temperature (multicolored line) across a front. a). Acoustic image of the first 15m below the surface along the ship track.

On the same day, around the time of low water at Tadoussac (~ 13:45 Z), a sequence composed of a front, an intrusion and internal waves was observed 1.7 km upstream of the 2nd sill. The essence of these features were captured by the echosounder and the shore-

based high resolution camera between 13:45 and 13:52 Z during a westward transect. The echogram (fig 10a) shows an intrusion, from 13:45:40 to 13:48:00 Z, and a solitary wavetrain from 13:48 to 13:50 Z. The intrusion is approximately 10 m thick and extends for $\sim$ 500 m along the boat track. The wavetrain is composed of three waves with amplitudes ranging from 7 m, for the one close to the intrusion head, to 10 m for the farthest one. Their respective wavelength, starting from the one closer to the intrusion, are $\sim$ 70, 70 and 90 m. Also, the georectified image captured at 13:47 Z (fig 10b) shows several stripes, signature of a solitary wavetrain, and a front located east of the transect. Despite being well defined on figure 10b, the exact front position was difficult to figure out by the crew on the boat at that time, such that it was not sampled. This explains the absence of any front signature on the echogram. Unfortunately, the density profile wasn't measured on neither side of the front and the current profiler was found unplugged at the end of this sampling, explaining the absence of velocity data and quantitative information about this sequence.

On the last day of the 2018 field expedition, the 9th of July, we carried out several transects over internal waves surface patterns located 3 km downstream of the 2nd sill and propagating westward. The sampling took place between 17:23 and 19:15 Z, roughly 2 h after the time of high water at Tadoussac during a neap ebb tide of $\Delta\eta$ = 2.5 m. The most representative transect that shows the physical processes observed during that time is the one captured from 18:28:40 to 18:33:30 Z (fig 11). The boat was travelling eastward toward a front near the shore, while crossing the internal waves first. Figure 11a shows, from 0 to 300 m, a not so well defined internal solitary wavetrain. Nevertheless, the ISW become clearer when looking at the horizontal and vertical velocity fields (fig 11b,c). The horizontal (along-track) velocity field shows patches of negative velocity while propagating in a positive horizontal velocity background. Also, a stripe pattern of positive and negative vertical velocities, typical signature of internal waves, is observed on figure 11c.

As opposed to the ISW, the intrusion is well defined on the echogram and is coincident with a tongue of negative velocity observed on the along-track velocity field. The intrusion

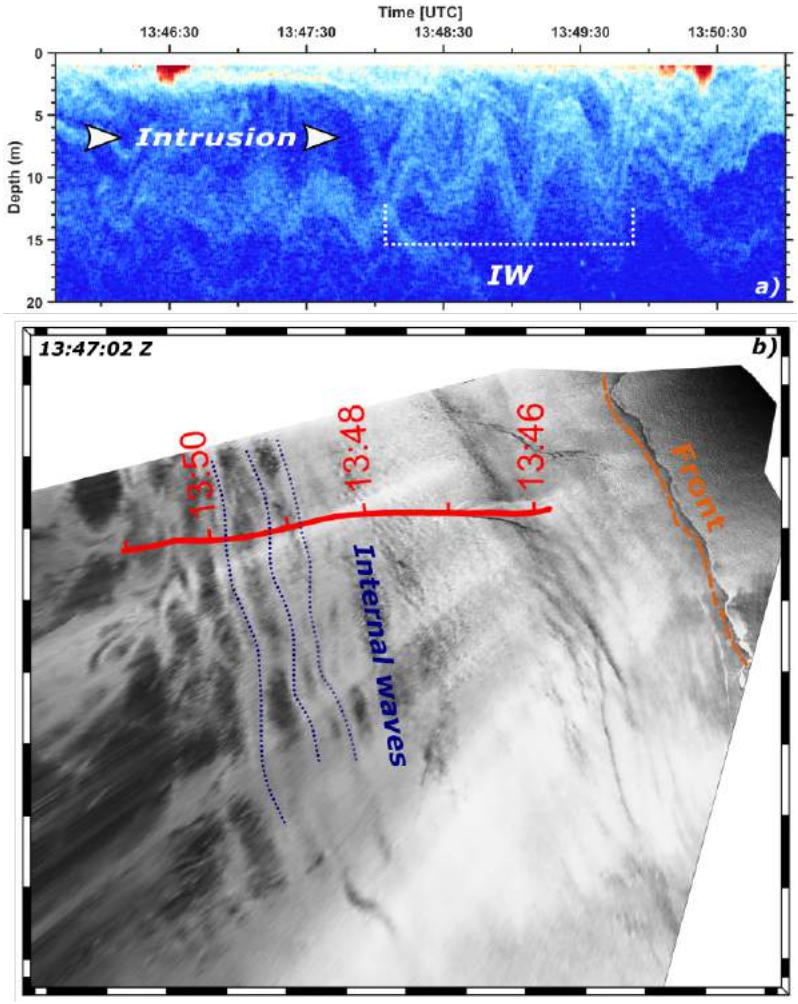

Figure 10: b). Sea surface patterns at 13:47:02 UTC on July 9th 2017 with the ship track with illustrations of the front and internal waves (orange and blue lines). a). Acoustic image of the transect (red track in b) showing the intrusion and the formation of internal waves.

is approximately 5 m thick with the head located around 510 m. The lack of density profiles prevent a more quantitative interpretation of the physical features presented here. This sampling was out of the field of view of the camera,such that no information about the wavelength and ground velocity were calculated.

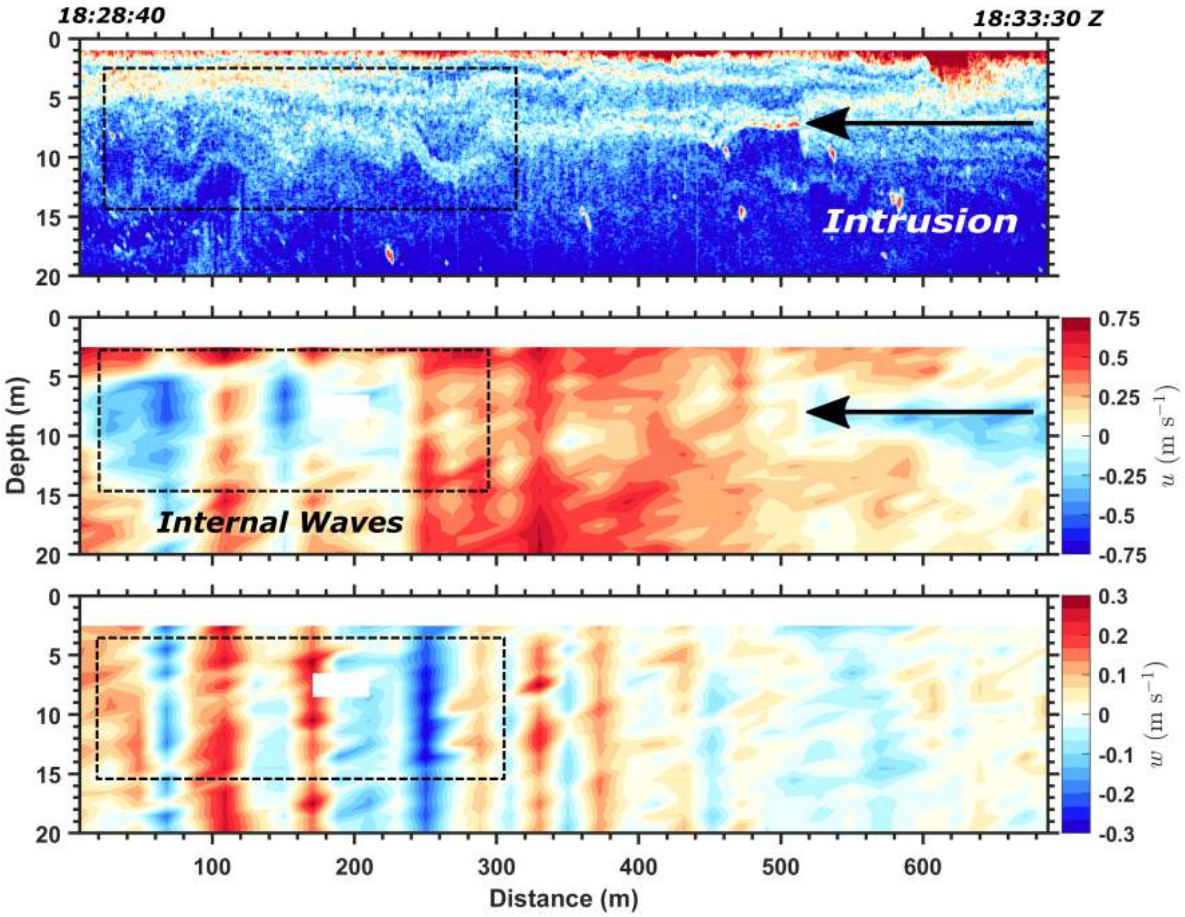

Figure 11: a) Echogram, b) Along-track velocity field, c) Vertical velocity field. Data were collected July 9th 2018 from 18:28:40 to 18:33:30 Z

1.3.2 Numerical simulations

To further the understanding of the frontally forced intrusion mechanism and to compensate for the rather low number of occurrences collected during the field expeditions, idealized numerical simulations were conducted to explore how the physical properties of the processes involved vary as a function of the changing environmental conditions. As a starting point, we recreated the first 4 runs made by Bourgault et al. (2016) with slight differences concerning the highest spatial resolution of the grid, Δx_{min}, Δz_{min} = 1 m instead of 0.5 m as presented in their article, but the initial velocity and density fields were identical. The objec-

tive here is to test the model sensitivity to a lower resolution since a considerable number of simulations need to be carried out. We then compared the simulations with those made by Bourgault et al. (2016) to see if we obtain similar results in term of internal waves properties such as number of waves, amplitude, wavelength and perturbation energy.

To explore the parameter space involved in this mechanism, 48 additional simulations were carried out using different initial conditions. Those new configurations were designed mainly to study the sensitivity of the results to changes in the stratification and layer thicknesses. These experiments really only explore a subset of the entire parameter space that characterizes this complex problem. The control parameters of each of these experiments are listed in Table 9 in the appendix.

1.3.2.1 Typical cases

After exploring a wide range of control parameters, many simulations can be classified into two typical cases based on their intrusion shape and how the water masses reach gravitational equilibrium. The first case is exemplified by the simulation made by Bourgault et al. (2016), which is, in our study, run #1 as seen in Figure 12.

In this run, internal waves propagate on both sides of the front, the intrusion has a quasi-rectangular shape with a rounded head (figure 12c,f), and the interface between ρ_1 and ρ_2 is dynamically unstable, with the presence of Kelvin-Helmholtz instabilities. The surface layer thickness of the lighter water is thinner than the denser one, i.e $h_1 > h_2$, such that this configuration creates a negative (leftward) horizontal density gradient between the surface, $z = 0$ and $z = h_2$ and a positive (rightward) horizontal density gradient between $z = h_2$ and $z = h_1$. As time evolves, the intermediate water, ρ_1, intrudes underneath the lighter water, helped by the initial velocity u_1, and generates large amplitude internal waves at its well defined head.

Although being initially motionless, simulation #7 shown in Figure 13 exemplifies the

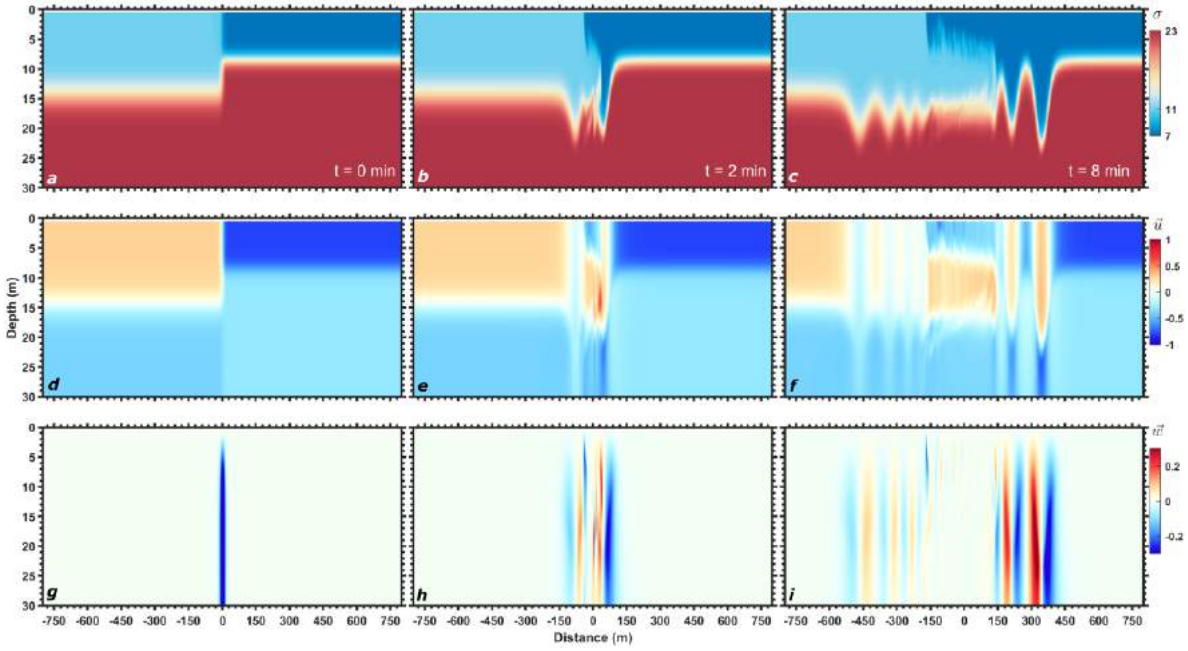

Figure 12: Evolution of simulation #1 at $t = 0, 2, 8$ minutes. a-c) Density field, d-f) Horizontal velocity field, g-i) Vertical velocity field. Units are kg m^{-3} for σ and m s^{-1} for the velocity fields.

second typical case encountered throughout this experiment. As opposed to the first case, h_1 is greater than h_2 which causes a leftward horizontal density gradient from $z = 0$ to $z = h_2$ as seen in Figure 13. With this initial condition, the entire surface layer tends to move leftward with the density gradient as opposed to the dual direction established when $h_2 < h_1$, in the first case. As a result, a conic shaped intrusion with no defined head is generated, large amplitude ($\frac{A_1}{h_1} = 0.8$) internal solitary waves are produced on the left side of the front and small oscillations ($\frac{A_2}{h_2} < 0.07$) on the right side. Dynamic instabilities are also formed at the ρ_1, ρ_2 interface. The pycnocline on the right side of the front rises at an mean rate of 0.8 cm s^{-1} until it reaches 10.5 m. Its seems that the initial motionless setup does not favor the formation of a well defined intrusion head that will impinge on the pycnocline to generate large amplitude IWs.

Simulation #33, shown in Figure 14, illustrates the second typical case with the pres-

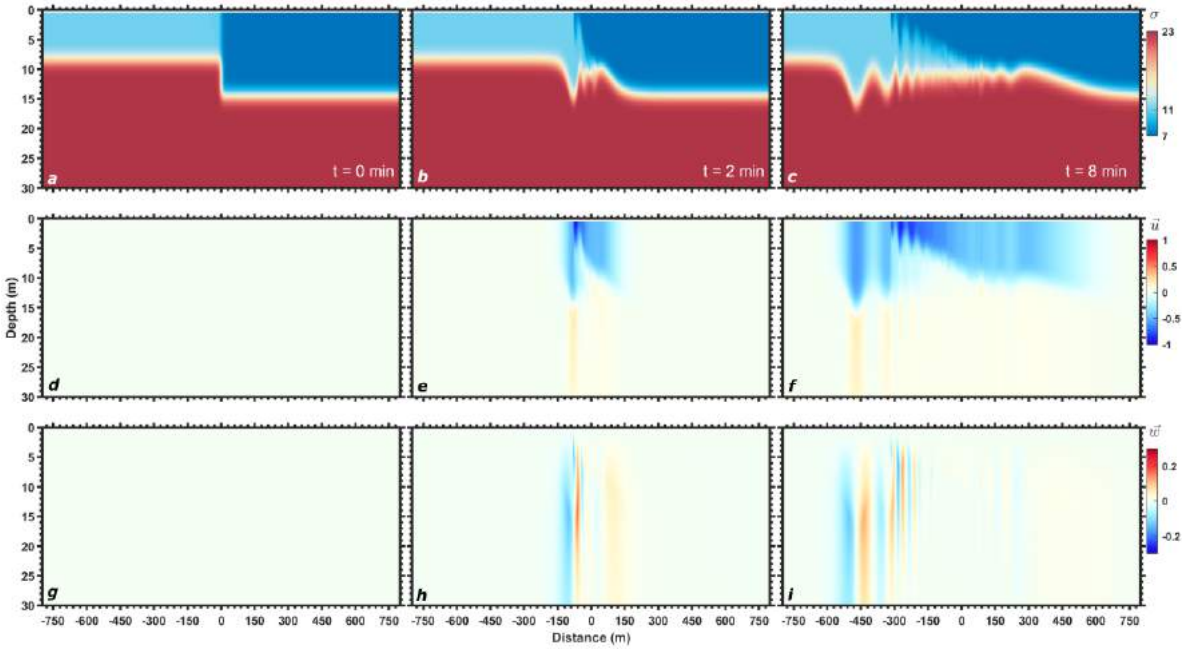

Figure 13: Evolution of simulation #7 at $t = 0, 2, 8$ minutes. a-c) Density field, d-f) Horizontal velocity field, g-i) Vertical velocity field. Units are kg m^{-3} for σ and m s^{-1} for the velocity fields.

ence of an initial velocity field. Similarly to run #7, $h_1 < h_2$, which tends to move the surface layer leftward, but also $|u_2| > |u_1|$, thus increasing the leftward motion by adding more kinetic energy on the right side. In comparison to run #7, a smaller barely defined conic shape intrusion is formed (Figure 14f) and larger IWs and instabilities are generated. Trapped cores reaching the surface are also observed (Figure 14c).

Overall, the majority of the simulations fits in one of these two typical cases which essentially depend on the pycnocline bump and the initial velocity. However, some simulations cannot be categorized in any of these two categories either because the initial Froude number is critical (Fr > 1), because the horizontal density gradient across the front is too small or because the environment is not stratified enough, that is $d_1/h_1 > 0.5$

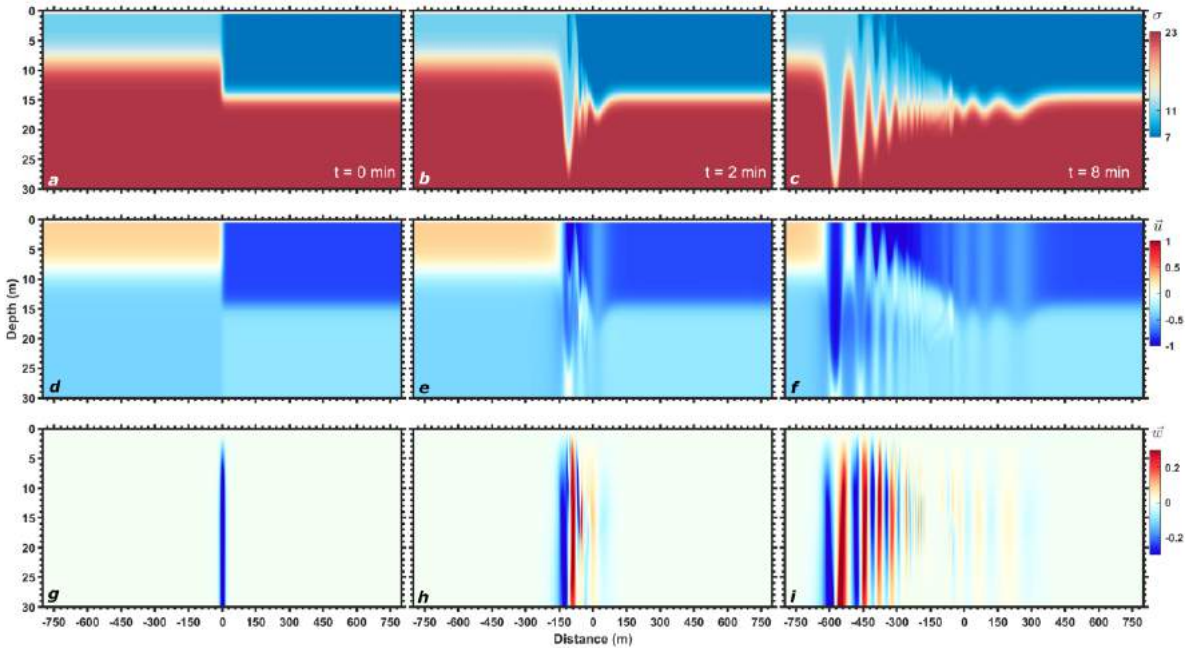

Figure 14: Evolution of simulation #33 at $t = 0, 2, 8$ minutes. a-c) Density field, d-f) Horizontal velocity field, g-i) Vertical velocity field. Units are kg m^{-3} for σ and m s^{-1} for the velocity fields.

1.3.2.2 Fronts

We now examine how frontal properties, such as front width (L) and frontal velocities v_f, affect the properties of internal waves. To examine these effects, 3 simulations (# 1,16,32, see Table 9 in Appendix 1) were performed with identical initial conditions, but with varying width (L) of respectively 20, 40 and 80 m. These simulations show that, over the range of values explored, the front velocity does not depend on the front width $v_f = 0.36$ m s^{-1} in all three runs. By also comparing the IWs properties, we found that the amplitude, the wavelength, the phase velocity and the perturbation energy are also roughly identical, with $A = 5 \pm 0.1$ m, $\lambda = 85 \pm 1$ m, $c_p = -1.1$ m s^{-1} and $E_k = -2.8 \pm 0.1 \times 10^4$ J m^{-1} for the first internal waves on left side of the front. The IWs properties on the right side of the front also show identical values.

In our simulations, the range of front velocity varies from -1.17 to 0.31 m s^{-1} depending

on the initial velocities and surface water densities, with an absolute minimum of 0.04 m s^{-1}. We observed that the front velocity remains fairly constant (Fig. 15a) throughout a run, independently of the presence of trapped core (Fig. 15b) and generation of internal solitary waves. This is seen in Figure 15, that shows a linear relationship between the front position and time.

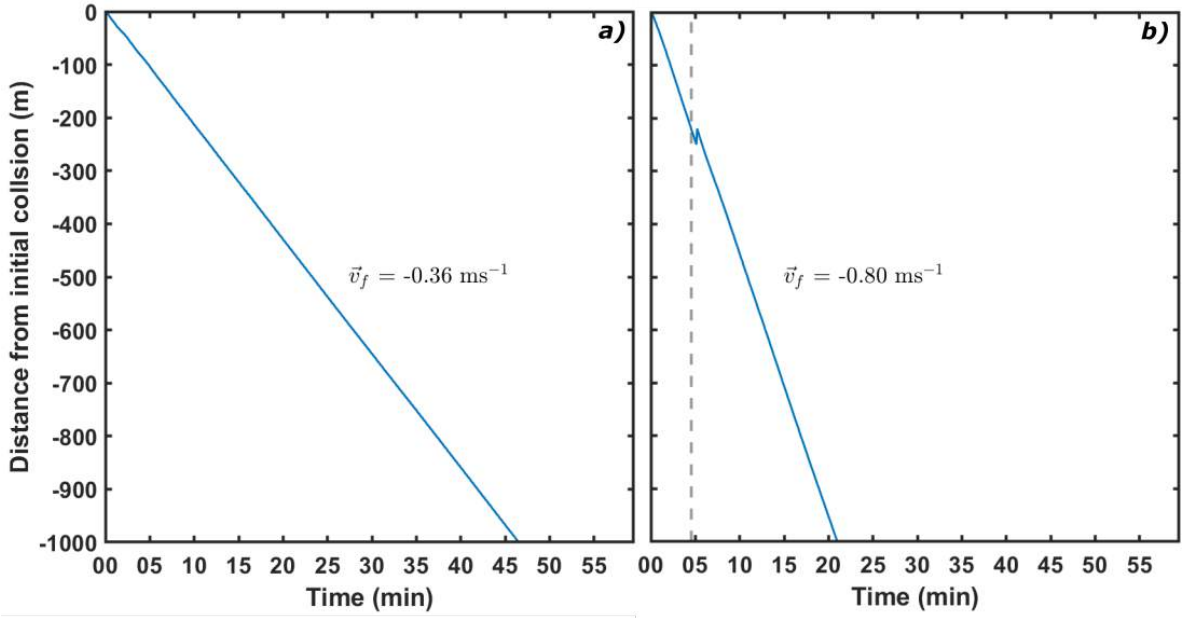

Figure 15: a) Position of the front in run #1, b) Position of the front (solid blue line) and trapped core detection (dashed gray line) in run #17

By grouping a certain number of simulations based on the nearly identical initial configurations they share, we can evaluate the impact of one parameter on the front velocity. As shown by the group #1, see Table 1, the absolute front velocity becomes greater as the surface density difference increases. The runs in this group were all designed with the same initial configuration, i.e. with no initial velocity, d_1, d_2 = 1.25 m and ρ_2, ρ_3 = 1007, 1023 kg m^{-3}, except for ρ_1 that has different value. Theses simulations have respectively a ρ_1 equal to 1009, 1011, 1014, 1017 and 1019 kg m^{-3} and a corresponding front velocity of -0.56, -0.66, -0.83, -0.91 and -0.96 m s^{-1}. Seeing this result, 2 additional sets of simulations were launched using a similar methodology, with each sets having identical initial conditions but

with a varying ρ_1. As opposed to the first set, these simulations were conducted with different surface layer thickness, $h_1 = h_2 = 14$ m for group #2 and $h_1, h_2 = 14, 8$ m for the third group. These simulations also show an increase of the absolute front velocity when increasing the surface density difference. Although the absolute front velocity in run #52 is the smallest in its group due to its smaller surface density difference, its front propagates rightward instead of leftward, as the other simulations do.

Table 1: Initial conditions for 3 groups of simulations. Units are in Meter-Kilogram-Second format, APE is in J m^{-2} and the front velocity v_f in m s^{-1}. A more exhaustive list of their initial parameters is available in Table 9 in Appendix 1

	run #	ρ_1	h_1	h_2	v_f	APE
Group 1	14	1009	8	14	-0.56	1058
	7	1011	8	14	-0.66	1456
	10	1014	8	14	-0.83	2069
	11	1017	8	14	-0.91	2725
	12	1020	8	14	-0.96	3402
Group 2	5	1011	14	14	-0.39	851
	19	1014	14	14	-0.58	1573
	20	1017	14	14	-0.79	2366
	21	1020	14	14	-0.91	3197
Group 3	52	1009	14	8	0.11	664
	49	1014	14	8	-0.18	786
	50	1017	14	8	-0.34	942
	51	1020	14	8	-0.59	1134

Grouping the previous simulations by their ρ_1, we studied the effect of the surface layer thicknesses (h_1, h_2) on the front velocity. For example, runs #10, 19, 49 have the same initial conditions but different surface layer thicknesses. They respectively have a $h_1 = 8, 14, 14$ m, $h_2 = 14, 14, 8$ m and a front velocity of -0.83, -0.57, -0.18 m s^{-1}. Similar results are obtained with runs #11, 20, 50 and runs #12, 21, 51. This suggests that the absolute front velocity

decreases as the surface layer thickness of the lighter water, h_2, is reduced. The hypothesis here, is that increasing h_2, as well as increasing the surface density difference, actually ρ_1 for theses examples, increases the available potential energy (APE) in the system. During the simulation, the system tends to a gravitational equilibrium state, where the lighter water ρ_2 is completely on top of the intermediate water ρ_1, and does this, by converting available potential energy into kinetic energy. Therefore, the more APE initially available, the faster the lighter water will try to "push" the intermediate water, and the same mechanism occurs for the intermediate water on the denser deep water, ρ_0. The available potential energy of simulations numbered #10, 19, 49, are respectively 2069, 1573 and 786 J m^{-2}, a decrease in absolute front velocity as the initial APE decreases is also observed in the other groups of runs. Four other simulations, see Table 2, were carried out using a similar setup, i.e. no initial velocity, $d_1 = d_2 = 1.25$ m, and h_1 and h_2 differ within them. As expected, an identical trend is detected, where an increase of the initial available potential energy leads toward a higher absolute front velocity.

Table 2: Varying initial conditions for runs in this experiments. Units are in Meter-Kilogram-Second format, APE is in J m^{-2} and the front velocity v_f in m s^{-1}. A more exhaustive list of initial parameters is available in Table 9 in Appendix 1

run #	h_1	h_2	v_f	APE
13	8	16	-1.04	4223
15	8	20	-1.17	6789
17	20	14	-0.80	3015
18	14	20	-1.12	6180

We observed a linear trend when plotting the volumic kinetic energy of the front, $K_f = \rho_0 v_f^2$ in relation to the initial available potential energy (Fig. 16). In order to characterize that trend, a linear regression was done to extract the correlation coefficient as well as the 95% confidence interval. We noticed that all simulations that featured a front (48), except for runs #33 and #45, are within the 95% confidence interval, and follow the linear trend. The coefficient of determination, $R^2 = 0.78$, indicates a strong linear correlation between the front

kinetic energy and the available potential energy.

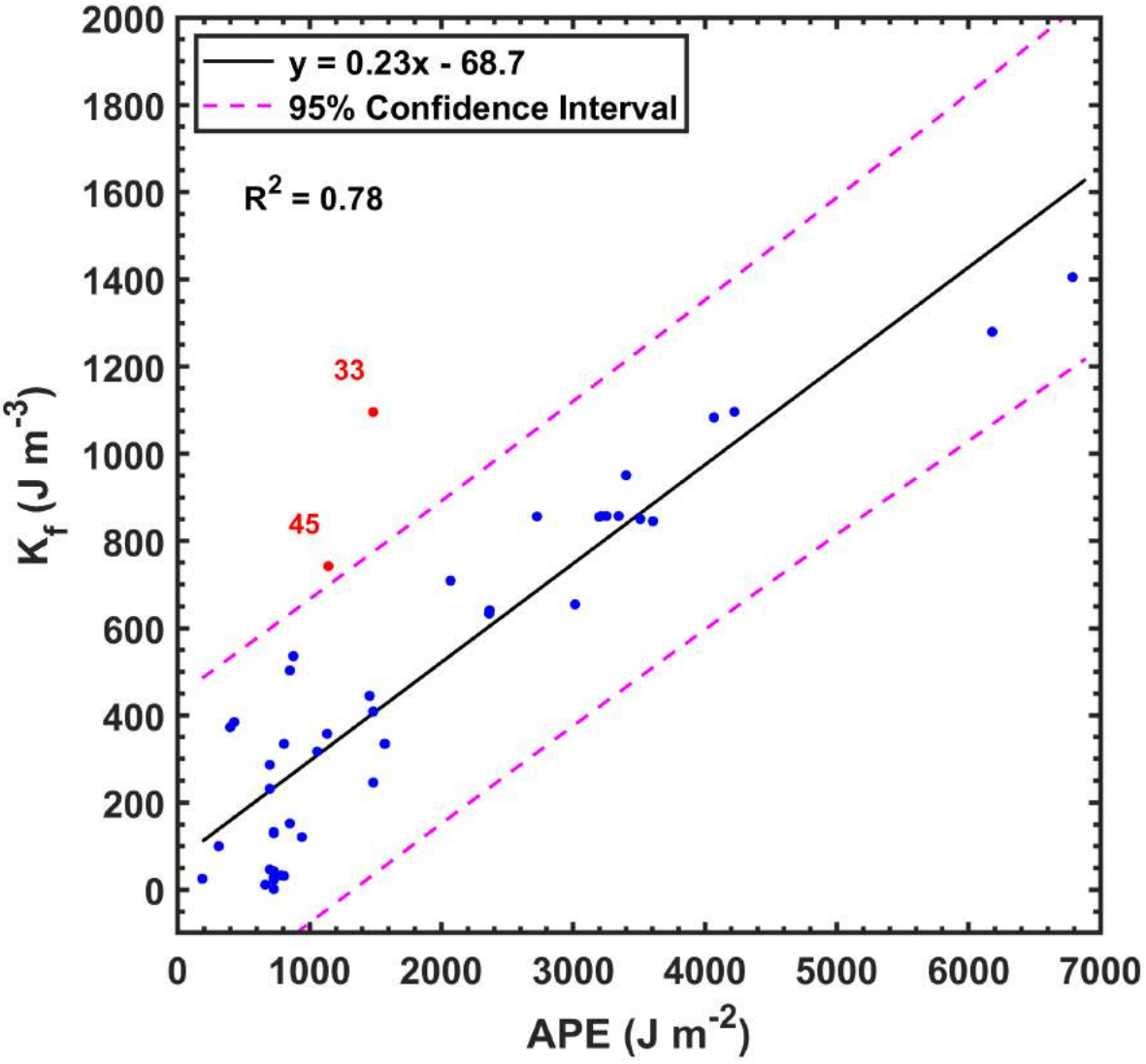

Figure 16: Linear regression (solid black) of the front kinetic energy in relation to the initial available potential energy for all simulations. Dashed magenta lines are the 95% confidence interval.

Runs #33 and #45 are not in the 95% confidence interval because the APE term doesn't take into account the initial kinetic energy of the surface waters. Although many other simulations have initial velocities, therefore initial kinetic energy, runs #33, 45 and 8 others have $|u_1| < |u_2|$. This initial configuration tends to increase the kinetic energy of the lighter water

without impacting the available potential energy term, causing an overestimation of the front kinetic energy term if we compare it to the APE only, even if several simulations with initial velocity follow the linear trend.

1.3.2.3 Difference of surface layer thickness

The role of the difference in surface layer thicknesses, $\Delta h = |h_2 - h_1|$, also referred to as the pycnocline bump, in the generation of IWs by frontally forced intrusion is not well understood. To assess this problem, we now examine whether a pycnocline bump alone can generate internal waves. For doing this, we configured two runs of the simplest possible case, that is two water masses separated by a sharp stratification with no initial velocity and $h_1 \neq h_2$, see runs #6 and 8 in Table 9. The results are IWs propagating in both directions for both simulations, although the amplitudes were much lower on the left side ($x < 0$), with $A_1 < 1$ m, compared to those on the right side that are characterized with $A_2 \sim 4$ m for the first IW. Although being characterized with small oscillations, the pycnocline on the left side rises more slowly compared to the right side. This disparity arises from the initial configuration where $h_1 > h_2$, with respective values of 14 and 8 m, thus creating an increasing horizontal density gradient starting at 8 m and pushing the denser water below 8 m leftward to reach gravitational equilibrium. We conclude from this exercice that a difference in the pycnocline height ($h_1 \neq h_2$) is sufficient by itself to generate IWs when there is only 1 surface layer.

To further the understanding of this process, we designed new simulations, this time with two surface waters standing over a denser deeper one. As used to study the front velocity, we formed subsets of runs that share a similar initial configuration where only 1 parameter varies throughout the different simulations. The first subset is configured with no initial velocity, $\rho_{0,1,2}$ are respectively 1023, 1011 and 1007 kg m^{-3}, $L = 20$ m, $d_1, d_2 = 1.25$ m and $h_1 = 8$ m, h_2 is the varying parameter in this group (Table 3).

The results of these simulations indicate that IWs with greater amplitude are generated

Table 3: 1^{st} subset of simulations used to characterize the pycnocline bump in regards to the waves properties. The properties are for the first 3 internal waves observed on the left side of the front. Units are in Meter-Kilogram-Second format.

run #	h_2	APE (J m^{-2})	A_1	λ_1	c_{p1}	E_1
7	14	1456	6.4	89	-1.3	5.87×10^5
			4.1	77	-1,1	3.19×10^5
			3.2	66	-1.1	1.17×10^5
9	20	4068	12.3	97	-1.3	2.02×10^6
			9.7	78	-1.3	1.11×10^6
			8.4	54	-1.1	0.76×10^6

when the surface layer thickness of the lighter water (h_2) increases. We also noted a higher perturbation energy (E_1) with higher values for h_2. In this configuration, IWs with amplitude greater than 1 m were generated exclusively on the left side of the front, except for one of 1.01 m of amplitude on the right side in run #9. However, it is uncertain, at this point, if the variation in the IW properties, mainly A and E, are caused by changing h_2 alone, or by the increase of Δh.

To answer this question, a second subset of initially motionless ($u_i = 0$) simulations with a varying h_1 and h_2 were carried out (see Table 4). The density of the surface layer are 1019 and 1007 kg m^{-3}, $L = 20$ m and $d_1,\ d_2 = 1.25$ m. Except for run #17, where a single IW of 1.6 m of amplitude and a traveling speed of 0.44 m s^{-1} was detected on the right side of the front, the IWs were generated and propagated on the left side.

By comparing runs #13 and #18, we observed that even if h_2 is greater in run #18, it produces IWs of smaller amplitude, but higher phase velocity and perturbation energy than run #13 (Table 4), proving that the maximum amplitude isn't only correlated with the thickness of the lighter surface water. However, we noticed in this group that the difference of surface layer thickness, Δh, is better correlated with the IWs amplitude, as A increases with a growing Δh.

Table 4: 2^{nd} subset of simulations used to characterize the pycnocline bump and the properties of the first two internal waves observed on the left side of the front. See Table 9 for the complete set of initial parameters.

run #	h_1	h_2	Δh	APE (10^3)	A_1	λ_1	c_{p1}	E_1 (10^6)
13	8	16	8	4.22	14.2 ∅	52 ∅	-1.15 ∅	1.63 ∅
15	8	20	12	6.79	15 5.4	58 37	-1.3 -1.15	3.12 0.64
17	20	14	6	3.01	12.9 ∅	149 ∅	-0.8 ∅	0.49 ∅
18	14	20	6	6.18	12.2 3.4	58 50	-1.3 -1.15	1.95 0.33

Note however that A can differ for identical values of Δh. For example, #17 has its thicker surface water associated with the intermediate water ρ_1 as opposed to run #18. This configuration generates different IW properties, even if the Δh remains unchanged. By comparing run #17 and #18, we observed a slight variation in the first IW amplitude, but the wavelength in run #17 is 3 times longer than in the rest of the group. We also noted that run #18 has a higher travelling speed and perturbation energy. The latter is thought to be linked with the increase of available potential energy in this simulation, which is coherent with the properties calculated in the rest of the group. As mentioned earlier, run #17 generated 1 IW on the right side of the front, which we think arises from a particularity in the initial configuration. At t_0, there is a negative horizontal density gradient from the surface to $z = h_2$, a feature observed in the other runs, but between $z = h_2$ and $z = h_1$, there is also a positive density gradient due to $h_1 > h_2$. This second feature tends to initially move a portion of the intermediate water to the right side of the front, thus increasing the intrusion velocity, 0.41 m s^{-1} compared to 0.27 m s^{-1}, therefore raising the quantity of energy impinging on the pycnocline.

To evaluate the effect of the pycnocline bump in a configuration with initial velocity, we designed 2 new simulations (#27,33) and compared their IW properties with those from simulation #1. The initial conditions of run #1 are an idealization of the observations made by Bourgault et al. (2016). Runs #27 and #33 use the same initial parameters excepted for h_1 and h_2, see Table 9. In their first numerical simulation, Bourgault et al. (2016) set $h_1 = 14$ m and $h_2 = 8$ m, therefore for run #27, h_1 and h_2 had values of 14 m, and in run #33, h_1 and h_2 were respectively set to 8 and 14 m. These three runs were initially stable and had a subcritical flow. As a result, IWs were detected on both sides in each simulation and trapped cores were observed on the left side in run #33. In the last simulation, only 2 IWs of amplitude greater than 1 m were detected on the right side of the front.

Table 5: 3^{rd} subset of simulations used to characterize the pycnocline bump and the properties of the first 3 internal waves observed on both sides of the front (E_i units are MJ m^{-1} and APE units are J m^{-2}). See Table 9 for the exhaustive set of initial parameters.

run #	h_1	h_2	APE	v_f	A_1	λ_1	c_{p1}	E_1	A_2	λ_2	c_{p2}	E_2
					5.1	86	-1.14	0.228	14.1	70	0.89	2.429
1	14	8	729	-0.36	3.3	73	-1.14	0.132	12.5	65	0.88	1.996
					2.5	62	-1	0.076	11.2	60	0.80	1.682
					14	86	-1.34	1.533	8.4	105	1	1.475
27	14	14	877	-0.72	9.7	75	-1.34	0.941	5.9	96	1	1.007
					8	66	-1.34	0.584	4.3	89	0.88	0.693
					20.2	61	-1.34	1.795	1.9	136	0.73	0.097
33	8	14	1484	-1.03	17	51	-1.14	1.203	1.2	112	0.67	0.054
					14.4	43	-1.34	0.815	∅	∅	∅	∅

Although runs #1, 27 and 33 share certain physical features, Table 5 demonstrates that the pycnocline bump can severely affect the number of IWs generated and their properties. By comparing them for each side of the front, we observed that the larger amplitude and the more energetic IWs are located on the side associated with the shallower surface layer, when $h_1 \neq h_2$. In the case of run #27, the amplitude and perturbation energy for each side of the

front are more similar with an average $\Delta A \sim 5$ m and $\Delta E_k \sim 0.1$ MJ m^{-1} as opposed to $\Delta A \sim 9$ m, $\Delta E_k \sim 1.8$ MJ m^{-1} for run #1 and $\Delta A \sim 17$ m, $\Delta E_k \sim 1.4$ MJ m^{-1} for run #33.

By increasing h_2 and decreasing h_1, the initial available potential energy in the system increases, resulting in a greater absolute front velocity (Table 5) and an higher speed of the surface layer above the ρ_1, ρ_2 interface (Figure 17 d-g). Consequently, more important instabilities and Kelvin-Helmholtz billows were formed, from 5 m tall in run #1 to 10 m in run #33, some of them developing into trapped cores reaching the surface (Figure 17c).

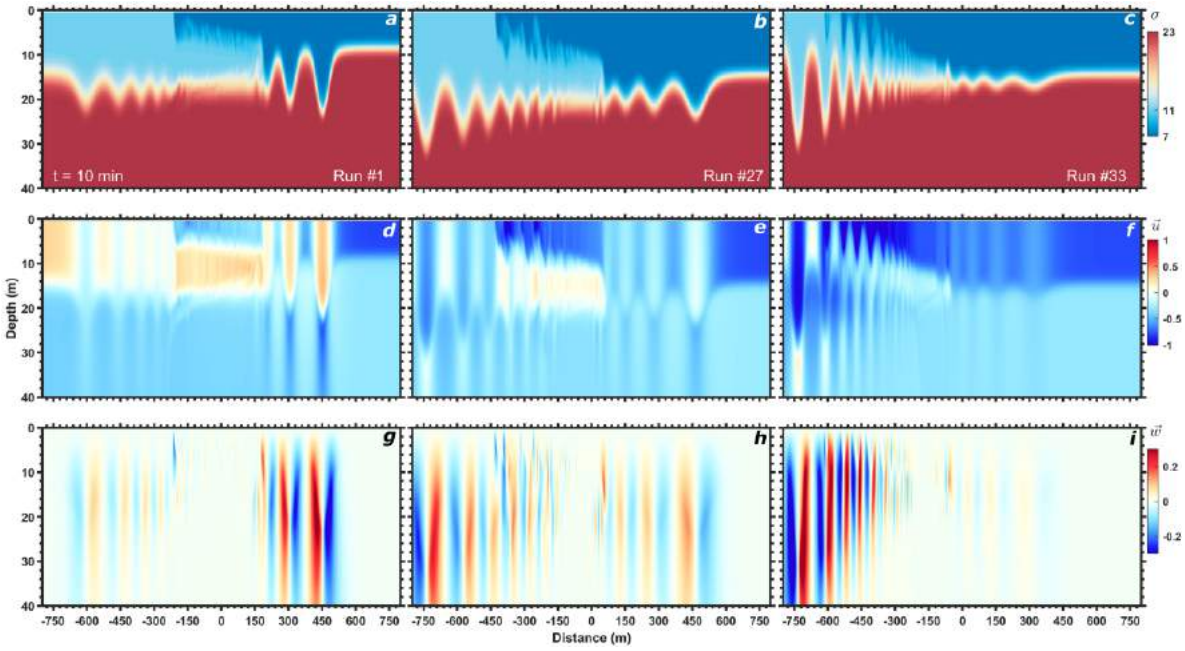

Figure 17: Snapshot of run# 1,27 and 33 at $t = 10$ min. — a-c) Density (σ), d-f) Horizontal velocity, and g-h) Vertical velocity

1.3.2.4 Stratification

To study the effect of stratification, two experiments were performed, each one was designed to study a specific component of the stratification, the thickness of the pycnocline ($2d_i$) and the difference of density $\rho_i - \rho_0$. Similar to the pycnocline bump experiments, the

first experiment explores the pycnocline thickness by designing a group of 7 nearly identical simulations where only one parameter varies within the group. These runs were initially motionless, $\rho_0, \rho_1, \rho_2 = 1023, 1020, 1007$ kg m^{-3}, $h_1, h_2 = 14$ m, $d_2 = 1.25$ m and a half pycnocline thickness d_1 varying from 0.313 to 14 m (Table 6). As a result, a single IW was detected on the left side in each run, and the front velocity remained mostly the same independently of the pycnocline thickness.

Table 6: 1^{st} subset of simulations used to characterize the stratification and the properties of the first internal wave observed on the left side of the front. (E_i units are J m^{-1} and APE units are J m^{-2}). See Table 9 for the exhaustive set of initial parameters.

run #	d_1	$2d_1/h_1$	N_1^2 (10^{-3})	APE	v_f	A_1	λ_1	c_{p1}	E (10^5)
40	0.313	0.045	46	3197.0	-0.914	12.7	69	-0.88	8.35
21	1.25	0.178	11.5	3197.1	-0.914	12.8	67	-0.88	8.33
41	3	0.429	4.8	3212.9	-0.915	12.8	65	-0.88	8.62
42	5	0.714	2.9	3251.9	-0.915	12.2	65	-0.88	7.36
43	8	1.143	1.8	3344.5	-0.915	11.1	64	-1.00	6.66
44	12	1.714	1.2	3508.7	-0.912	10.3	∅	-1.00	6.43
48	14	2.000	1.0	3605.1	-0.912	10.1	∅	-0.89	∅

Throughout this experiment, we observed a general decrease of the amplitude, the wavelength and the perturbation energy as d_1 increases, which means a smaller N_1^2 (Table 6). However some exceptions occurred, the amplitude in run #40 is smaller by roughly 0.1 m than the IWs of run #21 and 41, although the significance of the decimal may not be significant given that the highest vertical resolution is 1 m. Also, the first internal wave perturbation energy in run #41 is greater than in run #40 and 21.

The ratio of the pycnocline thickness over the depth of the surface water, $\frac{2d_1}{h_1}$, increases in each new simulation in this group, from 0.045 in run #40 to 2 in run #48. As d_1 increases over the simulations, the stratification left of the front weakens to a point, starting in run #

42, where the surface water (ρ_1) isn't separated from the bottom layer by a strong density gradient, as seen in Figure 18b. As a result, seen in run #42 to 48, there is a significant variation in the amplitude and the perturbation energy compared to the top three runs (#40, 21 and 41). For example, simulations #40, 21 and 41 have similar amplitude and energy with respective values of $\sim$ 12.8 m and $\sim 8.4 \times 10^5$ J m^{-1}, whereas the amplitude starts to decrease from run #42, $A_1 = 12.2$ m to $A_1 = 10.1$ m for run #48, the perturbation energy follows a similar trend, from 7.36 to 6.43×10^5 J m^{-1}.

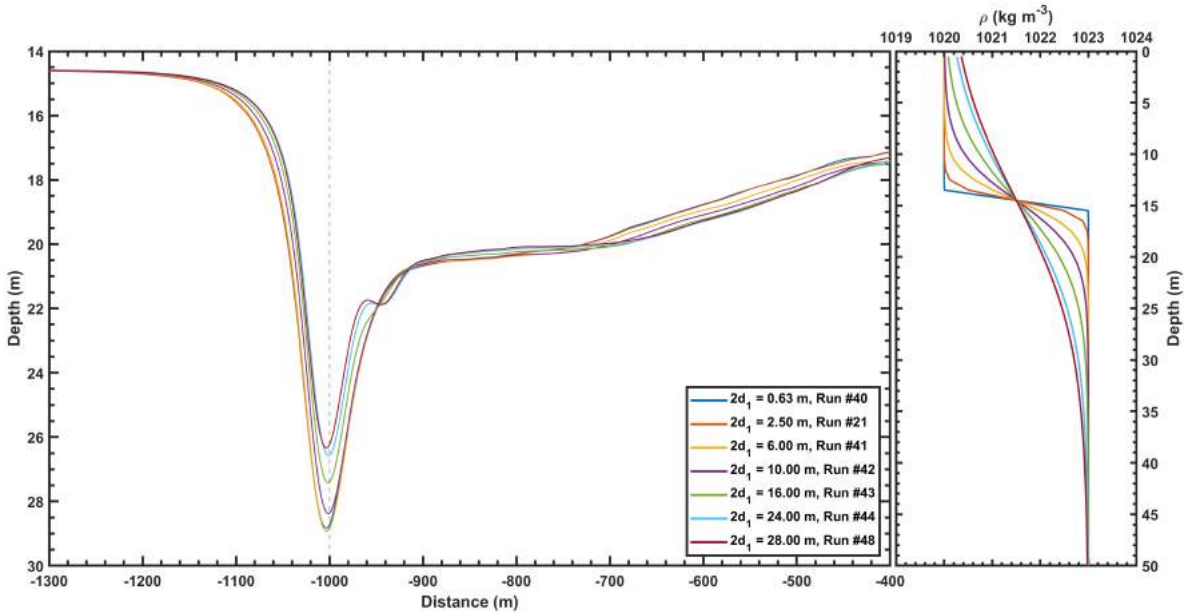

Figure 18: a) Pycnocline profile of Table 6 along the $x-$axis when the first internal waves reach x = -1000 m (grey dashed line). b) Initial density profile on the left side of the front for the simulations in Table 6.

We conclude from this experiment that a variation in the pycnocline thickness doesn't substantially affect the properties of the IWs generated by the frontally forced intrusion as long as $2d_i/h_i \lessapprox 0.5$. However, if the ratio is greater than 0.5, the amplitude, wavelength and perturbation energy will be more affected.

Following the same methodology as the previous experiment, the second set consists of simulations with nearly identical initial conditions, but instead of d_1, ρ_1 is the parameter

modifying the stratification (Table 7). For this subset, ρ_0, ρ_2 are respectively 1023 and 1007 kg m^{-3}, h_1, h_2 = 14 m and d_1, d_2 = 1.25 m, setting $2d_i/h_i$ = 0.1786. IWs were detected only on the left side of the front and run #5 and #21 had a single IW with an amplitude greater than 1 m. This explains why table 7 only reports the properties of the first IW. Instabilities appeared at the ρ_1, ρ_0 interface underneath the intrusion, and also at the ρ_1, ρ_2 interface with some Kelvin-Helmholtz billows. Trapped cores of 7m and 16m tall were detected in runs #20 and #21 respectively, above the IW trough in front of the front.

Table 7: 2^{nd} subset of simulations used to characterize the stratification and the properties of the first internal wave observed on the left side of the front. (E_1 units are J m^{-1} and APE units are J m^{-2}). See Table 9 for the exhaustive set of initial parameters.

run #	ρ_1	N_1^2	APE	v_f	A_1	λ_1	$\lvert c_{p1}\rvert$	E_1 (10^5)
5	1011	0.046	851.1	-0.39	1.9	169	1.15	0.630
19	1014	0.035	1572.5	-0.57	4.6	147	1.15	2.78
20	1017	0.023	2366.2	-0.79	9.9	133	1.00	7.836
21	1020	0.012	3197.1	-0.91	12.7	67	0.88	8.329

From table 7, we observe a clear trend in some of the IW properties as a function of the stratification. The amplitude and perturbation energy increase, respectively from 1.9 m and 0.63 J m^{-1} in run #5 to 12.7 m and 8.329 J m^{-1} in run #21. The wavelength and the absolute phase speed decrease as the buoyancy frequency decreases, respectively from 169 m and 1.15 m s^{-1} in run #5 to 67 m and 0.88 m s^{-1} in run #21 while N_1^2 goes from 0.046 to 0.012 s^{-2}.

Although only one IW was detected in run #5, we can observe in figure 19 that many waves of amplitude lower than 1 m follow the 1^{st} one on the left side of the front. This situation is caused by the first IW having an amplitude close to 1 m, which is the threshold of detection in our algorithm, and by the fact that the following waves have lower amplitudes than the previous one, $A_{1st} > A_{2nd} > A_{3rd}$. Therefore, the amplitude of the 2$^{\text{nd}}$ IW falls below the 1 m limit and is not detected. As a result, we hypothesize that the number of IWs generated decreases as the stratification weakens, which is supported by Figure 19. Waves with

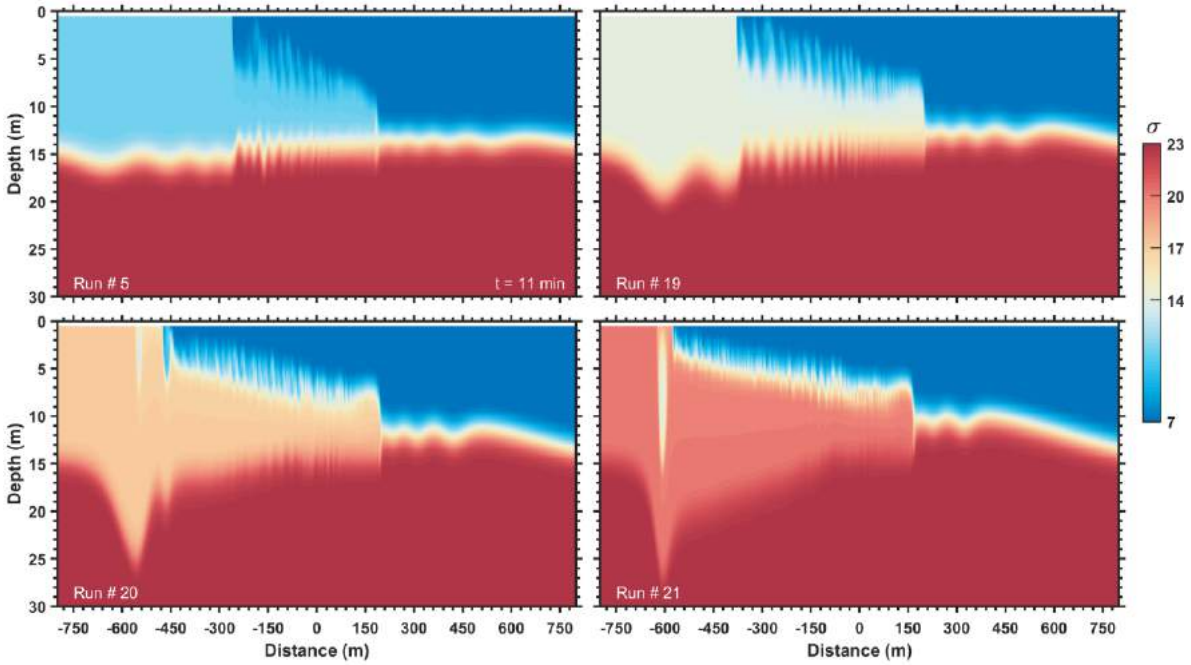

Figure 19: Snapshot at 11 minutes of the density field of simulations #5,19,20 and 21. σ units are kg m^{-3}

$A < 1$ m also propagate on the right side of the front in all the simulations of this subset.

To push this experiment further, we examine another subset of simulations that have the same initial conditions as the previous group, but this time with $h_1, h_2 = 8, 14$ m. Compared to the previous subset, the amplitude, absolute phase speed and perturbation energy are higher and the wavelength shorter in this group, as predicted by our analysis in the previous subsection. However, we find the same trend concerning the rise in amplitude and perturbation energy values as the stratification weakens (Table 8). The absolute phase velocity diminishes with a lesser stratification, but the wavelength doesn't decrease for runs # 14, #7 and #10 as it did previously.

To summarize, a variation in the pycnocline thickness doesn't substantially affect the

Table 8: 3^{rd} subset of simulations used to characterize the stratification and the properties of the first internal wave observed on the left side of the front. (E_1 units are J m^{-1} and APE units are J m^{-2}). See Table 9 for the exhaustive set of initial parameters.

run #	ρ_1	N_1^2	APE	v_f	A_1	λ_1	$\lvert c_{p1}\rvert$	E_1 (10^5)
14	1009	0.054	1057.5	-0.56	5.0	89	1.33	4.34
7	1011	0.046	1455.8	-0.66	6.4	89	1.34	5.87
10	1014	0.035	2069.6	-0.83	9.3	91	1.14	8.71
11	1017	0.023	2725.1	-0.91	12.6	68	1.00	11.6
12	1020	0.012	3401.7	-0.96	13.1	53	1.00	11.4

IW properties as long as the ratio of the pycnocline thickness over the depth of the surface layer remains smaller than 0.5. On the other hand, as the surface layer density increases, the amplitude and perturbation energy increase, and the absolute phase velocity decreases.

1.4 Discussion

1.4.1 Field Observations

From 12 days of mission split in two summer expeditions, we observed the generation of IWs via the frontally forced intrusion mechanism on 5 occasions, near the second sill of the Saguenay Fjord, mostly during ebb tide. Despite not collecting a full sequence, which consists of a front, an intrusion, some dynamic instabilities and internal waves, many *partial* observations exhibit consecutively two or more of the required features. Most of these observations lack physical properties such as the velocity field or the density profile on both sides of the front, due to instrument malfunctions. Therefore, only qualitative interpretations could be made since no controlling parameters such as the Richardson and Froude numbers, could be estimated from the sampling.

To this day, the origin of the fronts and the interactions between the different water

masses at the surface are not understood. It becomes essential to fully capture at least one complete sequence from field observations if we desire to further the understanding of this mechanism. A satisfying sequence must contain the entire velocity field, the temperature and salinity profiles on both sides of the front and during the intrusion, an echogram and a series of georectified images.

In that mind set, an experiment using two research boats can optimized the sampling. As the first boat samples the front and the IWs along their propagation with an ADCP, echosounder and small CTD, the second one stays stationary as it collects multiple density profiles on both sides of the front (yo-yo technique) while the IWs and intrusion crossed its path. Two high resolution cameras could be used to cover a wider range of the fjord since we have identified to date at least two sites of generation. Also, man controlled drones can provide to the on board team a better view of the surface patterns, therefore increasing the chance of capturing more features that could be difficult to detect from the boat. As mechanical failure, bad weather and equipment malfunctions can cost several days of sampling, as it did in the last two expeditions, the next mission should last more than 7 days to reduce the impact of these misfortunes.

1.4.2 Numerical simulations

From exploring a wide range of values for some specific parameters such as the surface layer thickness, the pycnocline thickness and the surface layer density, we concluded that most of our simulations can be categorized in two typical cases depending on how the pressure gradient is initially oriented below the front, and also that the initial available potential energy in the system plays an important role in the front velocity. We learned that a pycnocline bump in a sharply stratified environment can alone trigger the generation of IWs, and the height of the bump modulates the amplitude of these features. Another key aspect of this research was the interest toward the impact of the stratification on the IWs properties, in that regards, the thickness of the pycnocline barely impacts those properties as long as the

thickness is lower than half of the surface layer thickness. On the other hand, a change in the surface layer density modifies the number of internal waves generated, as well as their amplitude, perturbation energy and wavelength.

Additional simulations exploring different environmental conditions and the use of a three dimensional model at high spatial resolution are required to further the understanding of this mechanism, since the velocity field hasn't been explored in this study and the collisions where the surface velocities vary along the front are impossible to simulate with the current model. The latter could explain why we haven't observed internal waves on both sides of the front during the field expeditions. During the 2019 winter campaign, IWs were emitted from a front located near a 2 km wide vortex downstream of Anse-de-Roche. A 3-D model could enlighten the interaction between the front, IWs and the vortex.

1.4.3 Perspectives

To conclude, for any evidence collected during the two summer expeditions, the stratification of the water masses and the velocity field on both side of the front were impossible to determine due to a series of misfortune. In consequence, the results made with the numerical model were not verified experimentally. Due to the nature of our results, which are specific variations of the waves properties in a well understood environment, the validation process required a full sequence of at least two evidences of internal waves. To this date, only one was captured (Bourgault et al., 2016).

To solve this problem, a future study can focus on collecting with the setup described in the fields observations section, evidences of internal waves generated by frontally forced intrusion. Similarly to the method used here, the properties of the observed waves will be compared between them in regards to the environmental conditions such as the stratification and surface layer thicknesses. This validation process will confirmed or refuted the hypothesis presented here and fill a missing part of this study, a link between the observations and the numerical results.

CONCLUSION GÉNÉRALE

Ce manuscrit décrit la recherche menée dans le but d'éclairer un sujet récemment découvert et peu étudié jusqu'à présent. Il explique notamment les pistes envisagées et les résultats qui en ressortent tout en montrant les limitations de l'étude et la complexité de la génération d'ondes internes par collision frontale.

Deux missions océanographiques, orientées vers ce mécanisme de formation, ont permis de récolter quelques évidences dans le fjord du Saguenay. Même si ces observations ne contiennent pas de séquence complète (front, intrusion, instabilités dynamiques et ondes internes), elles démontrent tout de même que la séquence échantillonnée par Bourgault et al. (2016) n'est pas si fortuite, et donc que ce mécanisme se produire assez fréquemment. De plus, l'image acoustique recueille le 7 juillet 2017 montrant le début de l'intrusion sous le front vient soutenir expérimentalement l'hypothèse émise par Bourgault et al. (2016), qui est que l'intrusion provient de la collision de deux masses d'eaux de densité différentes.

Par la suite, plus de 70 simulations numériques idéalisées ont été réalisées dans le but de comprendre globalement ce processus de génération, de déterminer les propriétés des ondes internes générées en variant certains paramètres initiaux ou de reproduire ce phénomène en utilisant des données de terrain recueillies par d'autres équipes de chercheurs. Ces modélisations ont démontré que dans l'espace des paramètres utilisés, la largeur du front n'altère pas les propriétés physiques des ondes internes et que la vitesse du front dépend majoritairement de l'énergie potentielle disponible initialement. De plus, un saut de la pycnocline causé par une différence d'épaisseur des eaux de surface peut générer des ondes internes. L'étude de la stratification a démontré que l'amplitude, le nombre d'ondes et l'énergie de perturbations étaient plus sensibles à une modification de la stratification par une variation de la densité des couches de surfaces que par une variation de l'épaisseur de la pycnocline, dans la mesure où celle-ci est au minimum deux fois plus petite que l'épaisseur de la couche de surface.

Malgré une série de concluantes observations de terrain, plusieurs obstacles, majoritairement hors de notre contrôle, ont contraint cette recherche à réduire la quantité de données recueillies. Pour la mission 2017, le cable alimentant le courantomètre ne se connectait pas correctement, de ce fait, le champ de vitesse manque pour plusieurs observations pertinentes, empêchant l'étude complète de la dynamique de l'intrusion. En plus d'un problème de moteur et d'une journée très venteuse, ce qui a considérablement réduit le temps en mer, la perte de la sonde de température et de salinité, à l'été 2018, a contraint l'équipe de recherche à interpréter que qualitativement la séquence du 9 juillet 2018.

Afin de remédier à ces incovénients, la prochaine mission pourrait intégrer un deuxième petit navire de recherche qui ferait du *yo-yo* avec une sonde CTD en avant de l'intrusion, ce qui nous permettrait d'échantilloner le profil des ondes internes, de l'intrusion et des côtés du front pendant que le premier navire collecterait les données de courants et le profil acoustique. De plus, l'utilisation d'une deuxième caméra à haute résolution donnerait une couverture plus étendue de la surface de l'eau entre la baie d'Anse-de Roche et le 2^e seuil. Un drône piloté depuis un des navires aiderait grandement à identifer les patrons de surface hors du champs de vision de l'observateur et augmenterait la précision de l'échantillonage. De plus, en planifiant une mission d'une plus grande durée, les intempéries et bris mécaniques, s'ils sont réparables, auraient un impact plus limité sur la probabilité d'observer la génération d'ondes internes par collision frontale.

En ce qui à trait à la modélisation, le temps fut le principal facteur limitant, malgré l'important nombre de simulations, il reste plusieurs paramètres à explorer. Notamment le champ de vitesse et les interactions de celui-ci avec le saut de la pycnocline et la stratification. De plus, l'étude des collisions frontales imparfaites pourrait expliquer pourquoi on observe, en mer, la propagation d'ondes internes uniquement d'un côté du front. L'utilisation d'un modèle 3D à haute résolution spatiale permettrait d'étudier l'interaction de ce mécanisme avec d'autres phénomènes physiques tridimensionnels comme les tourbillons. À l'hiver 2019, des ondes internes émanant d'un front localisé en périphérie d'un tourbillon

d'environ 2 km de diamètre nous amène à penser qu'il y aurait peut-être un lien entre celui-ci et la génération d'ondes internes.

En terminant ...

Au retour de leur expédition en Arctique, Fridtjof Nansen et son équipage racontèrent en 5 volumes, le récit de leur voyage, les techniques de survie développées ainsi que leur multiple découvertes scientifiques. Ils pavèrent ainsi la voie à de nombreux explorateurs et océanographes, notamment Otto Sverdrup, Oscar Wisting et Roald Amundsen. Ces derniers désirant naviguer dans les sillions de l'exploration polaire ouverts par Nansen, ils appliquèrent les leçons apprises par ce dernier et poussèrent leur expéditions jusqu'au pôle nord, et même au pôle sud dans le cas de Wisting et d'Amundsen.

De nos jours, l'influence de ces explorateurs se fait encore ressentir alors que la mission MOSAiC (Multidisciplinary drifting Observatory for the Study of Arctic Climate) du Polarstern, un brise-glace de recherche allemand, touche à sa fin. À l'image de Nansen à bord du Fram, le Polarstern s'est laissé dériver sur la banquise arctique durant un an complet, récoltant de nombreuses données océanographiques et météorologiques qui seront analysées dans les prochaines années par une multitude de scientifiques à travers le monde.

En terminant, il est difficile de déterminer qu'elle sera dans le futur, l'impact scientifique, social et culturel d'une recherche. Tombera-t-elle dans l'oubli, appuyera- t-elle une hypothèse, ou donnera-t-elle naissance à un nouveau champ d'étude ? C'est donc sans prétention, et avec plein d'espoir, que je mets fin à cette recherche en souhaitant qu'un nouveau chapitre de l'exploration de ce mécanisme puisse commencer.

ANNEXE I

TABLEAU DES CONDITIONS INITIALES DES SIMULATIONS IDÉALISÉES

Tableau 9: Conditions intitiales pour chaque simulation, Format des unités [mks] .

#	ρ_0	ρ_1	ρ_2	u_{01}	u_{02}	u_1	u_2	h_1	h_2	d_1	d_2	L	Ri_1	Ri_2	Fr_1	Fr_2
1	1023	1011	1007	-0.4	-0.31	0.3	-0.8	14	8	2.5	1.25	20	1.17	1.59	0.26	0.73
2	1023	1011	1007	0	0	0	0	14	8	2.5	1.25	20	Inf	Inf	0	0
3	1023	1013.8571	1007	0	0	0	0	14	8	2.5	1.25	20	Inf	Inf	0	0
4	1023	1013.8571	1007	-0.4	-0.32	0.2	-0.8	14	8	2.5	1.25	20	1.22	1.66	0.21	0.73
5	1023	1011	1007	0	0	0	0	14	14	1.25	1.25	20	Inf	Inf	0	0
6	1023	1007	1007	0	0	0	0	14	8	1.25	1.25	20	Inf	Inf	0	0
7	1023	1011	1007	0	0	0	0	8	14	1.25	1.25	20	Inf	Inf	0	0
8	1023	1011	1011	0	0	0	0	14	8	1.25	1.25	20	Inf	Inf	0	0
9	1023	1011	1007	0	0	0	0	8	20	1.25	1.25	20	Inf	Inf	0	0
10	1023	1014	1007	0	0	0	0	8	14	1.25	1.25	20	Inf	Inf	0	0
11	1023	1017	1007	0	0	0	0	8	14	1.25	1.25	20	Inf	Inf	0	0
12	1023	1020	1007	0	0	0	0	8	14	1.25	1.25	20	Inf	Inf	0	0
13	1023	1019	1007	0	0	0	0	8	16	1.25	1.25	20	Inf	Inf	0	0
14	1023	1009	1007	0	0	0	0	8	14	1.25	1.25	20	Inf	Inf	0	0
15	1023	1019	1007	0	0	0	0	8	20	1.25	1.25	20	Inf	Inf	0	0
16	1023	1011	1007	-0.4	-0.31	0.3	-0.8	14	8	2.5	1.25	40	1.17	1.59	0.26	0.73
17	1023	1019	1007	0	0	0	0	20	14	1.25	1.25	20	Inf	Inf	0	0

#	ρ_0	ρ_1	ρ_2	u_{01}	u_{02}	u_1	u_2	h_1	h_2	d_1	d_2	L	Ri_1	Ri_2	Fr_1	Fr_2
18	1023	1019	1007	0	0	0	0	14	20	1.25	1.25	20	Inf	Inf	0	0
19	1023	1014	1007	0	0	0	0	14	14	1.25	1.25	20	Inf	Inf	0	0
20	1023	1017	1007	0	0	0	0	14	14	1.25	1.25	20	Inf	Inf	0	0
21	1023	1020	1007	0	0	0	0	14	14	1.25	1.25	20	Inf	Inf	0	0
22	1023	1011	1007	-0.4	-0.29	0.3	-0.8	14	14	1.25	1.25	20	0.59	1.46	0.26	0.55
23	1023	1011	1007	-0.67	-0.54	0.87	-0.3	14	8	2.5	1.25	20	0.24	6.69	0.71	0.29
24	1023	1011	1007	-0.67	-0.55	0.87	-0.3	14	14	2.5	2.5	20	0.24	12.27	0.71	0.24
25	1023	1011	1007	0.85	0.92	0.95	-0.3	8	8	2.5	2.5	20	57.54	0.52	1.01	0.33
26	1023	1011	1007	0.9	0.99	1.2	-0.3	12	8	2.5	2.5	20	6.39	0.46	1.05	0.34
27	1023	1011	1007	-0.4	-0.29	0.3	-0.8	14	14	2.5	1.25	20	1.17	1.46	0.26	0.55
28	1023	1007	1007	-0.07	0.07	0.7	-0.7	14	14	1.25	1.25	20	0.64	0.64	0.48	0.48
29	1023	1011	1011	-0.07	0.07	0.7	-0.7	14	14	1.25	1.25	20	0.48	0.48	0.55	0.55
30	1023	1011	1007	-0.4	-0.19	1	-1	14	14	2.5	2.5	20	0.29	1.18	0.79	0.68
31	1023	1011	1007	-0.4	0.01	2	-2	14	14	2.5	2.5	20	0.1	0.19	1.58	1.36
32	1023	1011	1007	-0.4	-0.31	0.3	-0.8	14	8	2.5	1.25	80	1.17	1.59	0.26	0.73
33	1023	1011	1007	-0.4	-0.32	0.3	-0.8	8	14	2.5	1.25	20	1.17	1.65	0.33	0.55
34	1023	1011	1007	-0.4	-0.29	0.8	-0.3	14	8	2.5	1.25	20	0.4	2557.94	0.64	0.28
35	1023	1011	1007	0.4	0.48	0.8	-0.3	14	8	2.5	1.25	20	3.6	0.63	0.64	0.29
36	1023	1011	1007	-0.4	-0.34	0.8	-0.3	8	14	2.5	1.25	20	0.4	240.6	0.84	0.22

#	ρ_0	ρ_1	ρ_2	u_{01}	u_{02}	u_1	u_2	h_1	h_2	d_1	d_2	L	Ri_1	Ri_2	Fr_1	Fr_2
37	1023	1011	1007	0.4	0.5	0.8	-0.3	8	14	2.5	1.25	20	3.6	0.61	0.84	0.23
38	1023	1014	1007	0	0	0	0	14	14	0.94	1.25	20	Inf	Inf	0	0
39	1023	1017	1007	0	0	0	0	14	14	0.63	1.25	20	Inf	Inf	0	0
40	1023	1020	1007	0	0	0	0	14	14	0.31	1.25	20	Inf	Inf	0	0
41	1023	1020	1007	0	0	0	0	14	14	3	1.25	20	Inf	Inf	0	0
42	1023	1020	1007	0	0	0	0	14	14	5	1.25	20	Inf	Inf	0	0
43	1023	1020	1007	0	0	0	0	14	14	8	1.25	20	Inf	Inf	0	0
44	1023	1020	1007	0	0	0	0	14	14	12	1.25	20	Inf	Inf	0	0
45	1023	1020	1007	-0.4	-0.31	0.3	-0.8	14	8	2.5	1.25	20	0.29	1.59	0.51	0.73
46	1023	1020	1016	-0.4	-0.31	0.3	-0.8	14	8	2.5	1.25	20	0.29	0.7	0.51	1.1
47	1023	1020	1016	-0.4	-0.31	0.3	-0.8	14	8	0.63	0.55	20	0.07	0.31	0.51	1.1
48	1023	1020	1007	0	0	0	0	14	14	14	1.25	20	Inf	Inf	0	0
49	1023	1014	1007	0	0	0	0	14	8	1.25	1.25	20	Inf	Inf	0	0
50	1023	1017	1007	0	0	0	0	14	8	1.25	1.25	20	Inf	Inf	0	0
51	1023	1020	1007	0	0	0	0	14	8	1.25	1.25	20	Inf	Inf	0	0
52	1023	1009	1007	0	0	0	0	14	8	1.25	1.25	20	Inf	Inf	0	0
100	1023	1011	1007	0.4	0.31	-0.3	0.8	14	8	2.5	1.25	20	1.17	1.59	0.26	0.73

ANNEXE II

ATLAS DES ONDES INTERNES OBSERVÉES DURANT LES MISSIONS SILLEX

Cette annexe contient les images acoustiques des ondes solitaires et des trains d'ondes internes échantillonés dans le fjord du Saguenay lors des missions Sillex 2017 et 2018. Les échogrammes sont affichés en order chronologique de la date d'échantillonage.

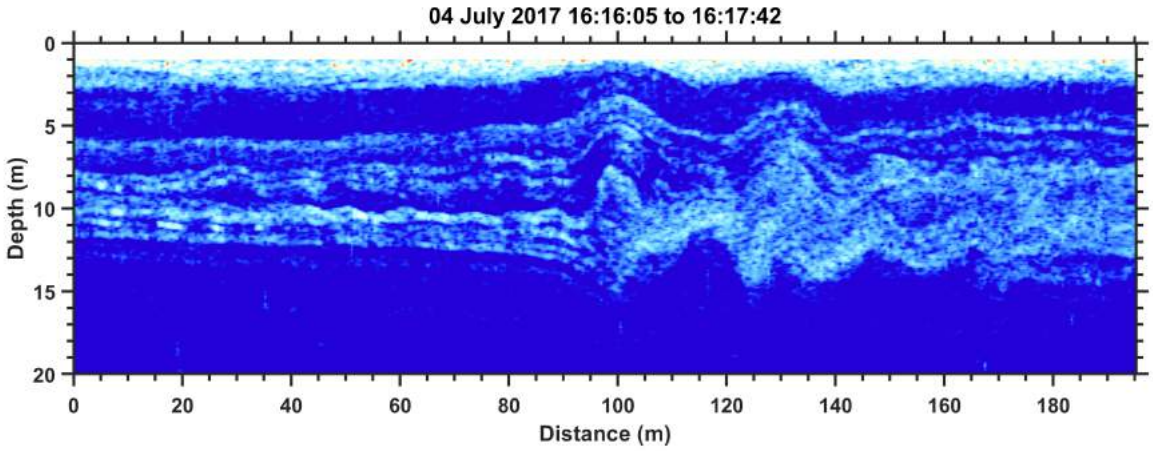

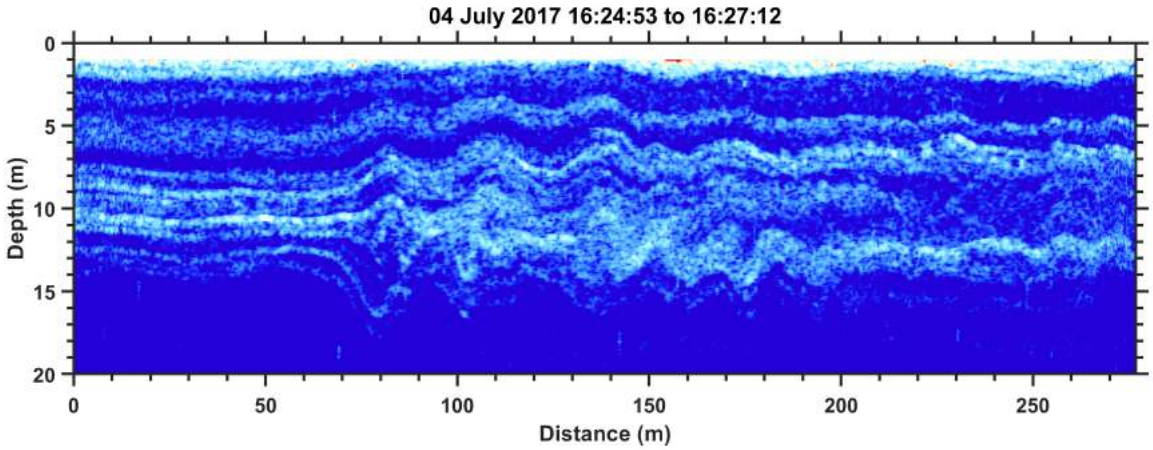
04 July 2017 16:24:53 to 16:27:12
Depth (m)
0
5
10
15
20
0
50
100
150
200
250
Distance (m)

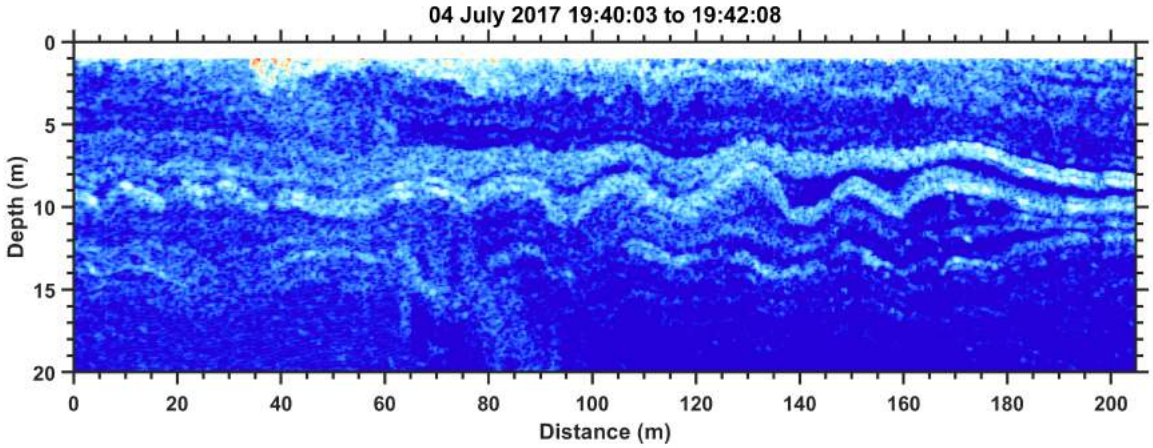
04 July 2017 19:40:03 to 19:42:08
Depth (m)
0
5
10
15
20
0
20
40
60
80
100
120
140
160
180
200
Distance (m)

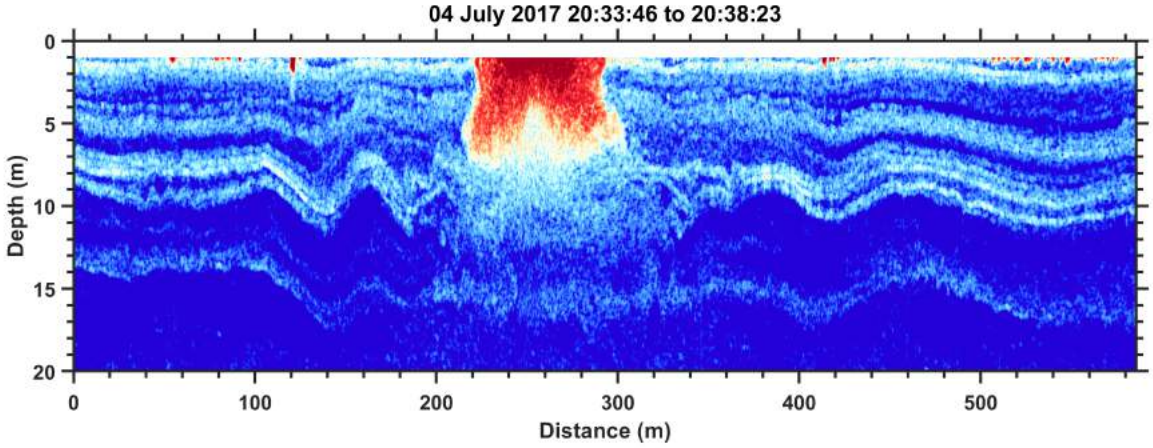
04 July 2017 20:33:46 to 20:38:23
Depth (m)
0
5
10
15
20
0
100
200
300
400
500
Distance (m)

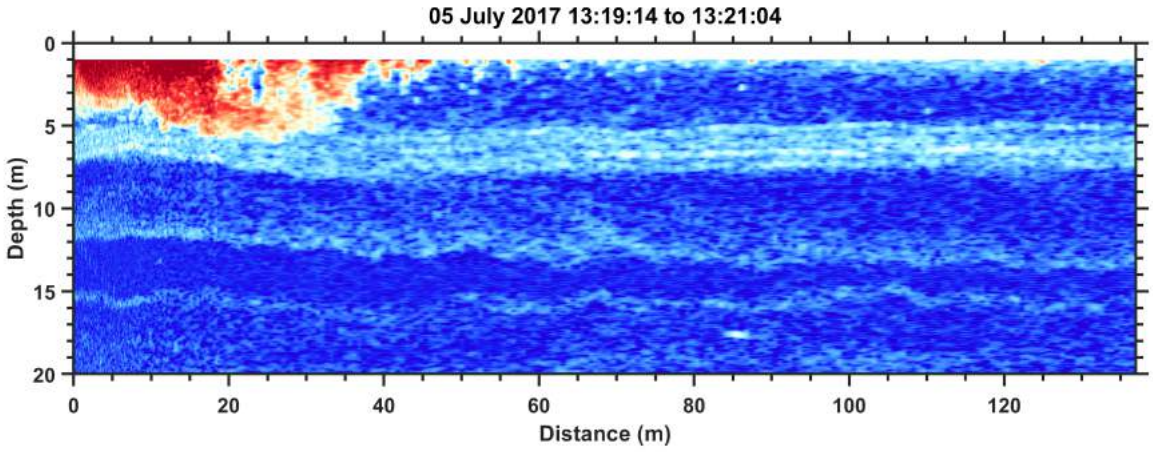
05 July 2017 13:19:14 to 13:21:04
Depth (m)
0
5
10
15
20
0
20
40
60
80
100
120
Distance (m)

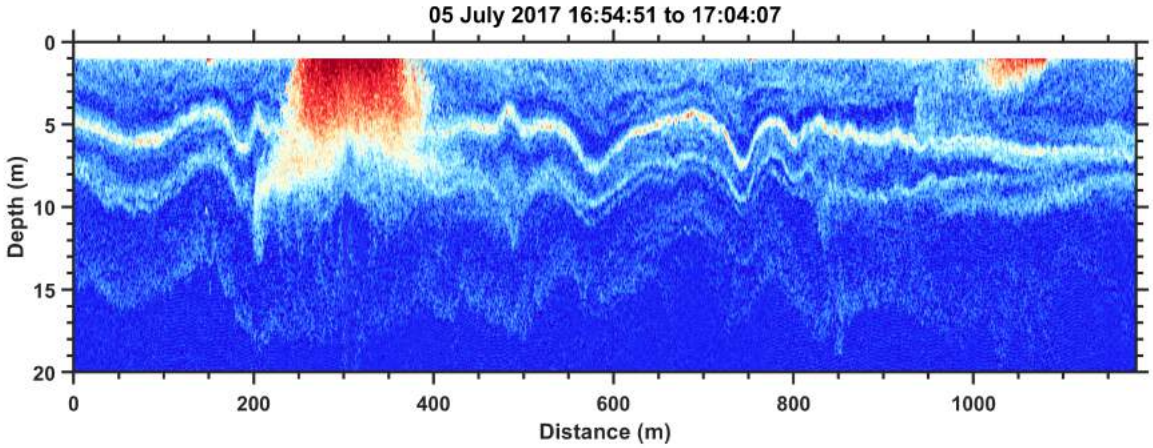
05 July 2017 16:54:51 to 17:04:07
Depth (m)
0
5
10
15
20
0
200
400
600
800
1000
Distance (m)

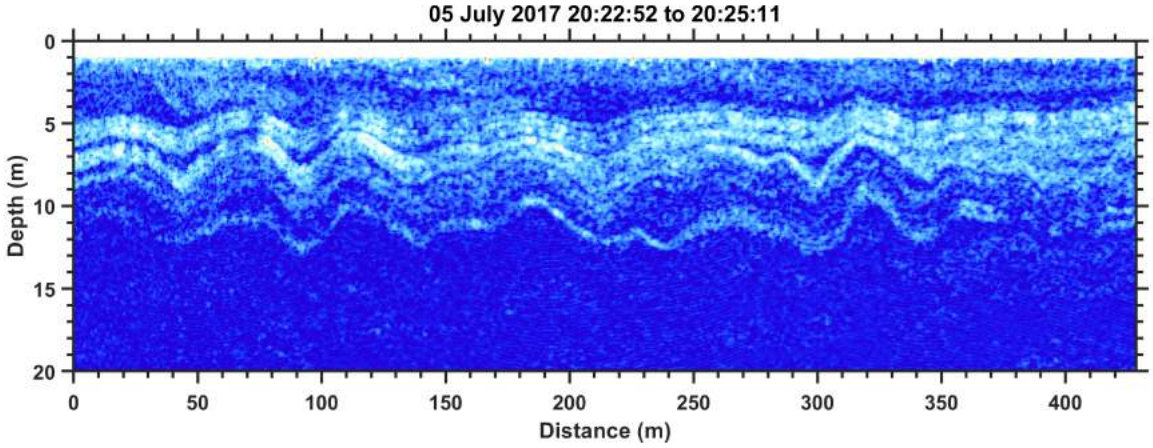
05 July 2017 20:22:52 to 20:25:11
Depth (m)
0
5
10
15
20
0
50
100
150
200
250
300
350
400
Distance (m)

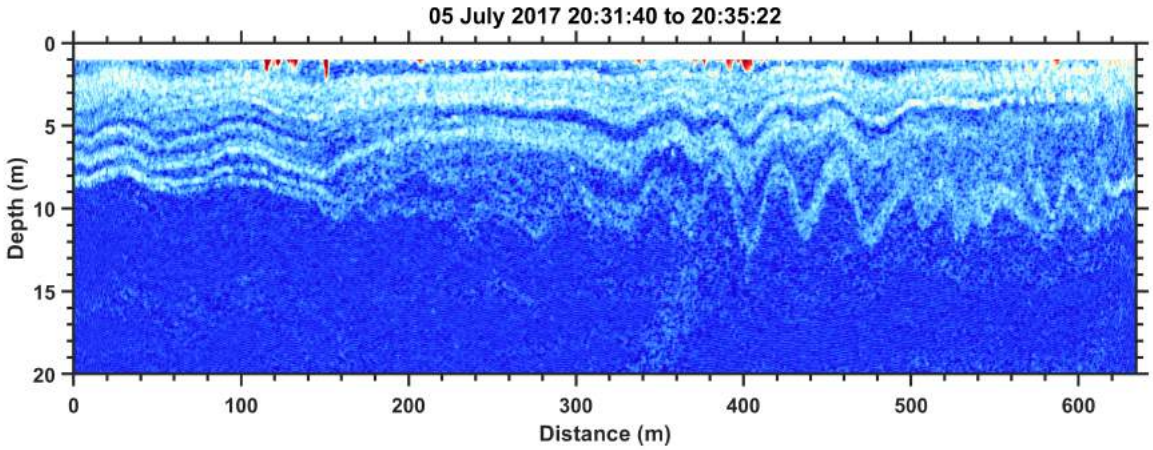
05 July 2017 20:31:40 to 20:35:22
Depth (m)
0
5
10
15
20
0
100
200
300
400
500
600
Distance (m)

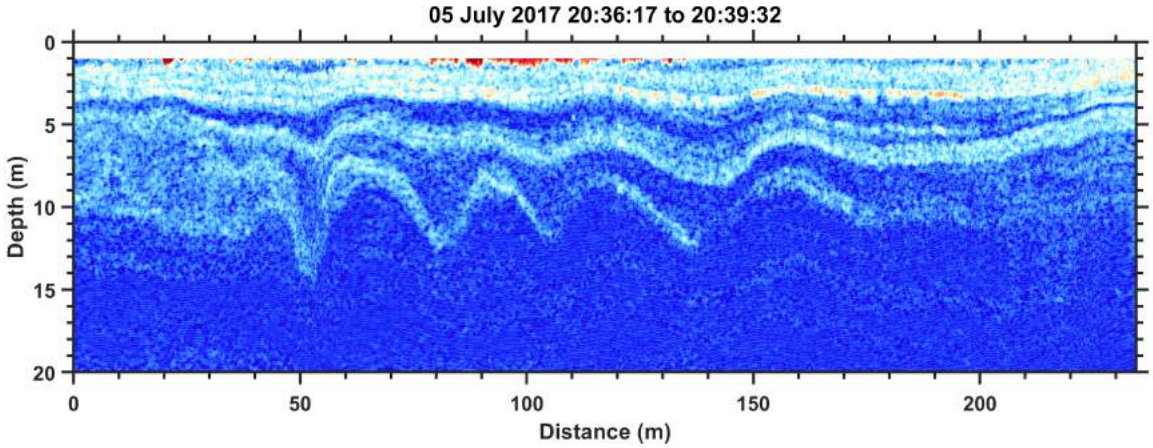
05 July 2017 20:36:17 to 20:39:32
Depth (m)
0
5
10
15
20
0
50
100
150
200
Distance (m)

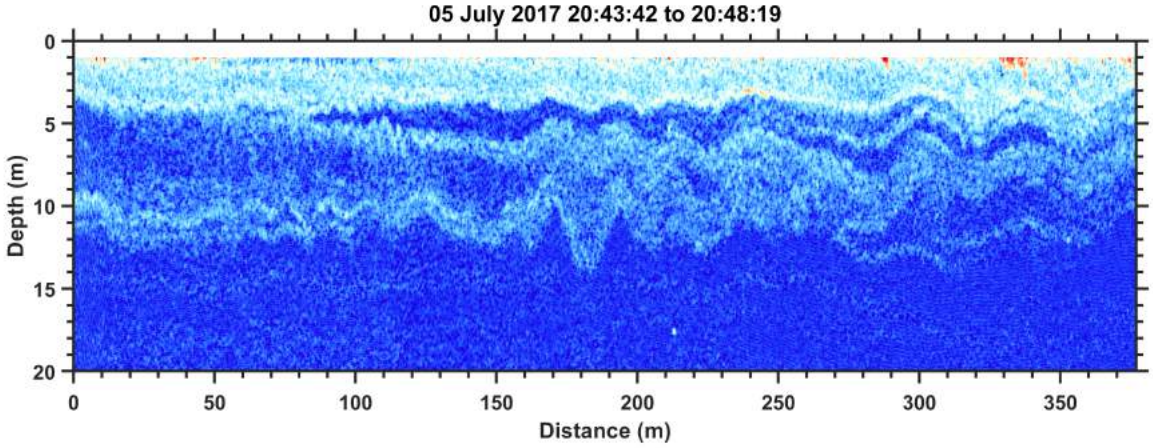
05 July 2017 20:43:42 to 20:48:19
Depth (m)
0
5
10
15
20
0
50
100
150
200
250
300
350
Distance (m)

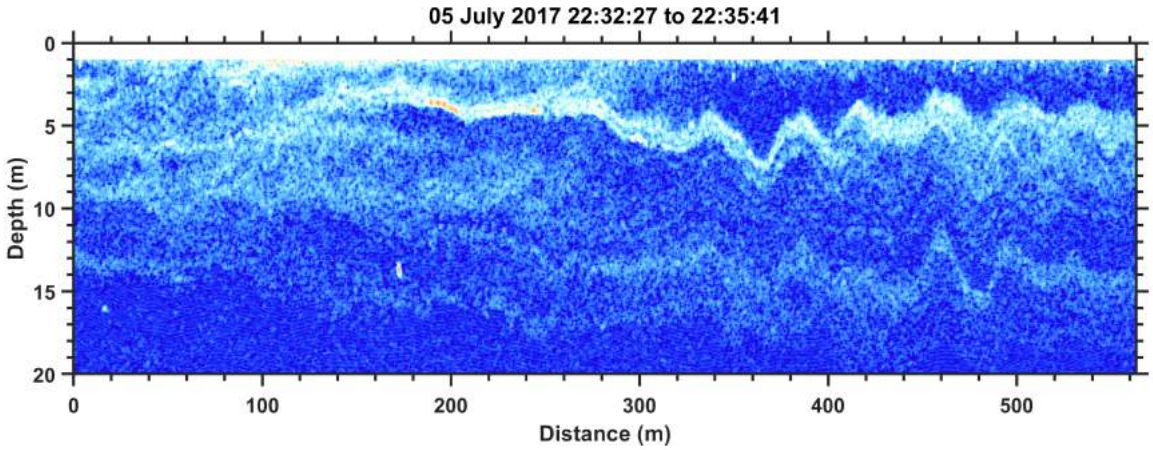
05 July 2017 22:32:27 to 22:35:41
Depth (m)
0
5
10
15
20
0
100
200
300
400
500
Distance (m)

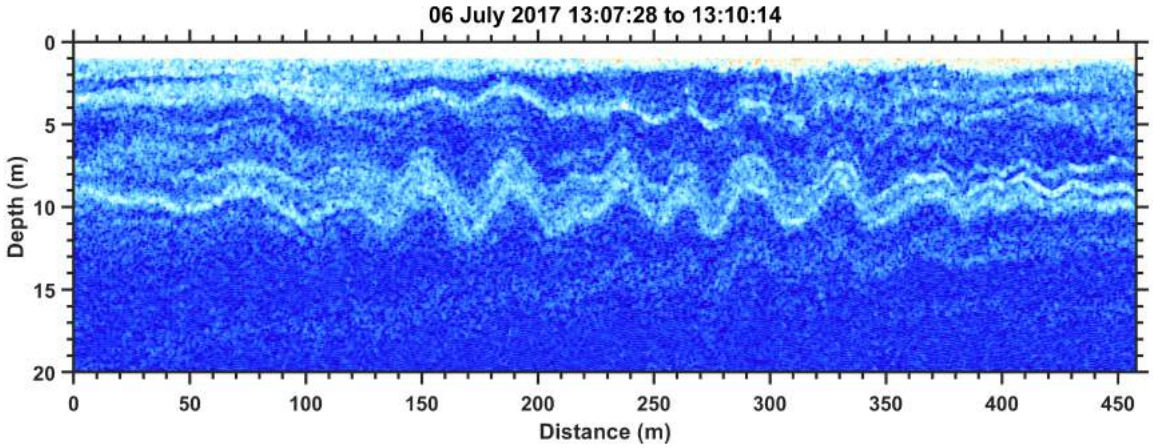
06 July 2017 13:07:28 to 13:10:14
Depth (m)
0
5
10
15
20
0
50
100
150
200
250
300
350
400
450
Distance (m)

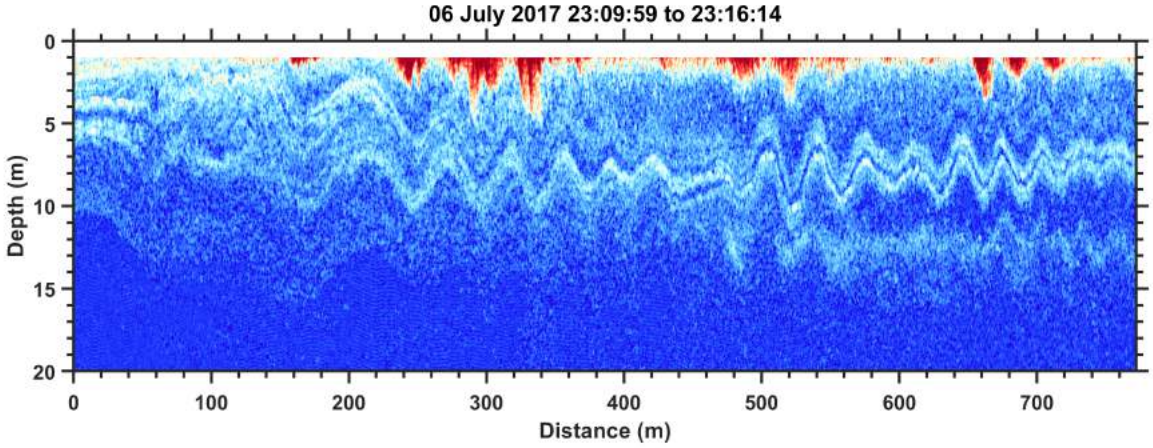
06 July 2017 23:09:59 to 23:16:14
Depth (m)
0
5
10
15
20
0
100
200
300
400
500
600
700
Distance (m)

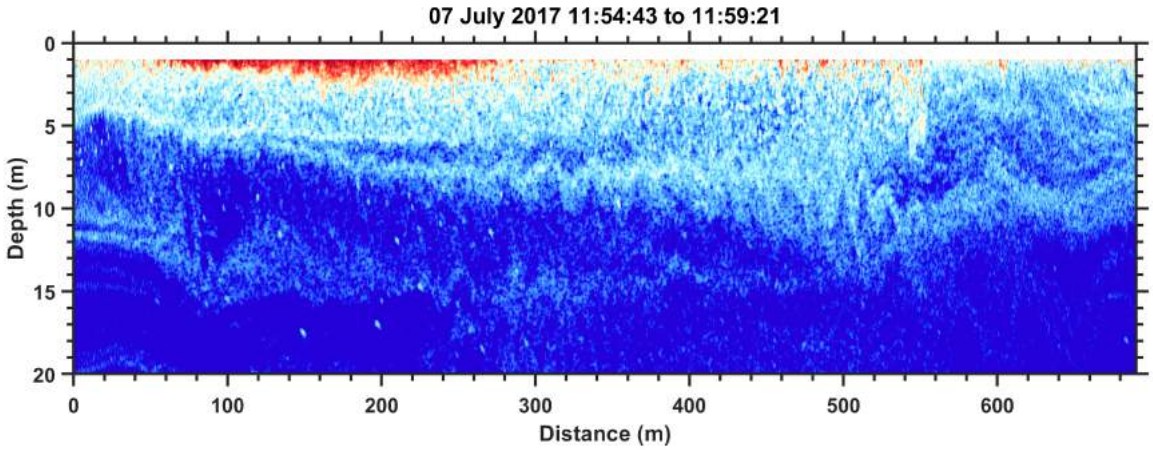
07 July 2017 11:54:43 to 11:59:21
Depth (m)
0
5
10
15
20
0
100
200
300
400
500
600
Distance (m)

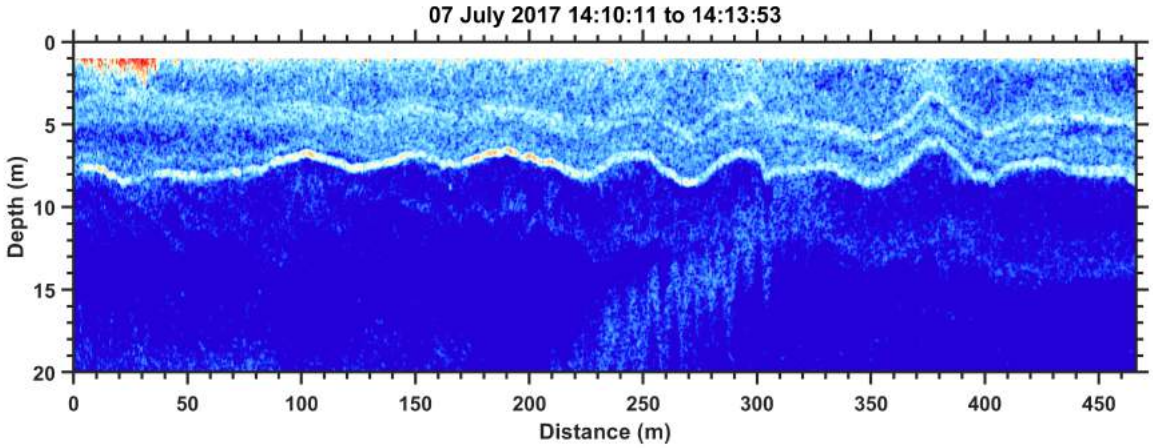
07 July 2017 14:10:11 to 14:13:53
Depth (m)
0
5
10
15
20
0
50
100
150
200
250
300
350
400
450
Distance (m)

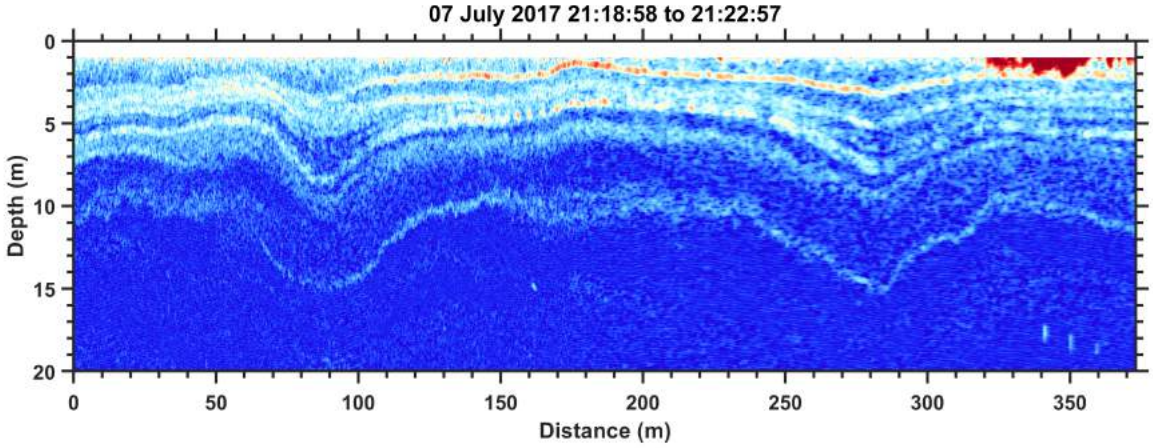
07 July 2017 21:18:58 to 21:22:57
Depth (m)
0
5
10
15
20
0
50
100
150
200
250
300
350
Distance (m)

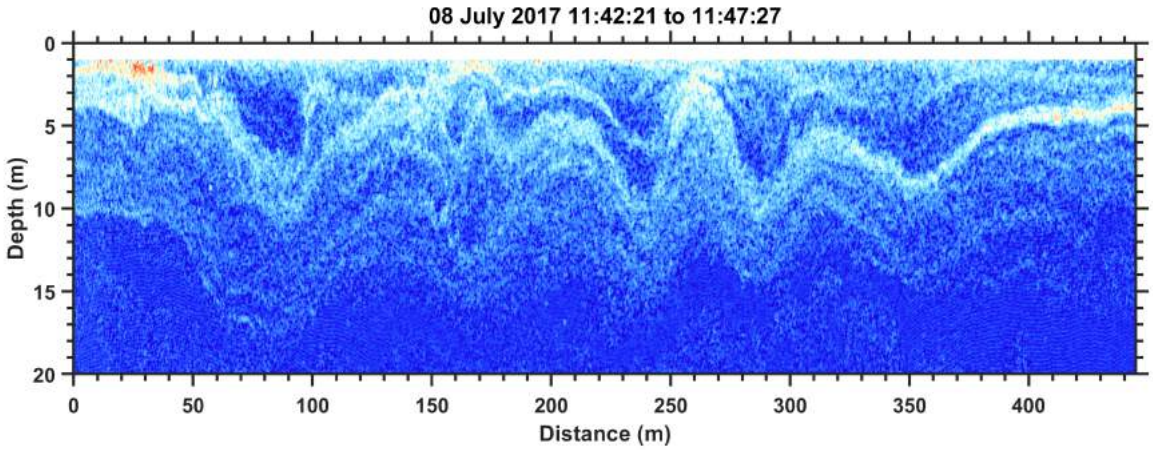
08 July 2017 11:42:21 to 11:47:27
Depth (m)
0
5
10
15
20
0
50
100
150
200
250
300
350
400
Distance (m)

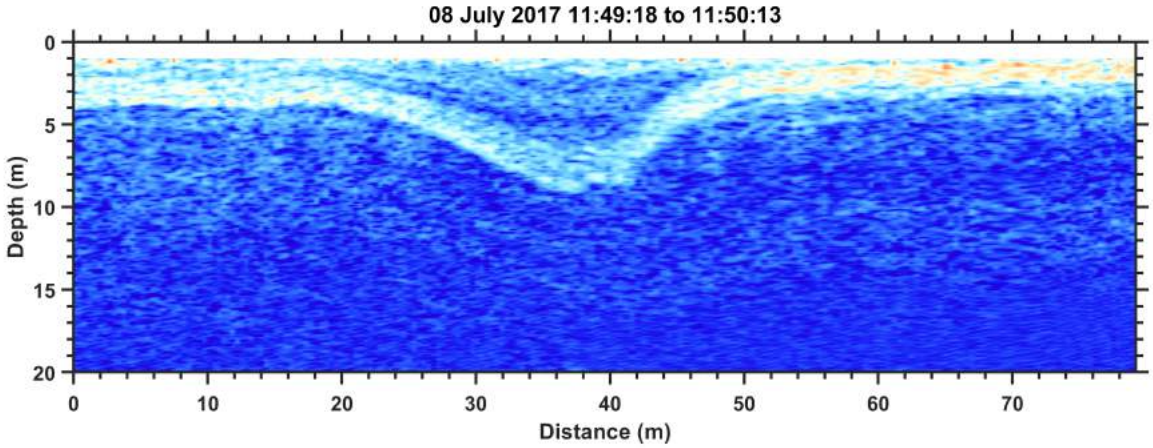
08 July 2017 11:49:18 to 11:50:13
Depth (m)
0
5
10
15
20
0
10
20
30
40
50
60
70
Distance (m)

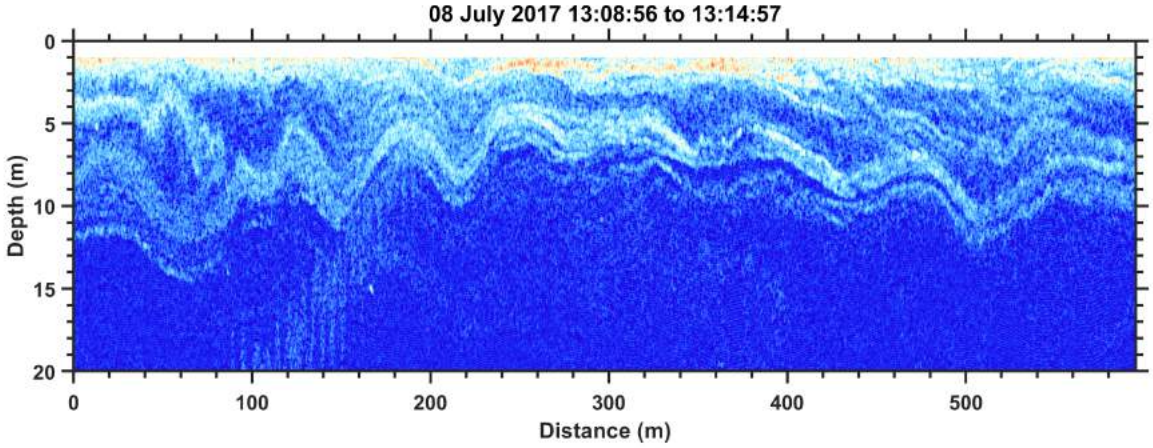
08 July 2017 13:08:56 to 13:14:57
Depth (m)
0
5
10
15
20
0
100
200
300
400
500
Distance (m)

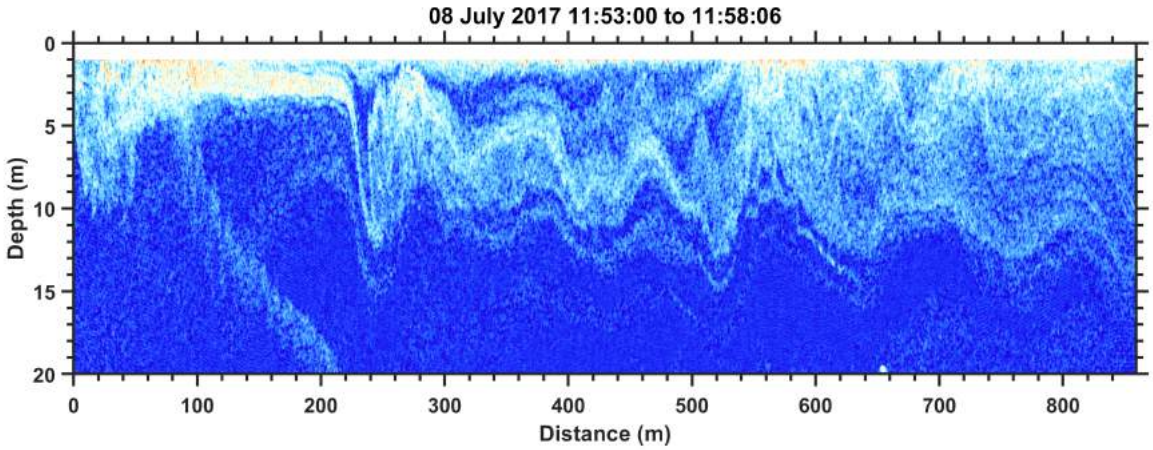
08 July 2017 11:53:00 to 11:58:06
Depth (m)
0
5
10
15
20
0
100
200
300
400
500
600
700
800
Distance (m)

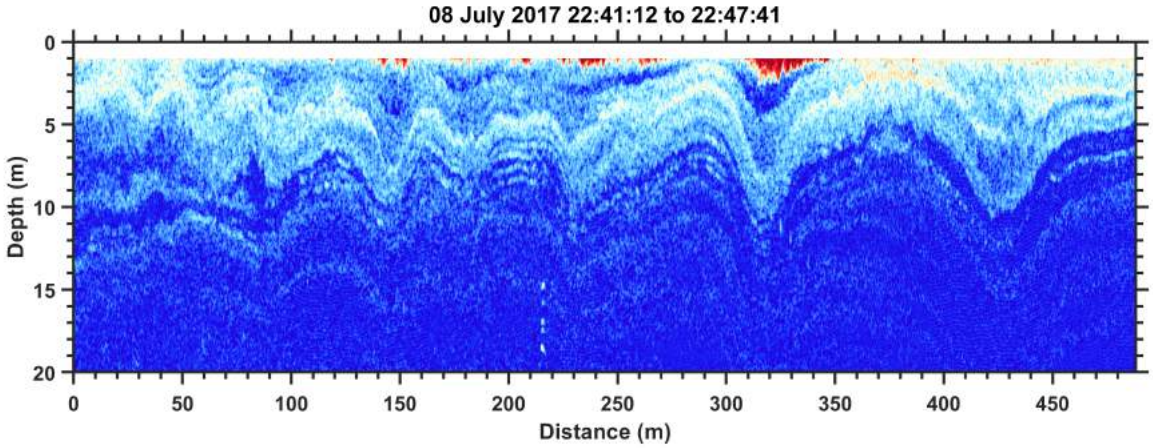
08 July 2017 22:41:12 to 22:47:41
Depth (m)
0
5
10
15
20
0
50
100
150
200
250
300
350
400
450
Distance (m)

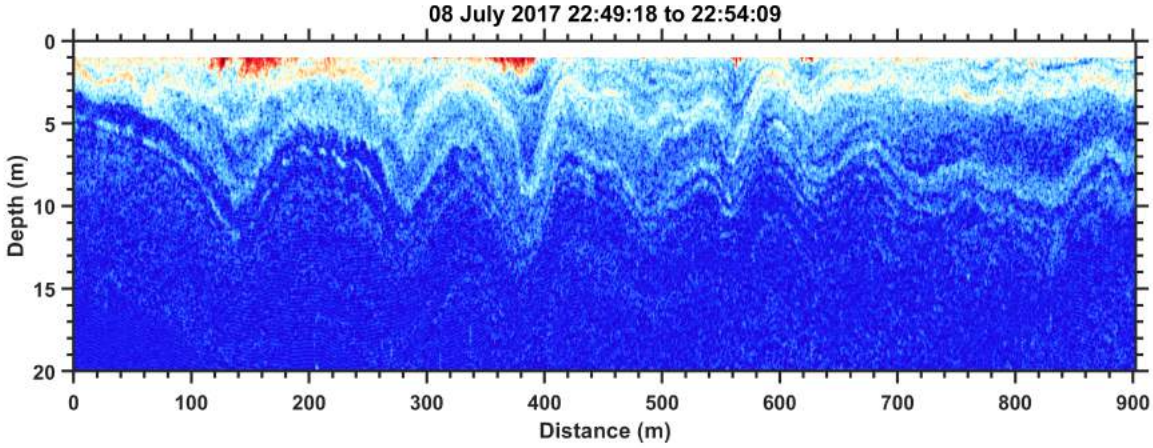
08 July 2017 22:49:18 to 22:54:09
Depth (m)
0
5
10
15
20
0
100
200
300
400
500
600
700
800
900
Distance (m)

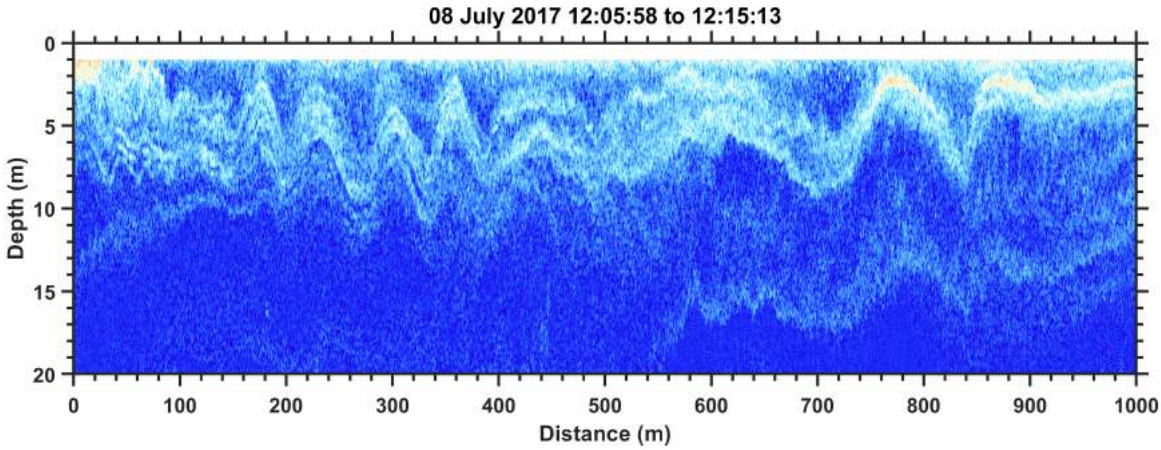
08 July 2017 12:05:58 to 12:15:13
Depth (m)
0
5
10
15
20
0
100
200
300
400
500
600
700
800
900
1000
Distance (m)

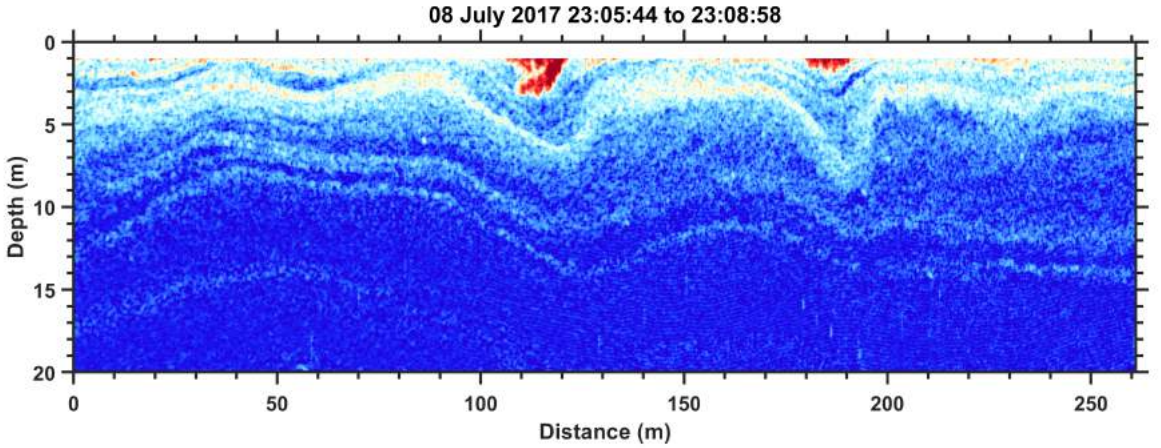
08 July 2017 23:05:44 to 23:08:58
Depth (m)
0
5
10
15
20
0
50
100
150
200
250
Distance (m)

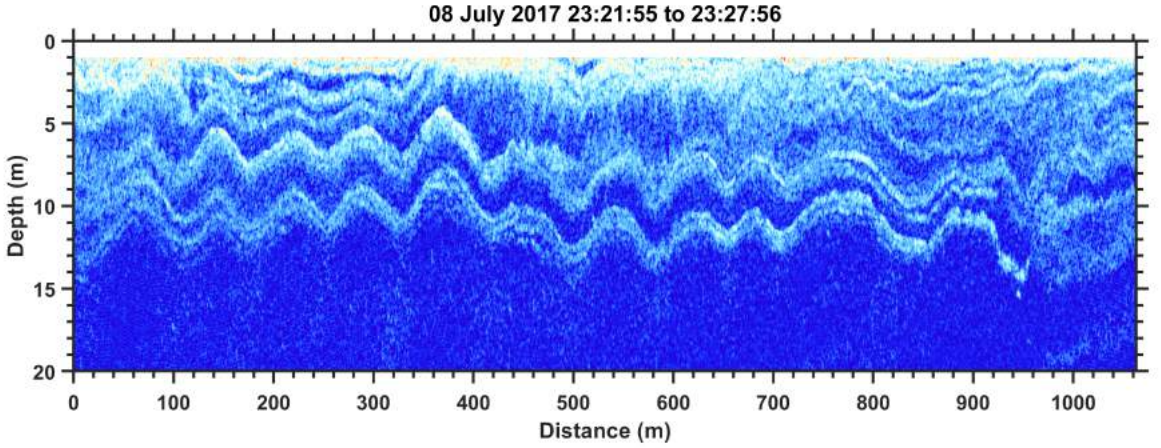
08 July 2017 23:21:55 to 23:27:56
Depth (m)
0
5
10
15
20
0
100
200
300
400
500
600
700
800
900
1000
Distance (m)

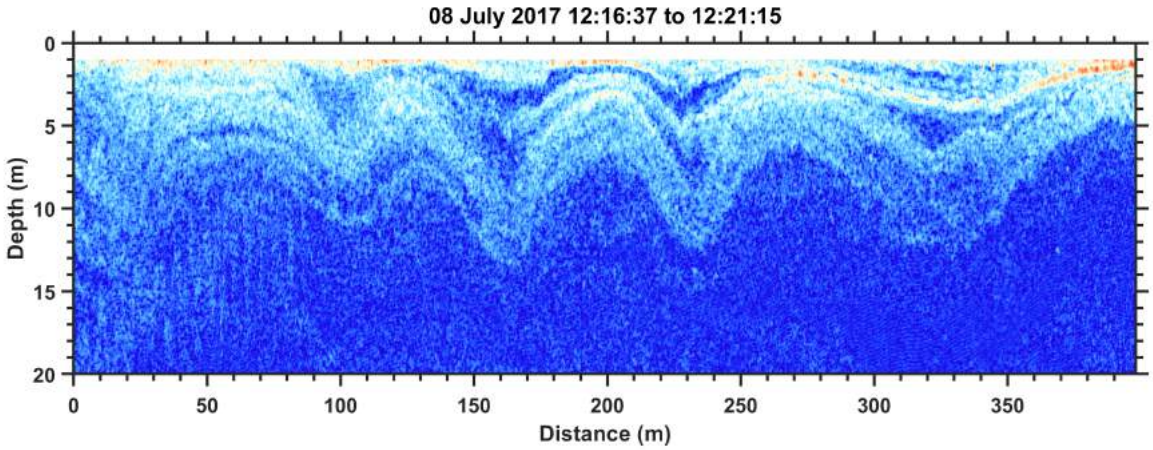
08 July 2017 12:16:37 to 12:21:15
Depth (m)
0
5
10
15
20
0
50
100
150
200
250
300
350
Distance (m)

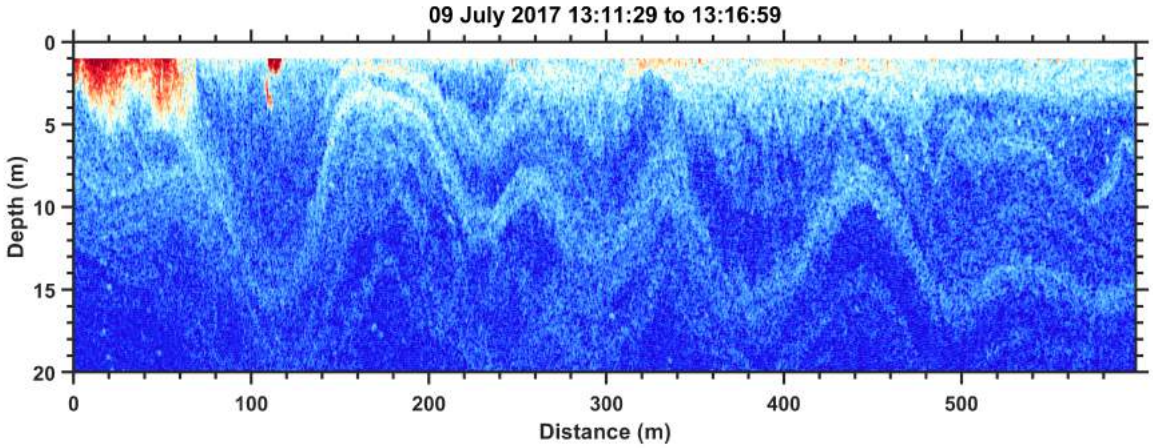
09 July 2017 13:11:29 to 13:16:59
Depth (m)
0
5
10
15
20
0
100
200
300
400
500
Distance (m)

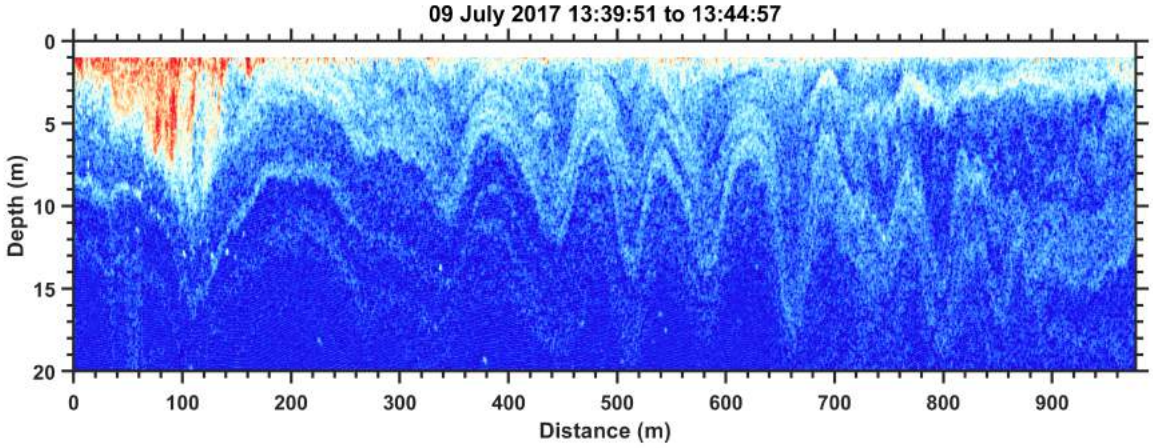
09 July 2017 13:39:51 to 13:44:57
Depth (m)
0
5
10
15
20
0
100
200
300
400
500
600
700
800
900
Distance (m)

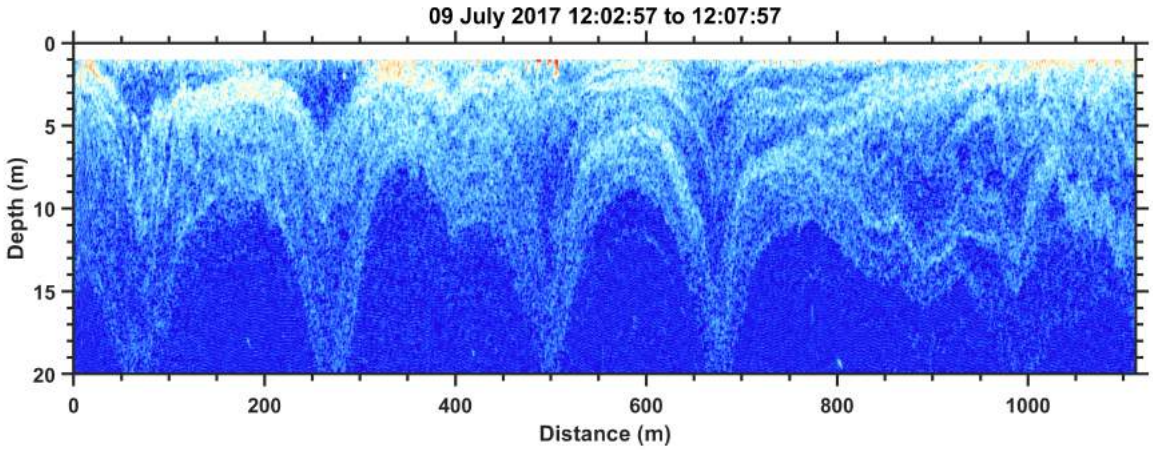
09 July 2017 12:02:57 to 12:07:57
Depth (m)
0
5
10
15
20
0
200
400
600
800
1000
Distance (m)

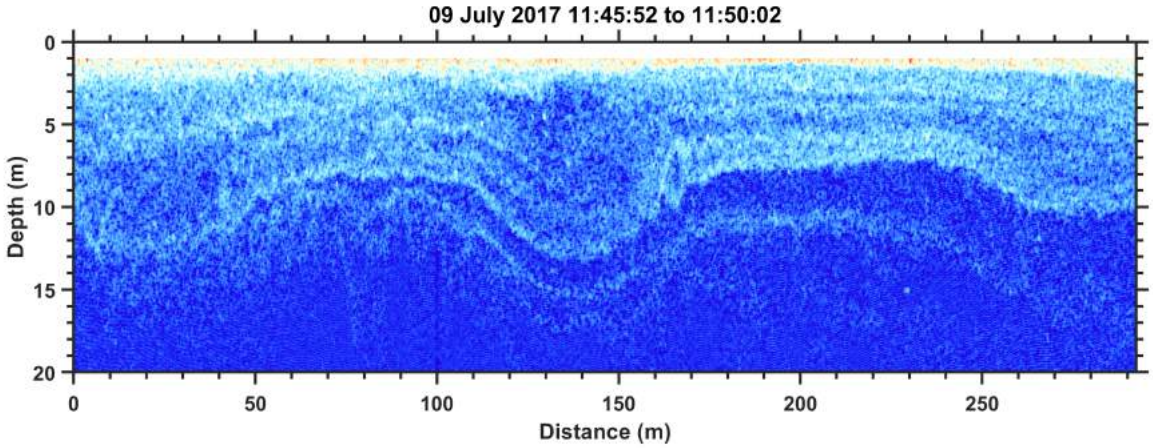
09 July 2017 11:45:52 to 11:50:02
Depth (m)
0
5
10
15
20
0
50
100
150
200
250
Distance (m)

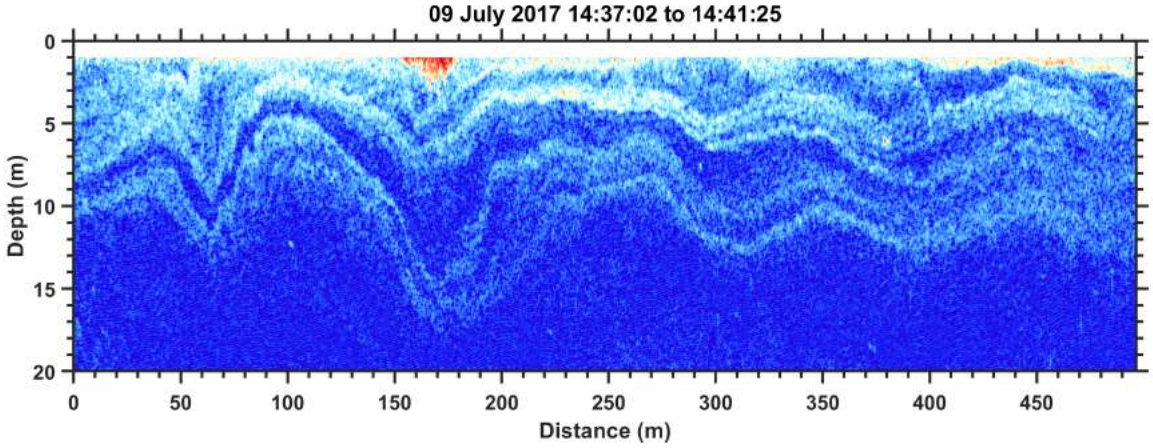
09 July 2017 14:37:02 to 14:41:25
Depth (m)
0
5
10
15
20
0
50
100
150
200
250
300
350
400
450
Distance (m)

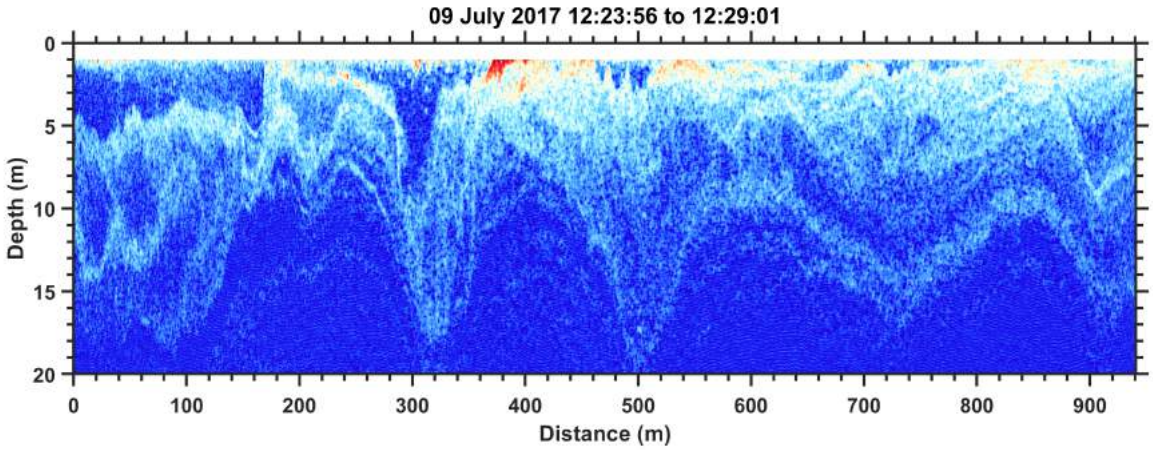
09 July 2017 12:23:56 to 12:29:01
Depth (m)
0
5
10
15
20
0
100
200
300
400
500
600
700
800
900
Distance (m)

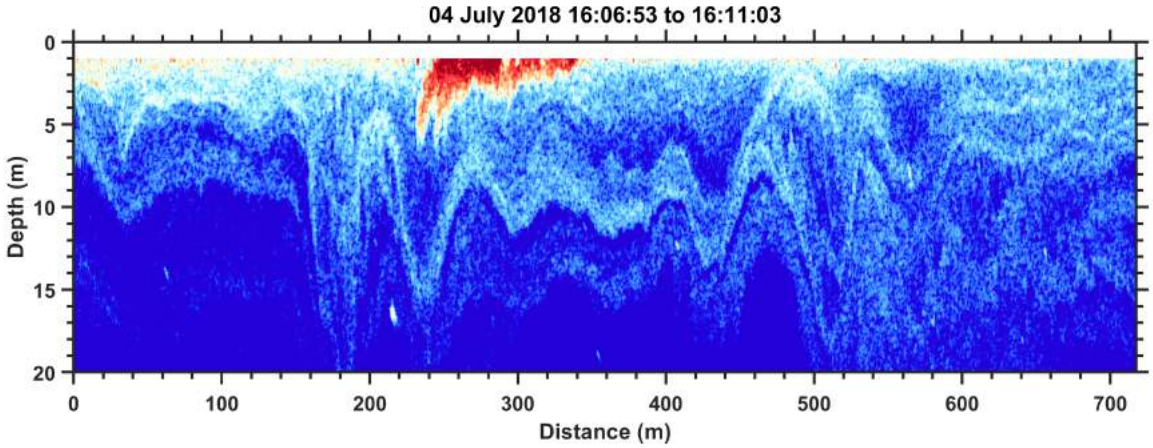
04 July 2018 16:06:53 to 16:11:03
Depth (m)
0
5
10
15
20
0
100
200
300
400
500
600
700
Distance (m)

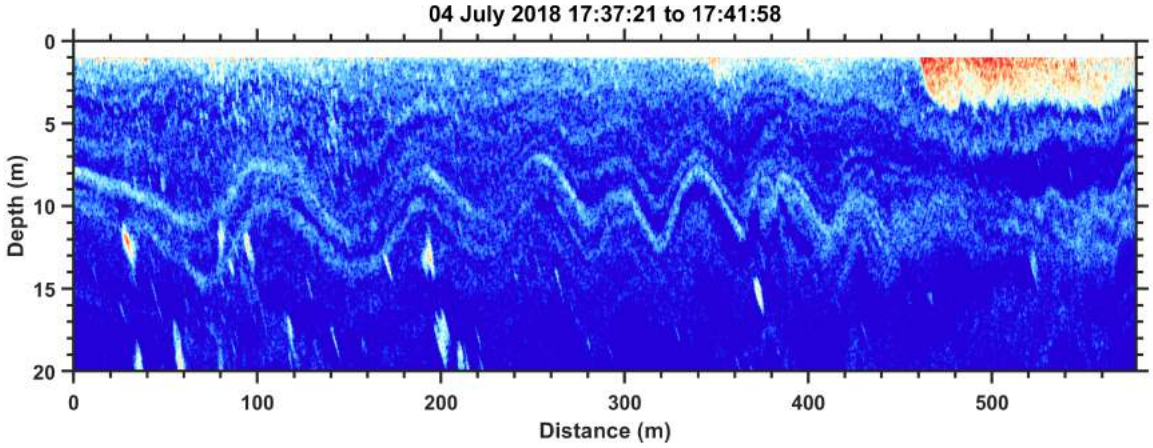
04 July 2018 17:37:21 to 17:41:58
Depth (m)
0
5
10
15
20
0
100
200
300
400
500
Distance (m)

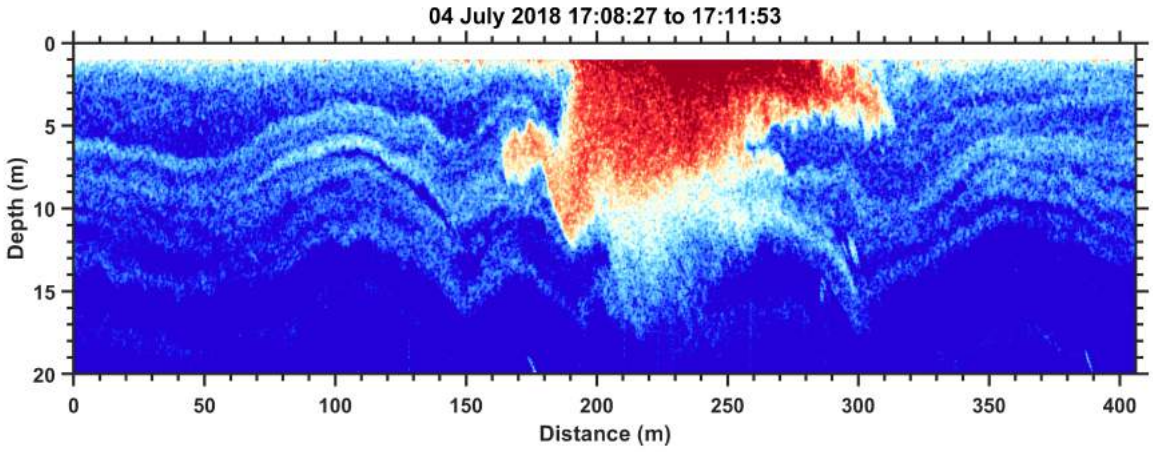
04 July 2018 17:08:27 to 17:11:53
Depth (m)
0
5
10
15
20
0
50
100
150
200
250
300
350
400
Distance (m)

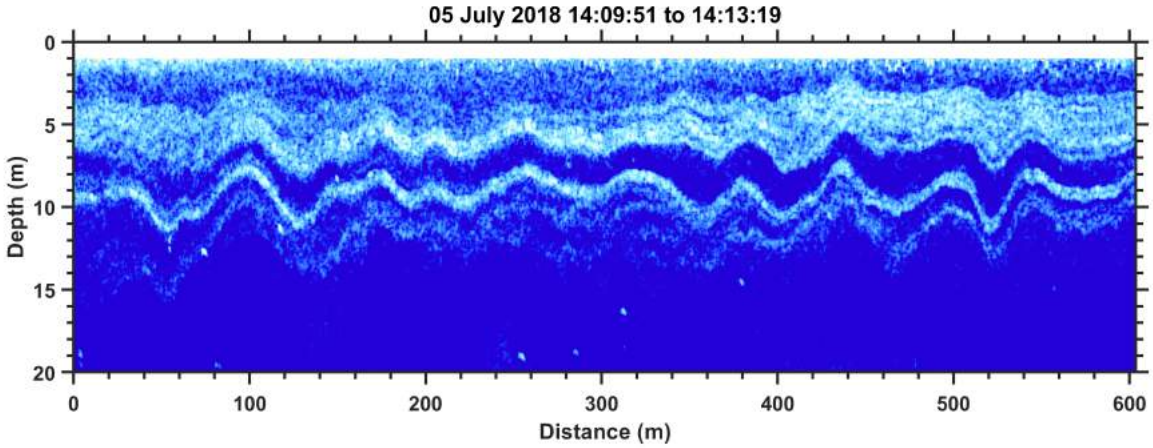
05 July 2018 14:09:51 to 14:13:19
Depth (m)
0
5
10
15
20
0
100
200
300
400
500
600
Distance (m)

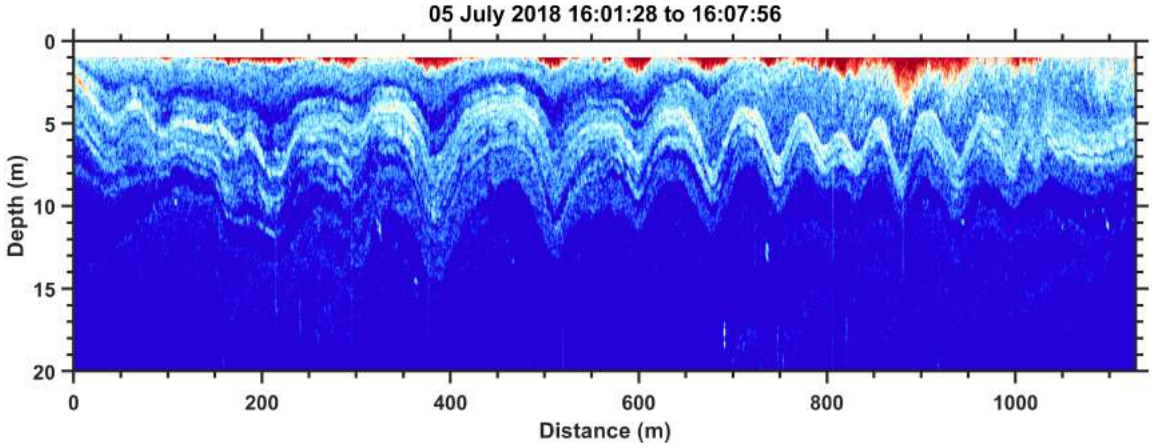
05 July 2018 16:01:28 to 16:07:56
Depth (m)
0
5
10
15
20
0
200
400
600
800
1000
Distance (m)

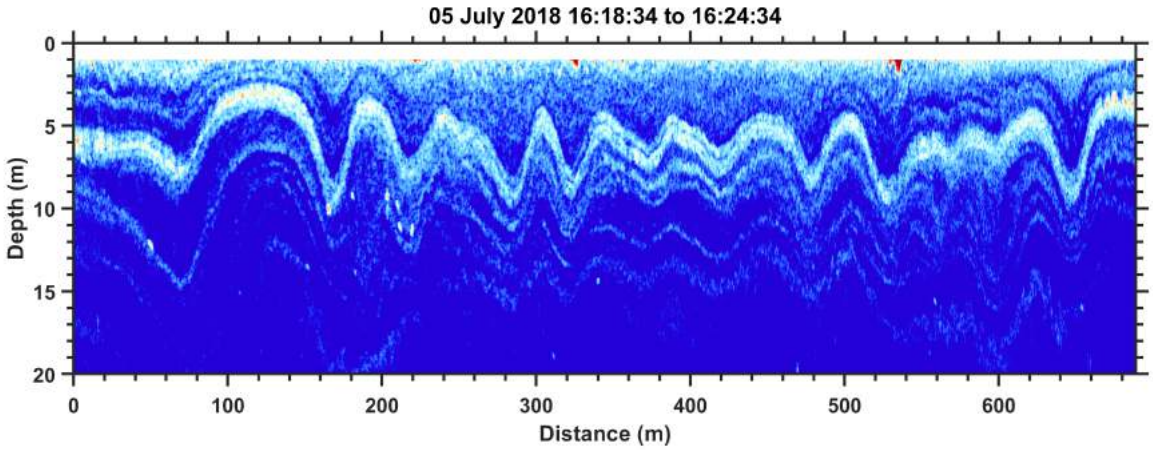
05 July 2018 16:18:34 to 16:24:34
Depth (m)
0
5
10
15
20
0
100
200
300
400
500
600
Distance (m)

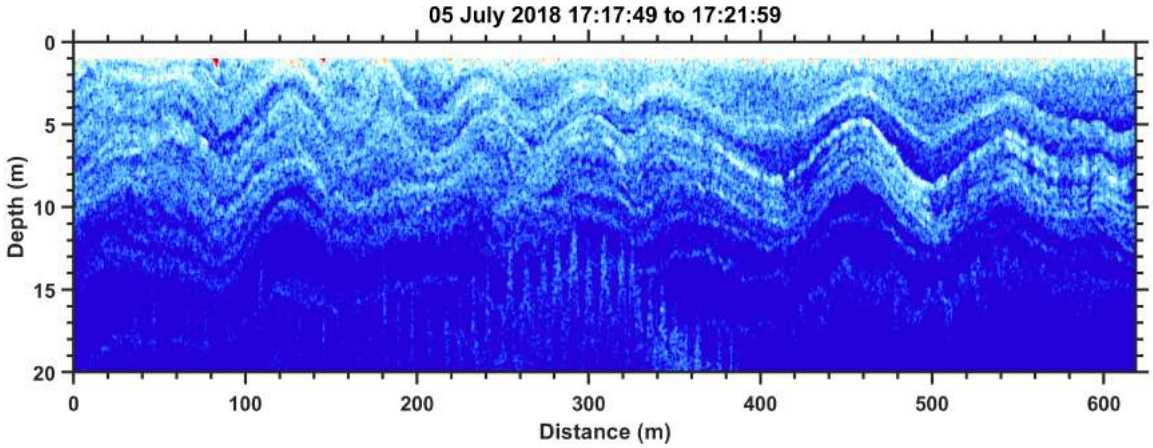
05 July 2018 17:17:49 to 17:21:59
Depth (m)
0
5
10
15
20
0
100
200
300
400
500
600
Distance (m)

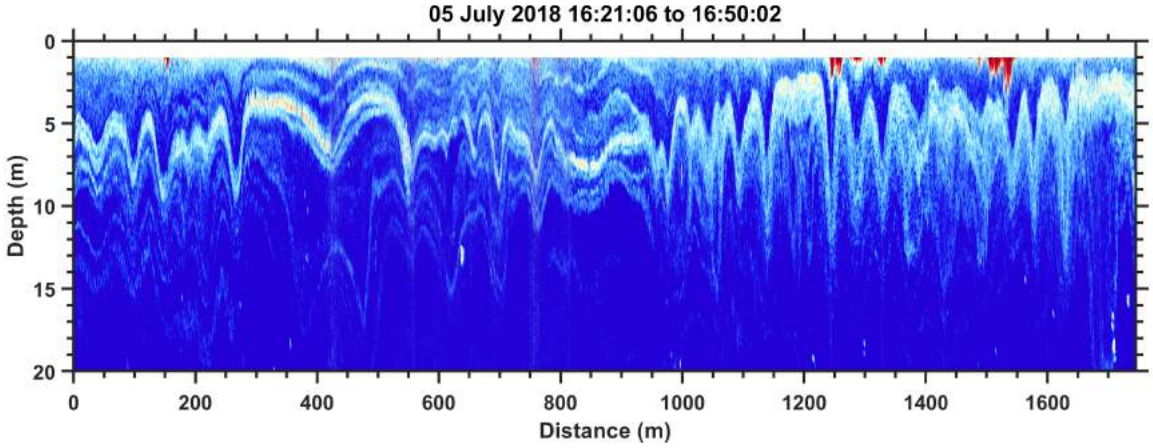
05 July 2018 16:21:06 to 16:50:02
Depth (m)
0
5
10
15
20
0
200
400
600
800
1000
1200
1400
1600
Distance (m)

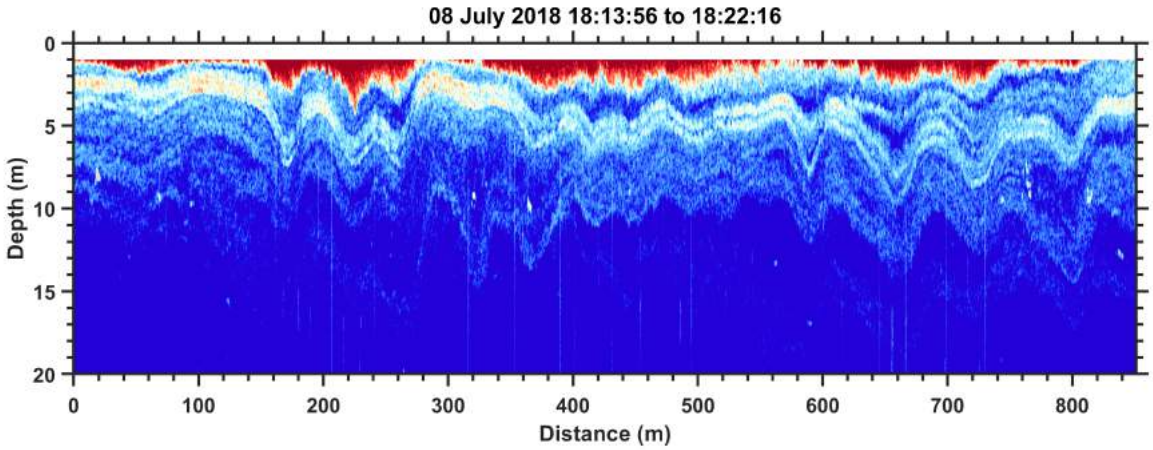
08 July 2018 18:13:56 to 18:22:16
Depth (m)
0
5
10
15
20
0
100
200
300
400
500
600
700
800
Distance (m)

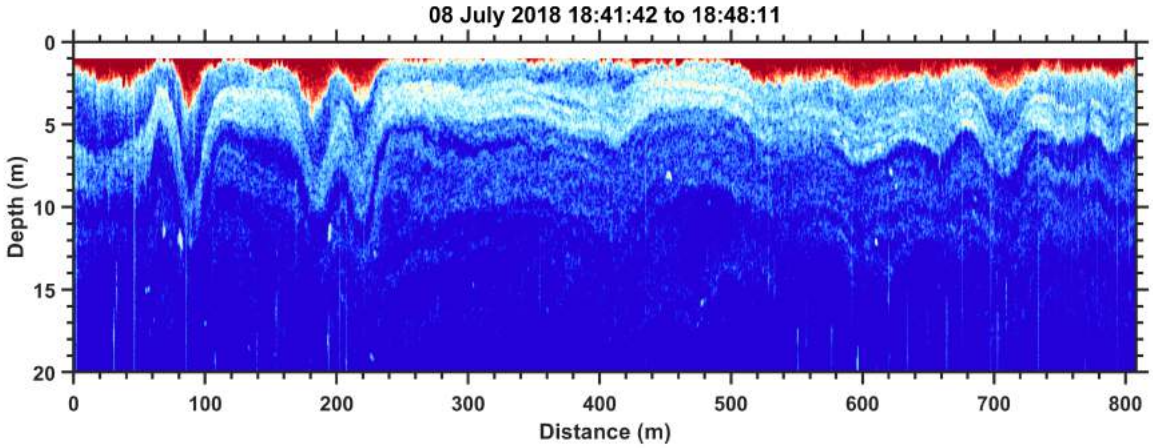
08 July 2018 18:41:42 to 18:48:11
Depth (m)
0
5
10
15
20
0
100
200
300
400
500
600
700
800
Distance (m)

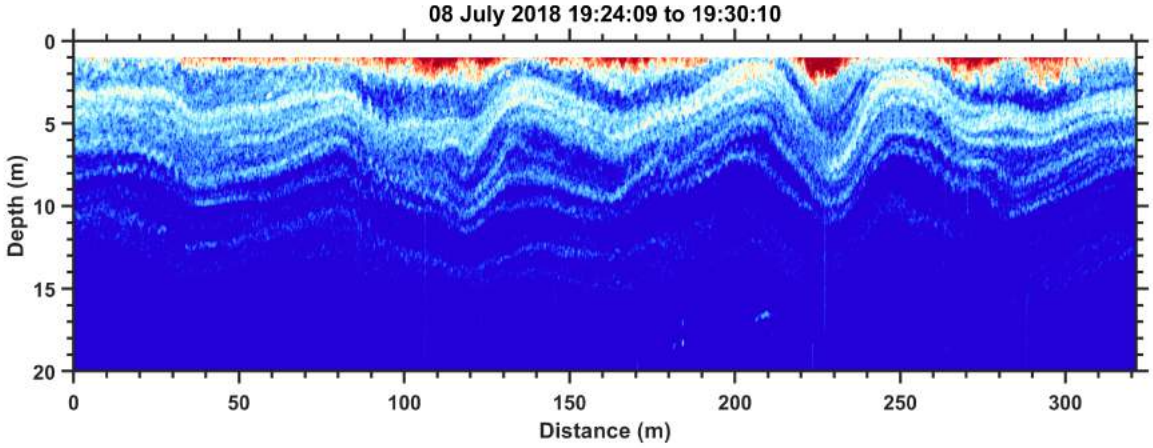
08 July 2018 19:24:09 to 19:30:10
Depth (m)
0
5
10
15
20
0
50
100
150
200
250
300
Distance (m)

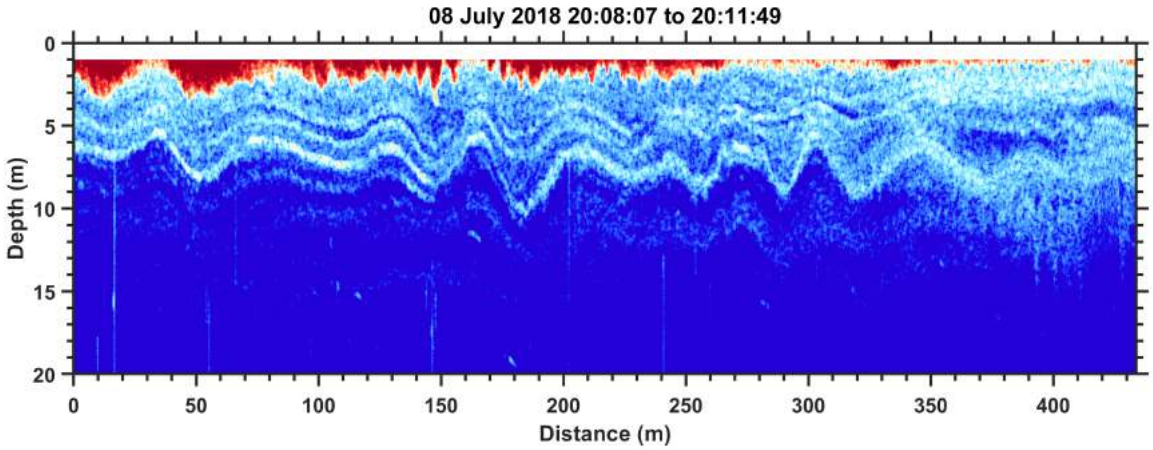
08 July 2018 20:08:07 to 20:11:49
Depth (m)
0
5
10
15
20
0
50
100
150
200
250
300
350
400
Distance (m)

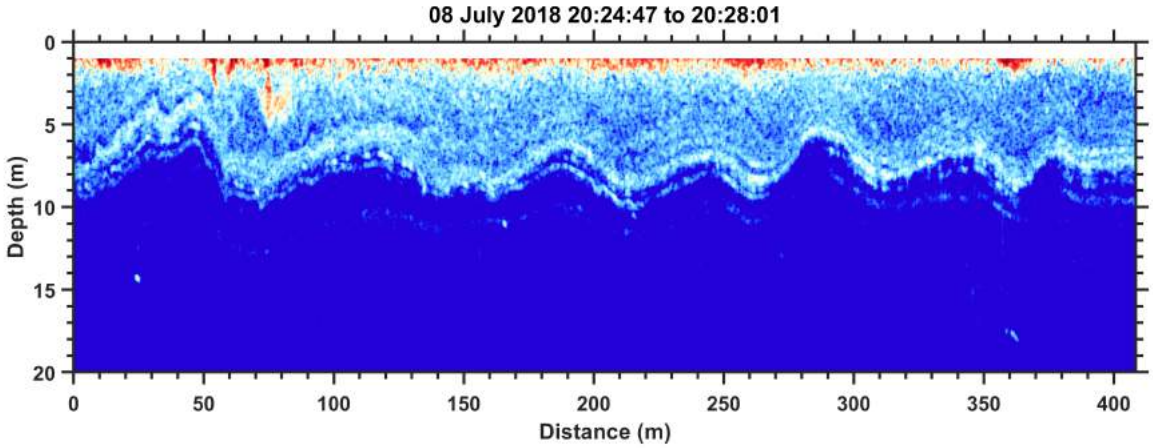
08 July 2018 20:24:47 to 20:28:01
Depth (m)
0
5
10
15
20
0
50
100
150
200
250
300
350
400
Distance (m)

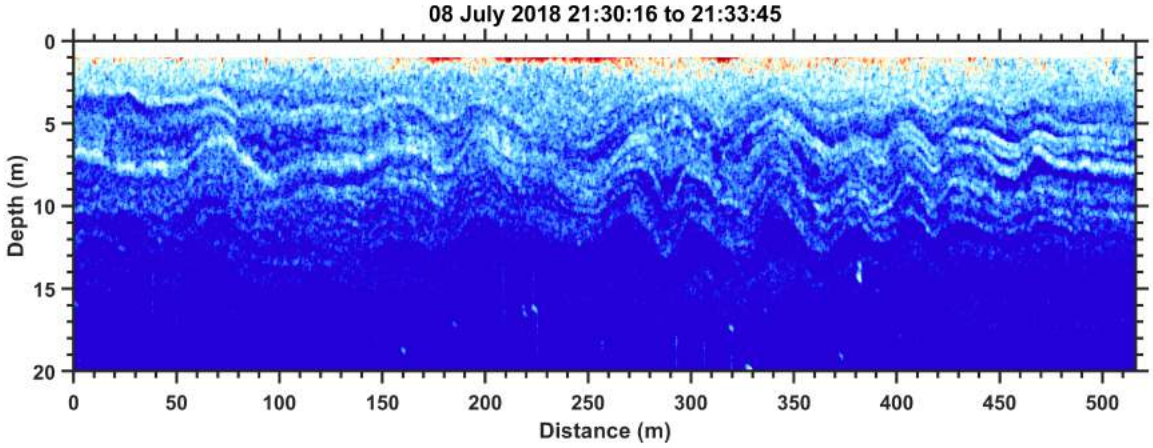
08 July 2018 21:30:16 to 21:33:45
Depth (m)
0
5
10
15
20
0
50
100
150
200
250
300
350
400
450
500
Distance (m)

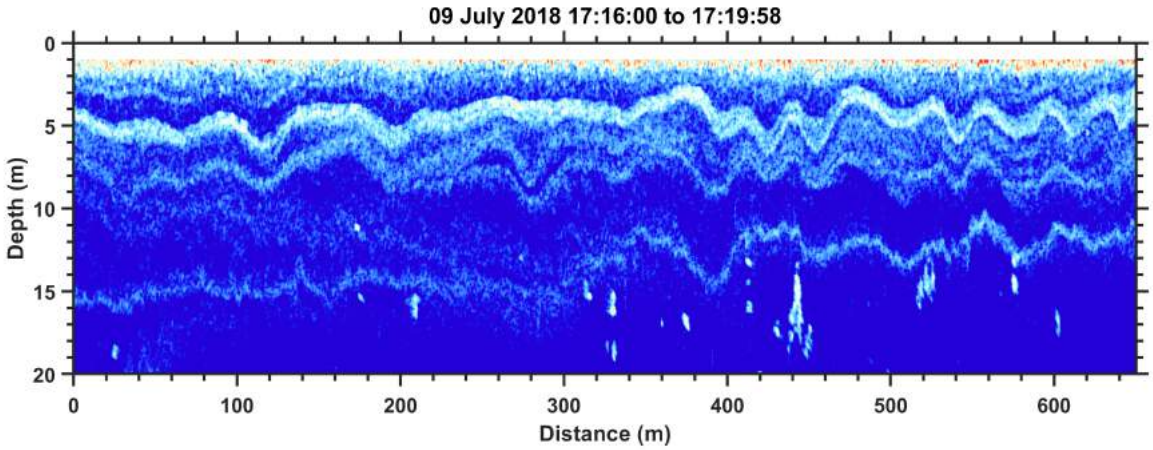
09 July 2018 17:16:00 to 17:19:58
Depth (m)
0
5
10
15
20
0
100
200
300
400
500
600
Distance (m)

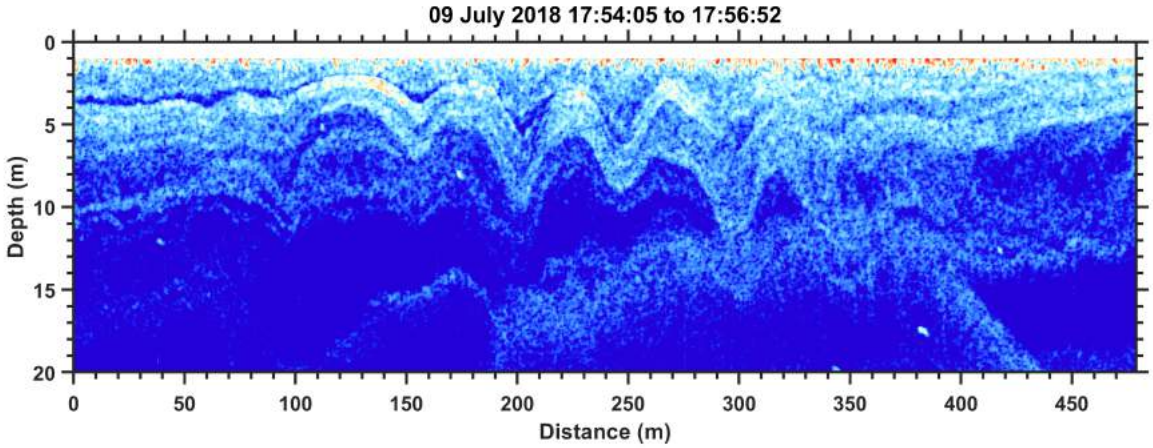
09 July 2018 17:54:05 to 17:56:52
Depth (m)
0
5
10
15
20
0
50
100
150
200
250
300
350
400
450
Distance (m)

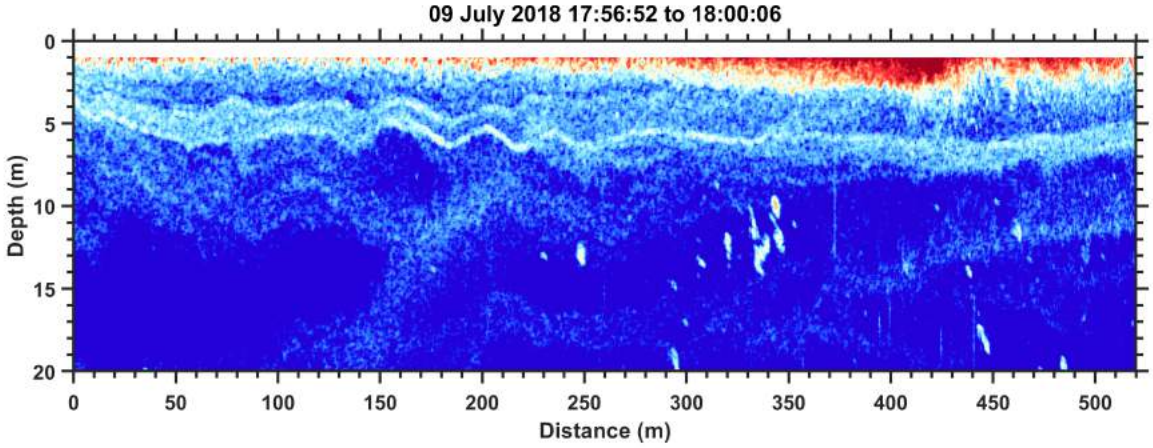
09 July 2018 17:56:52 to 18:00:06
Depth (m)
0
5
10
15
20
0
50
100
150
200
250
300
350
400
450
500
Distance (m)

RÉFÉRENCES

Alford, M., Peacock, T., Mackinnon, J., 2015. The formation and fate of internal waves in the south china sea. Nature 521.

Apel, J. R., 2002. Oceanic internal waves and solitons. An atlas of oceanic internal solitary waves, 1–40.

Arakawa, A., 1966. Computational design for long-term numerical integration of the equations of fluid motion: Two-dimensional incompressible flow. part i. J. Comput. Phys. 1.

Belzile, M., Galbraith, P., Bourgault, D., 2016. Water renewals in the saguenay fjord. J. Geophys. Res. Oceans 120.

Boegman, L., Ivey, G., Imberger, J., 2005. The degeneration of internal waves in lakes with sloping topography. Limnology and oceanography 50 (5), 1620–1637.

Boegman, L., Stastna, M., 2019. Sediment resuspension and transport by internal solitary waves. Annual review of fluid mechanics 51, 129–154.

Bourgault, D., 2008. Shore-base photogrammetry of river ice. Can. J. Civ. Eng. 35.

Bourgault, D., Galbraith, P., Chavanne, C., 2016. Generation of internal solitary waves by frontally forced intrusions in geophysical flows. Nat. Commun. 7.

Bourgault, D., Galbraith, P., Winkler, G., 2012. Exploratory observations of winter oceanographic conditions in the saguenay fjord. Atmosphere-ocean 50 (1), 17–30.

Bourgault, D., Janes, D., Galbraith, P., 2011. Observations of a large-amplitude internal wave train and it's reflection over a steep slope. J. Phys. Ocean. 41 (3).

Bourgault, D., Kelley, D., 2004. A laterally averaged nonhydrostatic ocean model. J. Atmos. Oceanic Technol. 21.

Bourgault, D., Morsili, M., Richards, C., Neumeier, U., Kelley, D., 2014. Sediment resuspension and nepheloid layers induced by long internal solitary waves shoaling orthogonally on uniform slopes. Continental Shelf Research 72.

Bourgault, D., Pawlowicz, R., Richards, C., 2020. g_rect : a matlab package for georectifying oblique images.

Cheong, H.-B., Kuenen, J., Linden, P., 2006. The front speed of intrusive gravity currents. J. Fluid Mech. 552.

Christie, D., Muilhead, K., Clarke, R., 1981. Solitary waves in the lower atmosphere. Nature 293.

Christie, D., Muilhead, K., Hales, A., 1978. On solitary waves in the atmosphere. J. Atmos. Sci. 35 (5).

Da Silva, J. C. B., New, A., Magalhaes, J., 2011. On the structure and propagation of internal solitary waves generated at the mascarene plateau in the indian ocean. deep sea research part 1:. Ocean. Res. Papers 58 (3).

Dorostkar, A., Boegman, L., Pollard, A., 2017. Three-dimensional simulation of high-frequency nonlinear internal wave dynamics in c ayuga l ake. Journal of Geophysical Research: Oceans 122 (3), 2183–2204.

Ekman, V. W., 1904. On dead-water ; from Nansen F., Norwegian North Polar Expedition 1893-1896: Sci. Results XV. Vol. 5. Christiana ; London, Longmans, Green and Co.

Farid, H., Woodward, J. B., 2007. Video stabilization and enhancement.

Farmer, D. M., 1978. Observations of long nonlinear internal waves in a lake. J. Phys. Ocean. 8 (1).

Flynn, M. R., Boubarne, T., Linden, P. F., 2008. The dynamics of steady, partial depth intrusive gravity currents. Atmosphere Ocean 46 (4).

Galbraith, P., Bourgault, D., Belzile, M., 2018. Circulation et renouvellement des masses d'eau du fjord du saguenay. Le Naturaliste canadien 142 (2), 36–46.

Garrett, C., Munk, W., 1979. Internal waves in the ocean. Annual review of fluid mechanics 11 (1), 339–369.

Gerkema, T., Zimmerman, J. T. F., 2008. Lecture note : An introduction to internal waves.

Grue, J., Bourgault, D., Galbraith, P. S., 2016. Supercritical dead water: effect of nonlinearity and comparison with observations. J. Fluid Mech. 803.

Heikkila, J., Silven, O., 1997. A four-step camera calibration procedure with implicit image correction. IEEE International Conference on Computer Vision and Pattern Recognition.

Hoyler, J. Y., Huppert, H. E., 1980. Gravity currents entering a two-layer fluid. J. Fluid Mech. 100 (4).

Hunkins, K., Fliegel, M., 1973. Internal undular surges in seneca lake : A natural occurrence of solitons. J. Geophys. Res. 78 (3).

Jackson, J. C. R., Da Silva, J. C. B., Jeans, G., 2012. The generation of nonlinear internal waves. Oceanography 25 (2).

Janes, D. C., 2008. Sills processes in the saguenay fjord. Master's thesis, Memorial University.

Lamb, K. G., 2003. Shoaling solitary internal waves: on a criterion for the formation of waves with trapped cores. J. Fluid Mech. 478.

Lamb, K. G., 2010. Energetics of internal solitary waves in a background sheared current. Nonlin. Processes Geophys. 17.

Lee, C.-Y., Beardsley, R. C., 1974. The generation of long nonlinear internal waves in a weakly stratified shear flow. J. Phys. Res. 79 (3).

Lien, R.-C., Henyey, F., Ma, B., Yang, Y. J., 2014. Large-amplitude internal solitary waves observed in the northern south china sea: Properties and energetics. J. Phys. Ocean. 14.

Marmorino, G. O., Smith, G. B., 2007. Infrared imagery of a turbulent intrusion in a stratified environment. G.B. Estuaries and Coasts: J ERF 30 (4).

Martin, J. P., Rudnik, D. L., Pinkel, R., 2006. Spatially broad observations of internal waves in the upper ocean at the hawaiian ridge. J. Phys. Ocean. 26.

Maxworthy, T., 1979. A note on the internal solitary waves produced by tidal flow over a three-dimensional ridge. J. Phys. Res. 84 (C1).

Maxworthy, T., 1980. On the formation of nonlinear internal waves from the gravitational collapse of mixed regions in two and three dimensions. J. Fluid Mech. 96 (01).

Michallet, H., Ivey, G. H., 1999. Experiments on mixing due to internal solitary waves breaking on uniform slopes. J. Geophys. Res. 104 (C6).

Miloh, T., Tulin, M. P., Zilman, G., 1993. Dead-water effects of a ship moving in stratified sea. J. Offshore Mech. Arct. Eng. 115.

Nansen, F., 1900. The Norwegian North Polar Expedition, 1893-1896; scientific results. Vol. 1. Christiana ; London, Longmans, Green and Co.

Nash, J. D., Moum, J. N., 2005. River plumes as a source of large-amplitude internal waves in the coastal ocean. Nat. Lett. 437.

Ouazzani, Z. R., Hacker, J. M., Thompson, R., Peacock, T., 2014. The morning glory: Flow visualization by mother nature. Phys. of fluids 26 (091110).

Pannard, A., Beisner, B. E., Bird, D. F., Braun, J., Planas, D., Bormans, M., 2011. Recurrent internal waves in a small lake: Potential ecological consequences for metalimnetic phytoplankton populations. Limnology and Oceanography: Fluids and Environments 1 (1), 91–109.

Papalas, A. J., 1997. The development of the trireme. The Mariner's Mirror 83 (3).

Pawlowicz, R., 2003. Quantitative visualization of geophysical flows using low-cost oblique digital time-lapse imaging. IEEE J. Oceanic Eng. 28 (4).

Pawlowicz, R., 2020. M_map: A mapping package for matlab, version 1.4m. URL www.eoas.ubc.ca/~rich/map.html

Reeder, M. J., Grimshaw, R., Christie, D. R., Smith, R., 1995. Interacting "morning glories" over northern australia. Bulletin of the American Meteorological Society 76 (7).

Richards, C., Bourgault, D., Galbraith, P. S., Hay, A., Kelley, D. E., 2013. Measurements of shoaling internal waves and turbulence in an estuary. Journal of Geophysical Research: Oceans 118 (1), 273–286.

Schwarz, G. R., 2008. The iberian caravel: Tracing the development of a ship of discovery, in vieira de castro, f., and custer, k., eds., edge of empire: Casal de cambra (portugal). Caleidoscópio—Edição e Artes Gráficas.

Siebert, G. H., Trites, R. W., Reid, S. J., 1979. Deepwater exchange processes in the saguenay fjord. J. Fish. Res. Board Can. 36 (1).

Stigebrandt, A., 1976. Vertical diffusion driven by internal waves in a sill fjord. J. Phys. Oceano. 6.

Sutherland, B. R., Flynn, M. R., Dohan, K., 2004a. Internal wave excitation from a collapsing mixed region. Deep-Sea Res. 2 51.

Sutherland, B. R., Kypa, P. J., Flynn, M. R., 2004b. Intrusive gravity currents in two-layer fluids. J. Fluid Mech. 514.

Thorpe, S. A., Hall, A., Crofts, I., 1972. The internal surge in loch ness. Nature 237 (5350).

Wang, C., Pawlowicz, R., 2017. Internal wave generation from tidal flow exiting a constricted opening. J. Geophys. Res. Oceans 122.

Wang, C., Wang, X., Da Silva, J. C. B., 2019. Studies of internal waves in the strait of georgia based on remote sensing images. Remote Sens 11 (96).

Wang, Y.-H., Dai, C.-F., Chen, Y.-Y., 2007. Physical and ecological processes of internal waves on an isolated reef ecosystem in the south china sea. Geophys. Res. Lett. 34 (L18609).

Watson, G., Chapman, R. D., Apel, J. R., 1992. Measurements of the internal wave wake of a ship in a highly stratified sea loch. J. Geo. Res. 97 (C6).